FLUID MECHANIC PHENOMENA RELATING TO FLOW CONTROL IN CONDUITS AND PUMPS

A DISSERTATION
SUBMITTED TO THE FACULTY OF
UNIVERSITY OF MINNESOTA
BY

YILMAZ BAYAZIT

IN PARTIAL FULLFILLMENT OF THE REQUIREMENTS
FOR THE DEGREE OF
DOCTOR OF PHILOSOPHY

ADVISER: WILLIAM L. GARRARD

AUGUST 2014

Table of Contents

List of Tables

List of Figures

CHAPTER 1: INTRODUCTION

Fluid mechanics has many forms and facets. It covers a vast range of applications while, at the same time, it has attracted the interest of the best theoretical thinkers. Fluid mechanic phenomena dominate every aspect of life on earth as well as biological processes which are essential to human life. The monumental spectrum of fluid mechanic applications and processes has created a vast umbrella which accommodates an enormous diversity of engineers and scientists. Those workers may be conveniently cataloged as either creators of knowledge or as appliers of knowledge.

This thesis fits comfortably within that umbrella at a location where creators of knowledge congregate. The knowledge stemming from the research performed here is a response to the needs of vital engineering applications. In particular, the work is motivated by the need to control and shape fluid flows to enhance their effective use in a range of critical technologies.

For example, heat transfer devices are major participants in the current energy scene. The efficiency of such devices is majorly dependent on the nature of the fluid flows which pass through them. When such flows are maldistributed either at the inlet or in the interior of a heat exchange device, there will be a loss of energy.

This issue is exaggerated in contemporary efforts to minimize what is commonly referred to as *waste heat*. In that regard, dual-cycle electric power producing machines have recently become a major focus for innovation. These devices consist of gas-turbine and steam-turbine power plants arranged in series. The still-energetic combustion products in the gas-turbine exhaust are used to transform liquid water to vapor in the steam plant. However, the cross section of the exit of the gas-turbine plant is drastically area mismatched with the cross section of the ductwork of the steam plant. Moreover, the combustion products flowing out of the gas turbine exit possess a highly vigorous swirl component.

To efficiently utilize the steam plant, powerful means must be created and employed to tame the irregularities and inhomogenities that are the legacy of the gas-turbine exhaust. The practical means to accomplish this necessary action is the perforated plate. A highly schematic cartoon of this situation is conveyed in Figs. 1(a) and (b). The first of these illustrates the highly unruly flow which would exist in the duct upstream of the steam generator in the absence of the perforated plate. In contrast, the (b) part of the figure displays the nature of the flow when a perforated plate is positioned at the inlet of that duct. A schematic diagram of an installed perforated plate is exhibited in Fig. 2.

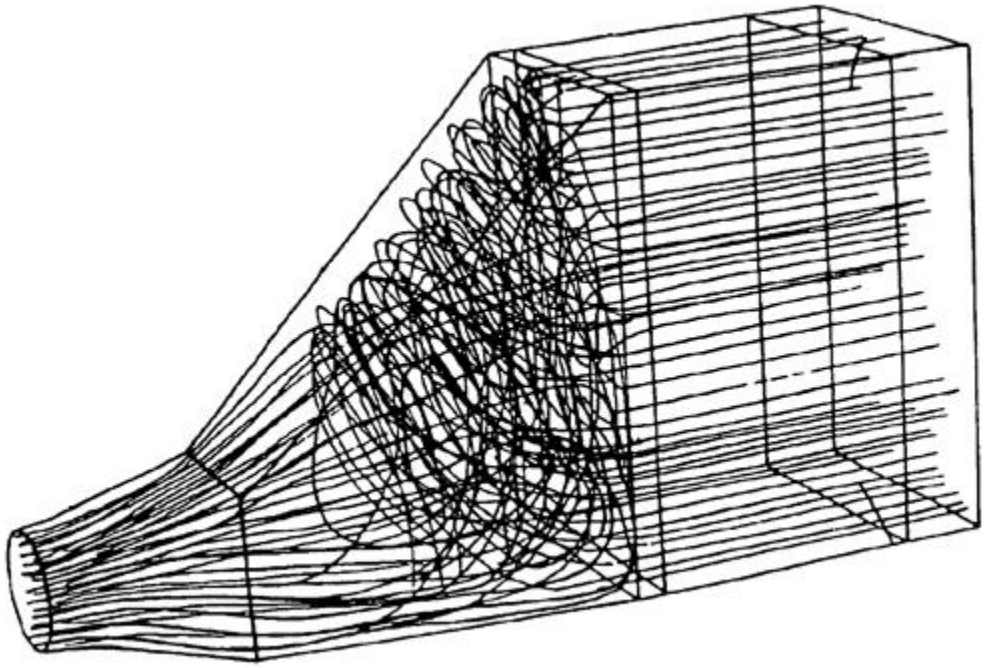

Fig. 1 (a): Cartoon of the unmanaged fluid flow passing from the exit of a gas turbine power plant into the inlet duct of a steam plant.

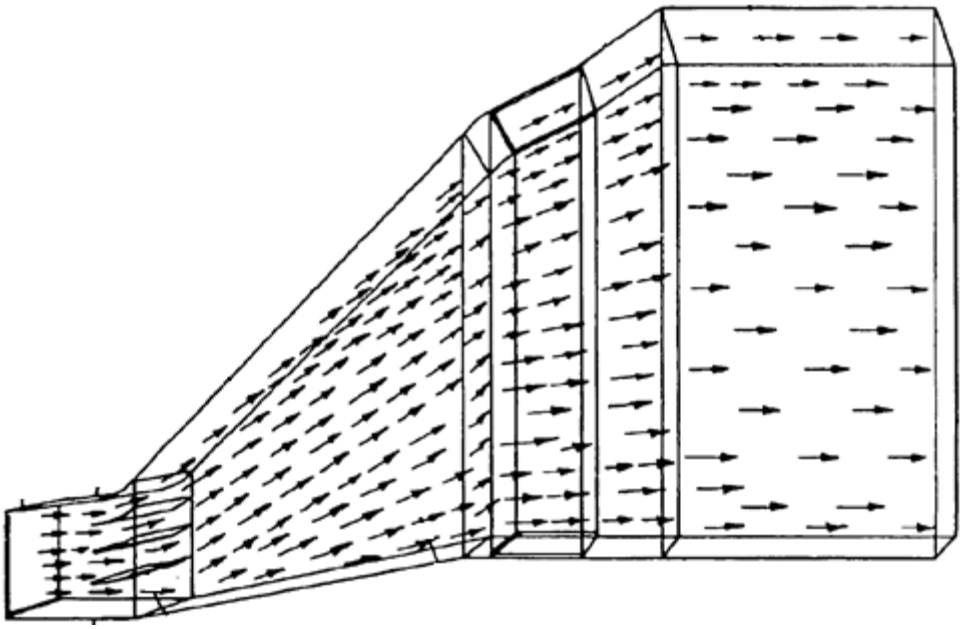

Fig. 1 (b): Cartoon of the managed fluid flow passing from the exit of a gas turbine power plant into the inlet duct of a steam plant.

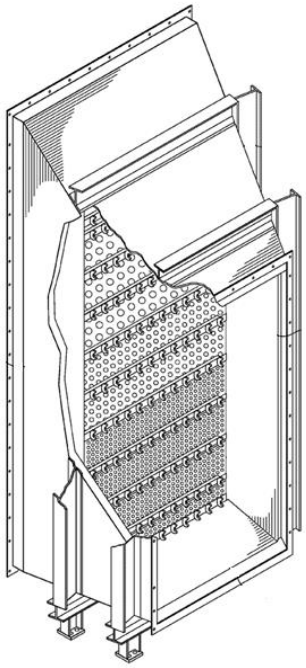

Fig. 2: Schematic diagram of perforated plate used to homogenize the exit flow from a gas turbine power plant prior to its introduction into a steam power plant.

The foregoing discussion serves to motivate the research performed in this thesis. It is built on the clear recognition of the importance of flow conditioning and control in real-world applications. The topical coverage of the thesis encompassed control/conditioning of complex ducted flows and the control of flows produced by pumps.

The device that has found greatest favor in engineering practice for the control/conditioning of complex ducted flows is the perforated plate. A perforated plate is a plane plate into which a regular array of circular apertures has been fabricated. As will be documented shortly, the existing literature is almost completely empirical, uncoordinated, and without any consideration of the underlying physical processes.

In the present research, a synergistic combination of numerical simulation and experimentation has been implemented to investigate the underlying physical processes relevant to perforated-plate flow conditioning devices and to determine results of immediate use for the design of such devices. For the experiments, a dedicated wind tunnel was fabricated to facilitate the work. The main goal of the experiments was to provide a standard for the validation of the numerical simulations. The numerical simulations covered a wider range of physical situations than did the experiments, encompassing perforated plates that are either perpendicular or inclined to the oncoming flow. Other geometric parameters included plate thickness, plate porosity, and aperture deployment. In those cases involving plates inclined to the oncoming flow, the cross section geometry of host duct required specification. The numerical simulations were extended over all recognized flow regimes consistent with incompressible flow.

The phenomena-focused studies were motivated by the need to resolve seeming paradoxes. For example, one such paradox was encountered when the pressure drop across a thin plate was found to be larger than that across a thicker plate, all other conditions being equal.

A different facet of flow control was investigated for a newly devised hydraulic pump. That work was accomplished by utilizing pure analysis. The participating physical phenomena included both fluid flow and structural considerations. This type of problem is typically described by the acronym FSI (fluid-structure interaction). The outcome of the analysis provided a pair of coupled, non-linear algebraic equations. Numerical solutions of the equations provided the pressure variation in a piston bore, comparing pumps with canted bores to those with cylindrical bores. Also, the flow—pressure drop relationship and other relevant results were gathered. It was also shown that the inertial forces on the pumps with canted bores were smaller than the ones without enabling higher pump speeds.

The literature with respect to perforated plates is broad and worthy of exposition. For discussion purposes, it can be classified into various categories. The category that is most relevant to the present investigation involves structurally rigid plates in contradistinction to wire meshes and deformable screens. The apertures in the plates are circular and are arranged in a regular pattern. There are a number of investigations of perforated plates whose circular apertures are arranged in groupings whose density varies with position. This is in contrast to the uniformity of the aperture arrays considered here.

The most encompassing collection of experimental data for situations that are relevant to the present study is that provided by Idelchik [1]. The presented data were collected by Idelchik from mostly unavailable Soviet works that were performed prior to 1966. Gan and Riffat [2] suggest the use of numerical simulation but provide too little information to be of practical or fundamental utility. Experiments for turbulent flow through perforated plates of various thicknesses were performed by Yavuzkurt and Catchen [3], but the final presentation of the data shows considerable scatter. The effect of chamfered inlet and exit geometries on the pressure drop across perforated plates was measured by Broach et al. [4], without any measurements for the baseline case of unchamfered inlets and exits.

Perforated plates have been used extensively as flow conditioners [5-10]. One use is to dissipate disturbances caused by obstructions and pipe bends. Another is to diminish the length of straight pipe upstream of a flow measurement instrument required for accurate measurements. The papers relating to these applications were focused on measurements of velocity distributions, either by particle image velocimetry, laser-Doppler anemometry, and hot wire anemometry. In general, no measurements of pressure drop nor of fluid flow events upstream of the perforated plate were made.

A major negative impact on the performance of heat transfer devices is flow maldistribution. To counter this degraded performance, it is common to make use of flow conditioning devices to provide a more uniform inlet velocity. A large number of journal publications have dealt with this critical issue. A representative collection of these papers may be found in references [11-20].

Another facet of flow conditioning by the use of perforated plates and screens is encountered in connection with flow through diffusers. It is well established that except for very small diffuser angles, flow separation is commonly encountered. To control and counteract the effects of separation, perforated plates have been used [21-23]. A very common application involving the use of perforated plates positioned in diffusers is encountered in electrostatic precipitator systems.

In agriculture-based applications, screens are commonly used to control horticultural environments. The structure of a screen is more complex than that of a perforated plate, what with overlapping filaments or threads. This complexity has thus far resisted detailed analysis. Instead, it is common to treat flow through a screen as if it were a porous medium [24-29]. Depending on the Reynolds number, various models were used to relate the pressure gradients through the screen with the velocity. In [26], the separate dependence of the pressure drop on the nature of the weave of the screen was explicitly quantified. Entire greenhouses were modeled in [27, 28] with the screen being included as a boundary condition. In a simplified model [29], it was assumed that Bernoulli's

equation was sufficient to describe the pressure drop through the screen. This model defies the lossless assumptions that underlie the Bernoulli model.

In general, it may be stated that the existing work in the field lacks a fundamental basis and also is limited to specific physical situations.

No review of the fluid-flow role of perforated plates and screens is complete without taking note of the role of these devices in either suppressing turbulence [30, 31] or in creating tailored turbulence [32]. In a somewhat different context, a screen was employed to modify the turbulence in a boundary layer that had been tripped at its origin [33].

The chapter-by-chapter flow of the thesis is as follows: Chapter two is focused on the fluid mechanics of flow perpendicular to a perforated plate. This chapter reports the synergistic combination of experimentation and numerical simulation. The next chapter, Chapter three, extends the simulations to flow impinging at an angle of attack on a perforated plate. Chapter four gains inspiration from porous-medium theory to facilitate the development of an all-flow-regime model to bring together the pressure drop results of Chapters 2 and 3. In Chapter five, the Taguchi method is applied to evaluate the effects of design parameters such as Reynolds number, plate thicknesses, hole patterns, and the porosity of the plate on pressure drop. The final substantive chapter is Chapter six. In that chapter, the analytically based flow characteristics for a hydraulic pump are set forth.

CHAPTER 2: PERFORATED PLATES FOR FLUID MANAGEMENT: PLATE GEOMETRY EFFECTS AND FLOW REGIMES

1. Introduction

The motivation for the research reported here is the importance of perforated plates as a primary passive means for fluid and thermal management. The need for fluid flow control is highlighted in systems which include fittings that create major flow distortions. In particular, instrumentation accuracy requirements are frequently based on flows which are homogeneous and unidirectional, as is the efficiency of electrostatic precipitators. In agricultural applications, screens are widely used to control the environment in greenhouses. There are a number of heat transfer applications where homogeneous fluid flows are strictly necessary. For example, in flow passages marked by rapid enlargements in which there are duct burners, the efficiency of the combustion process critically depends on the nature of the oncoming flow. In another context, HVAC equipment such as total energy wheels is substantially affected by flow inhomogeneities.

In response to the needs for definitive fundamental and applicable information, an investigation was undertaken here to effectuate a broad and deep study of the flow characteristics of perforated plates which are situated perpendicular to a uniform oncoming free stream flow. The particular application that motivated the present investigation was the need for air flow control in a complex ducting system used to distribute fresh air in a large manufacturing facility.

The present research has multiple goals that span both fundamentals and engineering applications. With regard to fundamentals, identification of the limits of friction-dominated laminar flow is carefully determined, and the flow regime that follows the breakdown of the aforementioned laminar flow is definitively

identified. In like manner, the conditions marking the onset of pure turbulent flow are also carefully defined. The nature of the flow that takes place within the open apertures of perforated plates is investigated in great detail. That investigation is focused on the characteristics of the separated flow that occurs in the apertures. In particular, the nature of the separated flow has a dominant impact on the role of plate thickness with respect to the plate-based pressure drop. The downstream flow redevelopment lengths at which the plate-based flow disturbances have been definitively quantified. With regard to practical applications, a means was found to generalize the pressure-drop results to be applicable to various deployment patterns of the plate perforations. Furthermore, the effect of plate thickness is definitively documented.

The research encompasses synergistic interaction of experimentation and numerical simulation. The experimental work was motivated by the necessity of verifying the turbulence model selected for the simulation.

Nomenclature

a,b	coefficients in Forchheimer equation
c,d	edges of the symmetry triangle
D	hole diameter
L	downstream length at which disturbance disappears
P	pitch for square array
$P1$	equilateral pitch for staggered array
$P2$	longitudinal pitch for staggered array
Re_o	pore Reynolds number
Re_∞	upstream Reynolds number
U_o	mean fluid velocity in pores
Δp	overall pressure drop
t	plate thickness
x	distance within the bore
α,β	dimensionless Forchheimer coefficients
ε	plate porosity
μ	fluid viscosity
ρ	fluid density

2. Experimental Setup

An experimental facility was designed and fabricated to provide a means for validating the results of the numerical simulations. It was deemed necessary to evaluate the choice of a turbulence model, and the use of experimental operating conditions that coincided with those of the simulations appeared to be the most logical approach to this issue.

The facility, a wind tunnel, was especially designed to model the simulations and also to offer a flexible means of evaluating perforated plates of different geometrical characteristics. The facility was a square duct of side dimension 30.48 cm (12 inches) and overall length of 243.8 cm (96 inches). This wind tunnel is displayed in Fig. 3. It was operated in the suction mode, with air being

Fig. 3. Longitudinal view of the experimental facility.

drawn from the laboratory room through a flow straightener. The straightener consisted of a bed of 3500 straws, each straw having a diameter of 0.6 cm and a length of 19.5 cm (0.24 by 7.72 inches). The length-to- diameter ratio, 33, of the flow-straightener elements was deemed sufficient for the attainment of a uniform parallel flow. A photograph of the flow straightener assembly is displayed in Fig. 4. The downstream end of the wind tunnel emptied into a large plenum chamber

Fig. 4. Inlet to the wind tunnel showing the flow-straightening section.

from which air was drawn by means of an array of blowers. The plenum with a mated blower can be seen in Fig. 3.

The construction features of the wind tunnel were designed to allow easy access to the perforated plate. This access was an important feature because it enabled various plate configurations to be conveniently put in place. The access feature is illustrated in Fig. 5. That figure exhibits the interior of the wind tunnel as seen through the opening created by the removal of the upper wall of the tunnel. One of the perforated plates is shown in place in the photograph. By means of shallow grooves machined into the walls of the tunnel at the selected cross section, plates were removed and replaced by sliding the plate vertically as it is guided by the grooves.

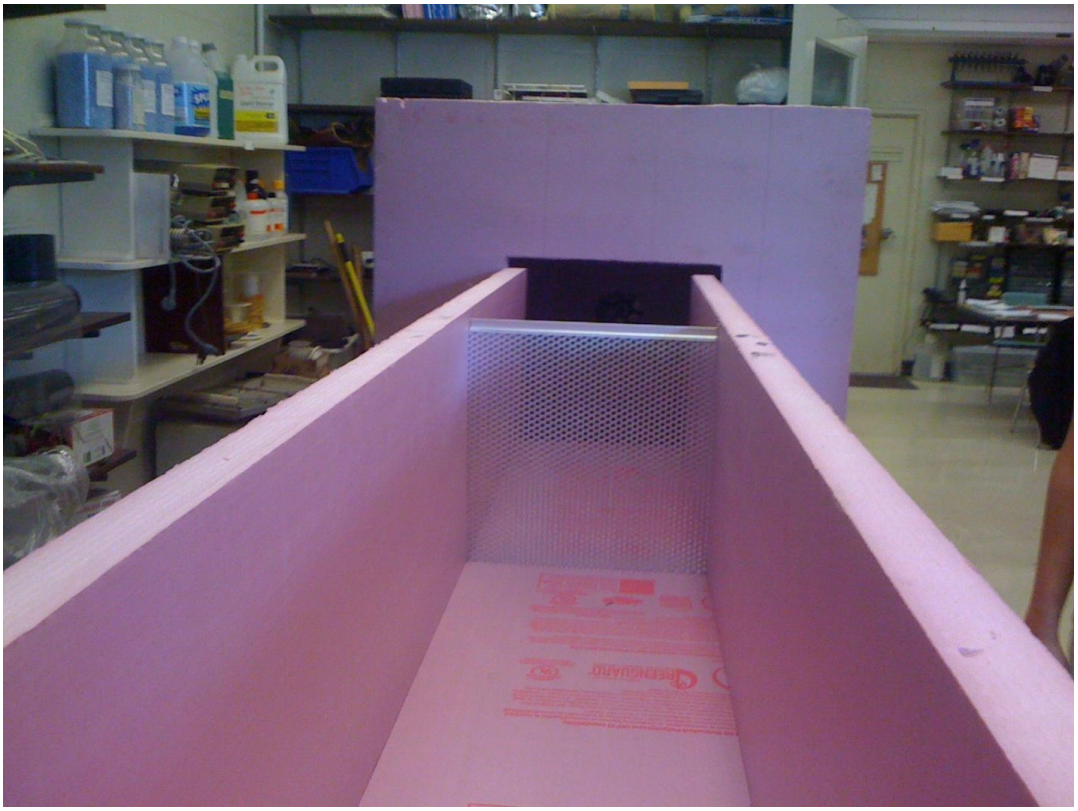

Fig. 5. Interior of the wind tunnel with a perforated plate in place as seen through the open top.

The wind tunnel was constructed of extruded polystyrene. It was assembled by means of tongue-in-groove mating. This material can be machined to very tight tolerances. As an additional defense against leakage, caulk was applied along mating surfaces.

The instrumentation used for data collection included two Pitot tubes and an array of pressure taps. The impact openings of the Pitot tubes were positioned at a common cross section, 45.7 cm (18 inches) upstream of the cross section of the perforated-plate location. One of the Pitot tubes entered the flow cross section from above and the second entered from the side. The Pitot tubes were specifically chosen to have different-sized impact openings and static ports. In addition, a wall pressure tap was installed at a streamwise location identical to that of the static ports of the Pitot tubes. It was verified that the static pressures measured by three independent means agreed to within 0.0005 inches of water. Furthermore, the velocities obtained from the two Pitot tubes agreed to the same level of accuracy.

Ten pressure taps were installed in the side wall of the wind tunnel at a uniform streamwise spacing of 2.54 cm (1 inch), downstream of the cross-sectional location of the perforated plate. This array of taps and the upstream tap can be seen in Fig. 6. Thanks to the easy access to the inside of the wind tunnel, the pressure taps could be carefully sanded to remove any irregularities.

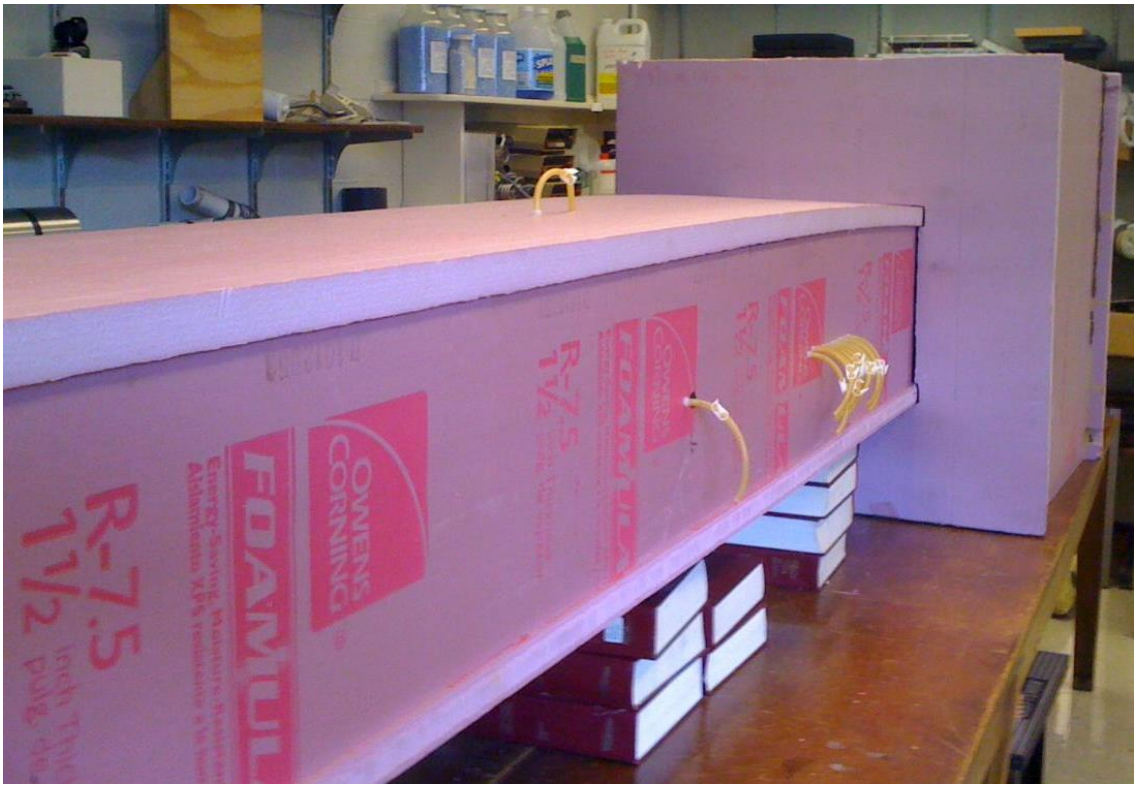

Fig. 6. Pressure taps installed in the side wall of the wind tunnel.

The various pressures were read by means of a micromanometer capable of resolving 0.0002 inches of water. A secondary instrument, an inclined manometer capable of resolving 0.01 inches of water was used to collect data for pressure differences that exceeded one inch of water. The velocity of approach of the air to the perforated plate was obtained from the Pitot tube measurements.

The various perforated plates employed for the experimental work included those made of stainless steel and ABS plastic. A CAD model of a typical perforated plate is displayed in Fig. 7.

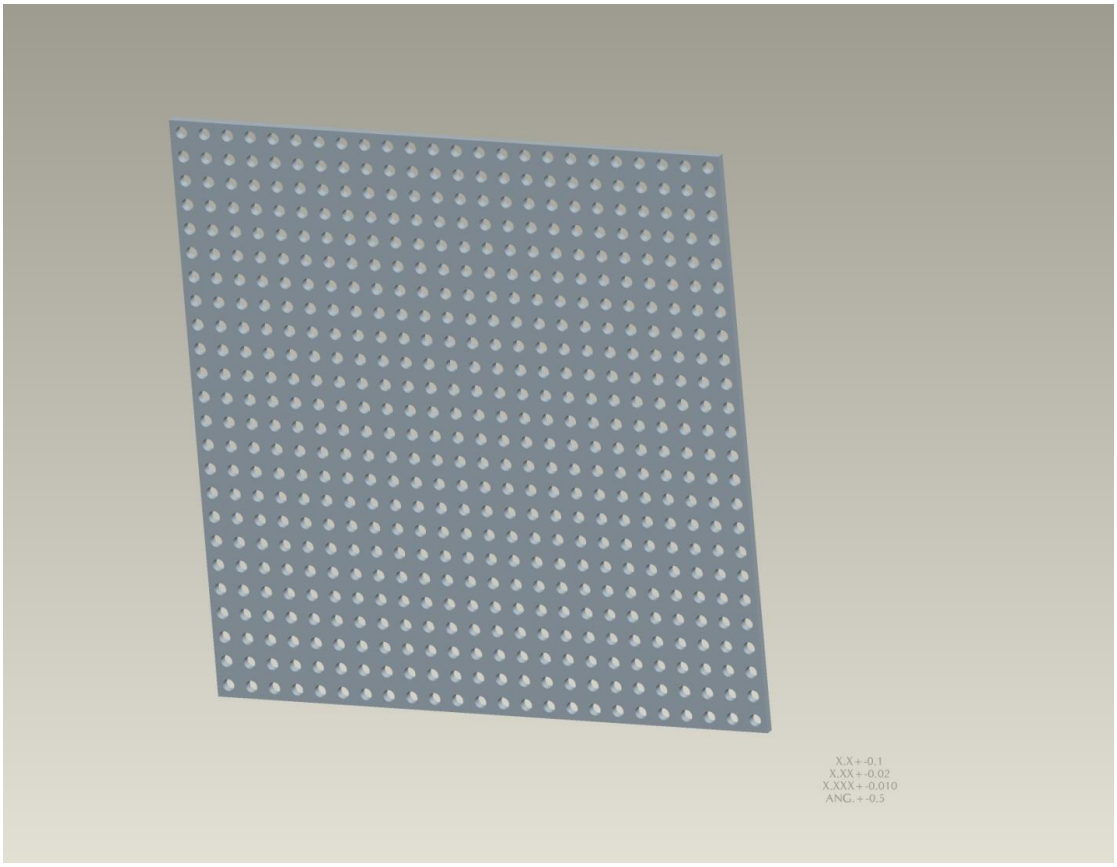

Fig. 7. CAD model of one of the perforated plates used in the experimental work.

3. Numerical Simulation

The numerical simulation required the solution of a three-dimensional, steady fluid flow. The laminar portion of the simulations is based on the full Navier-Stokes equations, while the basis of the turbulent-flow simulations is the Reynolds Averages Navier-Stokes (RANS) equations supplemented by a turbulence model. A necessary prerequisite for the implementation of any numerical simulation is the selection of the space in which the solution is to be performed. In the present situation, inspection of Figure 7 suggests that away from the outboard edges of the plate, the flow through each aperture will be the same as the flow through any other aperture. Furthermore, in light of the inherent symmetries of the flow field, the per-aperture flow can be constructed from a modular model.

This modularity is demonstrated by examination of Fig. 8. The left-hand and right-hand diagrams display clusters of apertures that respectively define square and staggered deployments of aperture centers. The blackened triangles identify a module whose repetitions characterize the entire flow field. This module receives flow from a stream tube whose origin lies upstream of the cross-sectional location of a perforated plate. The stream-tube geometry is continued downstream of the location of the plate. This concept forms the basis for the creation of the solution domain which is pictured in Fig. 9.

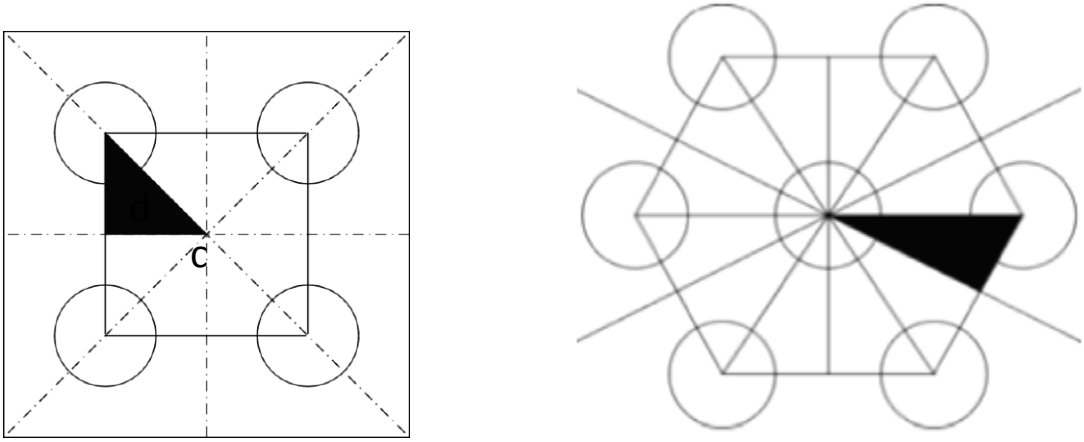

Fig. 8. Identification of modular patterns whose repetitions define the entire flow field. The left-hand and right-hand diagrams respectively correspond to the square and staggered arrays.

Fig. 9 illustrates how these symmetry modules are modeled in three-dimensional space. That figure is specific to the square array, but a similar figure can be prepared for the staggered array.

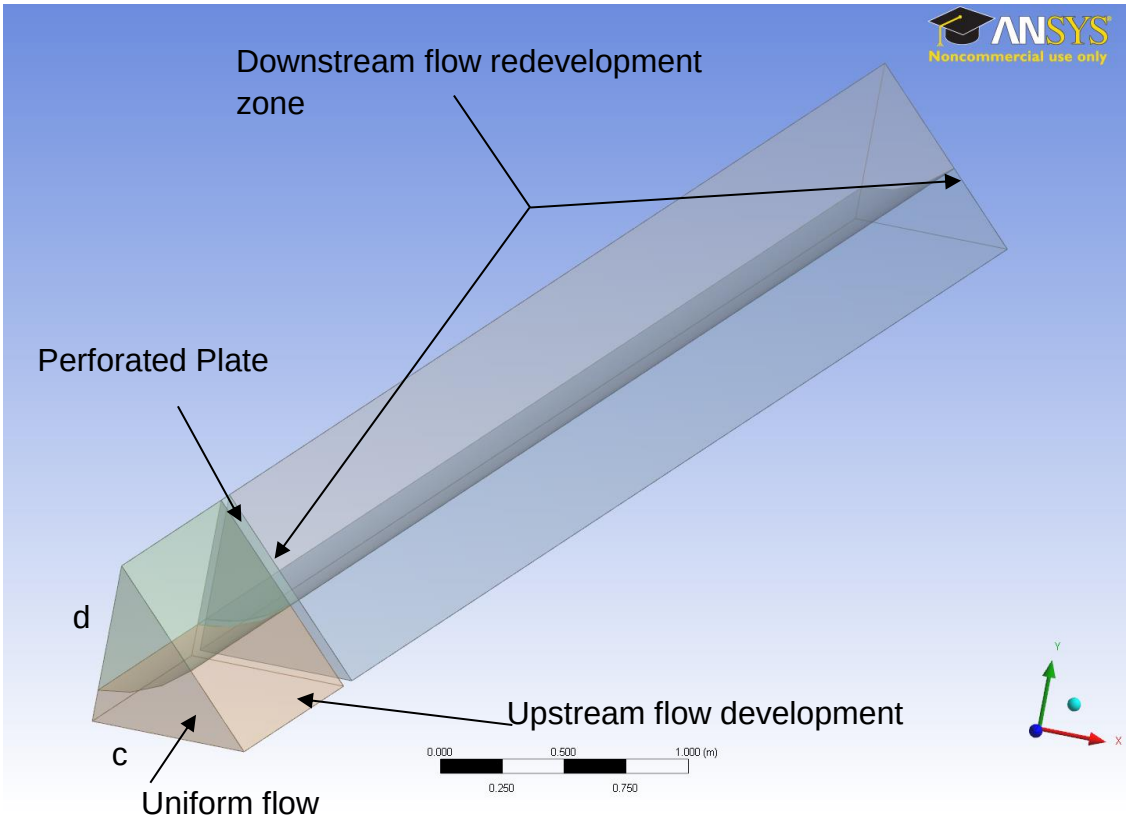

Fig. 9. Typical solution domain within which the numerical solution is implemented. The figure is specific to the square array.

As can be seen from the figure, the solution domain consists of three contiguous but discrete zones. The most upstream zone is a flow development region. Flow enters this zone with a uniform velocity profile which undergoes progressive development as the fluid recognizes the presence of the perforated plate. Numerical experiments were performed to verify that the chosen length of the upstream development zone was, in effect, infinity. The second zone contains the perforated plate. Here, the standard no-slip and impermeability boundary conditions are applied. The last of the zones lies downstream of the plate and is extended to a length at which the presence of the plate fully disappears. Once again, numerical experiments were carried out to ensure that the selected length of the downstream zone was sufficient to meet the foregoing criterion. Aside from the aforementioned conditions, the other surfaces of the solution domain are symmetry boundaries.

To quantify the various perforated-plate geometries to be considered, reference may be made to Fig. 10. This figure conveys dimensional information and identifies the cases for which simulations have been performed and results provided. The (a) through (c) parts of the figure correspond to the square array of holes while (d) through (f) parts are for the staggered array. Following Figure 10 is a table in which the respective porosities are listed for these cases.

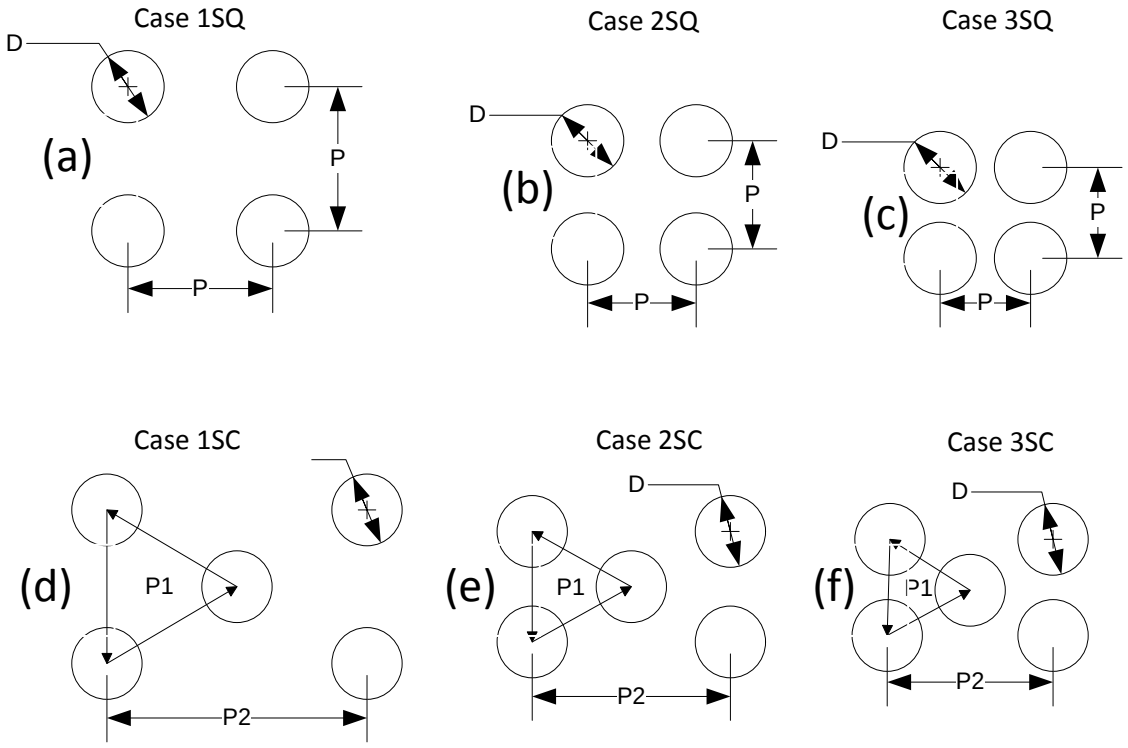

Fig. 10. Dimension layouts and identification of the cases to be considered. Square array: (a) P/D = 2, (b) P/D = 1.5, (c) P/D = 1.25. Staggered array: (d) P1/D = 2.14, P2/D = 3.70, (e) P1/D = 1.61, P2/D = 2.82, (f) P1/D = 1.34, P2/D = 2.36. These dimensional ratios apply to both the t/D = 0.5 and 1.0 perforated plates.

Table 1: Porosities of the investigated cases defined in Figure 8 for the plate thickness t/D = 0.5 and 1.0.

Case	1SQ	2SQ	3SQ	1SC	2SC	3SC
Porosity ε %	19.6	34.9	50.3	19.6	34.9	50.3

The solution domain was discretized differently in accordance with the specific geometries. Depending on the nature of the array, square or staggered, and on the porosity of the plate, it was necessary to take account of the unique geometry of each case. For each of the individual geometries, a mesh independence study was made to evaluate the sufficiency of the discretization. As a metric for the evaluation of accuracy, focus was directed to the dimensionless overall pressure drop due to the presence of the plate. When the differences in this metric varied by less than 0.2% as the number of nodes was increased, it was judged that the discretization was sufficient. The nodal count ranged from 100,000 to 500,000 depending on the specific case. In addition to mesh independence, another measure of the sufficiency of the mesh is the value of y^+ at the nodes that are nearest the wall. In general, the values of y^+ were no greater than five. The numerical calculations were performed by making use of CFX finite-volume-based software. For all of the investigated cases, a convergence criterion of 10^{-6} was enforced.

The governing equations were utilized in dimensionless form in order to reduce the number of required inputs. For the Navier-Stokes equations and the RANS equations derived there from, a nondimensionalization yields

Laminar Case:

$$\frac{\partial u_i}{\partial x_i} = 0 \qquad (1)$$

$$\rho \frac{\partial u_i}{\partial t} + \rho u_j \frac{\partial u_i}{\partial x_j} = -\frac{\partial p}{\partial x_i} + \mu \frac{\partial^2 u_i}{\partial x_j \partial x_j} + \rho f_i \quad (2)$$

Turbulent Case:

$$\rho \bar{u}_j \frac{\partial \bar{u}_i}{\partial x_j} = \frac{\partial}{\partial x_j}\left[-\bar{p}\delta_{ij} + \mu\left(\frac{\partial \bar{u}_i}{\partial x_j} + \frac{\partial \bar{u}_j}{\partial x_i}\right) - \rho\overline{u'_i u'_j}\right] + \rho \bar{f}_i \quad (3)$$

To implement Eq. (3), a turbulence model is needed to evaluate the last term in the square brackets. Based on considerable experience [34], the Shear Stress Transport (SST) model was selected. As is necessary, the selection of the turbulence model has to be validated. In the present situation, validation was achieved by experimentation.

4. Results and discussion

4.1. Laminar flow

The presentation will begin with an exposition of results that correspond to laminar friction-dominated flow. These results define the Reynolds number range that characterizes this flow regime. The simulations from which these results are extracted encompass a wide range of geometrical and flow parameters. These include two deployment patterns of the plate apertures (square and staggered), porosities ranging from approximately 20 to 50%, two relative plate thicknesses (t/D = 0.5 and 1), and aperture-based Reynolds numbers up to 20. Figure 9 was created with a view to displaying the pressure drop results for the entirety of these parameter ranges.

The figure conveys a presentation of the dimensionless pressure drop results as a function of the aperture-based Reynolds number defined as

$$Re_o = \frac{\rho U_o D}{\mu} \quad (4)$$

In this equation, U_o is the average velocity of the fluid passing through the apertures of the perforated plate, and D is the aperture diameter. For each case, a dimensionless pressure drop is defined as

$$\frac{\Delta p}{\rho U_0^2} \qquad (5)$$

The pressure drop Δp spans between the undisturbed flow upstream of the plate and a downstream location where all the effects of the presence of the plate have died away.

It can be seen in Figure 9 that the dimensionless pressure drop varies with the inverse of the Reynolds number. This relationship, when viewed in terms of physical parameters, reduces to

$$\Delta p \propto U_o \qquad (6)$$

It is well established that when the pressure drop for laminar flow is directly proportional to the velocity, the pressure drop is due to friction alone. This regime breaks down when other loss-causing processes are activated. It is seen that this regime terminates at approximately $Re_o = 20$.

The results presented in Fig. 11, when viewed carefully, reveal that larger pressure drops occur for larger plate thicknesses. The pressure drop for the thicker plate (t/D = 1) is about 50% greater than that for the thinner plate (t/D = 0.5). It is also seen that the thicker plate is more sensitive to the specifics of the hole-deployment pattern. For that plate, the pressure drop for the staggered hole pattern is approximately 21% greater than that for the square hole pattern. For the thinner of the two plates, the pressure drop shows the same trend with regard to hole-pattern distribution, but the spread between the respective results is 17%.

In retrospect, it is seen that the laminar friction-dominated pressure drops are moderately sensitive to the hole pattern and significantly sensitive to the thickness of the plate. These sensitivities are expected for laminar flows. On the

other hand, the results do not display sensitivity to the porosities over the range which characterizes the data (porosities from 19.6 to 50.3%). The plotted points include all the investigated porosities.

The connection between the aperture-based Reynolds number Re_o and the upstream Reynolds number based on the uniform velocity of approach U_∞ is

$$Re_\infty = \varepsilon Re_0 \qquad (7)$$

in which ε is the porosity of the perforated plate.

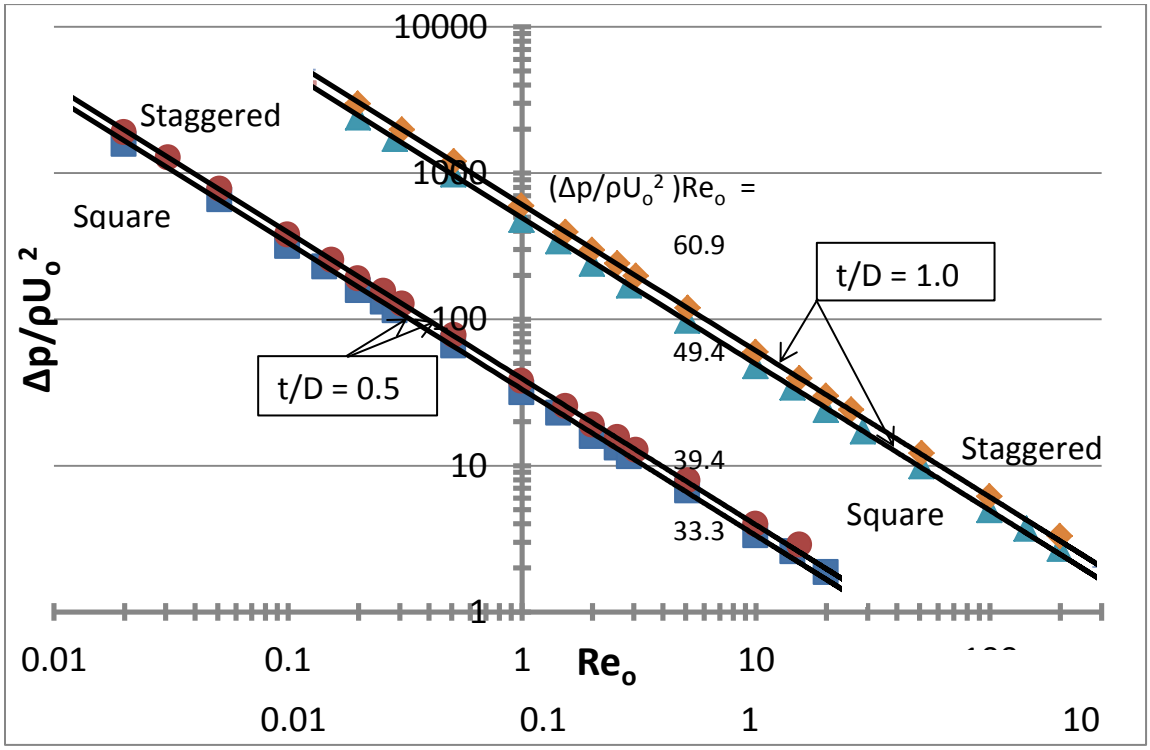

Fig. 11. Universal dimensionless pressure drop results for perforated plates with apertures deployed in square and staggered arrays, for plate thicknesses t/D = 0.5 and 1.0, and for porosities ranging from 19.6 to 50.3%. The results correspond to laminar friction-dominated flow.

The breakdown of the laminar, friction-dominated flow regime is illustrated in Fig. 12. The breakaway points are predicted by a laminar model and, therefore, do not represent the onset of turbulence.

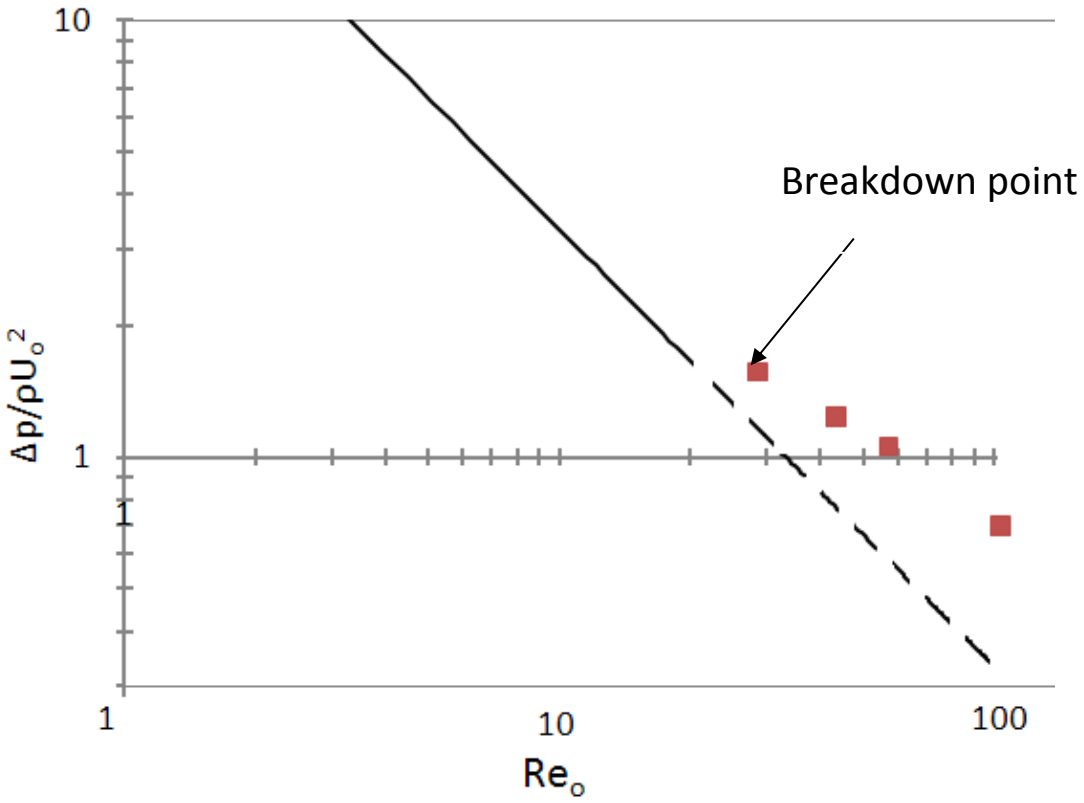

Fig. 12. Illustration of the breakdown of laminar friction-dominated flow. Square array and t/D = 0.5.

4.2. Turbulent flow

Attention is next turned to the turbulent regime. These results for this regime are presented in Figs. 13 and 14, which respectively correspond to plate thickness ratios of 0.5 and 1.0. Each figure conveys results for both the square and staggered arrays. The results are grouped according to the porosity values to which they correspond. The fully turbulent regime is identified by the insensitivity of the dimensionless pressure drop results to variations of the Reynolds number.

Also included in Fig. 13 are experimental data collected as part of this investigation. The data correspond to the thickness ratio t/D = 0.5 and to porosities of 19.6 and 34.9%. Inspection of the figure indicates that excellent agreement prevails, within 1%, between the results of the numerical simulation

and those of the experiments. A further comparison between the present simulation results and literature data can be made by making use of the Idelchik [1] compilation. As noted in the Introduction, the compilation is based on mostly unavailable Soviet works that were performed prior to 1966. Comparisons were made for both thicknesses t/D = 0.5 and 1.0. All told, six cases were chosen for comparison, and the resulting deviations were found to be 2, 4, 7, 8, 9 and 10%, with random larger and smaller results for the two sources of information. This level of agreement, considering the absence of definitive information about the sources of the data, is deemed to be highly satisfactory. In retrospect, the excellent agreement between the simulation results and those of experiment lend strong support to the turbulence model employed for the simulations.

The insensitivity of the results displayed in Figs. 13 and 14 to Reynolds number is due to the fact that the pressure drop increases with the square of the velocity. This finding indicates that the pressure drop is dominated by momentum losses. Careful inspection of Figs. 13 and 14 suggests that the flow can be regarded as fully turbulent for $Re_o > 4000$. It is also seen that the turbulent pressure drop results are virtually insensitive to whether the holes are arranged in either square or staggered patterns. A comparison between Figs. 13 and 14 reveals that the pressure drop results are highly sensitive to the plate thickness, with the *higher pressure drops belonging to the thinner plate*. This outcome may be regarded as unexpected, especially since the laminar pressure drop results were larger

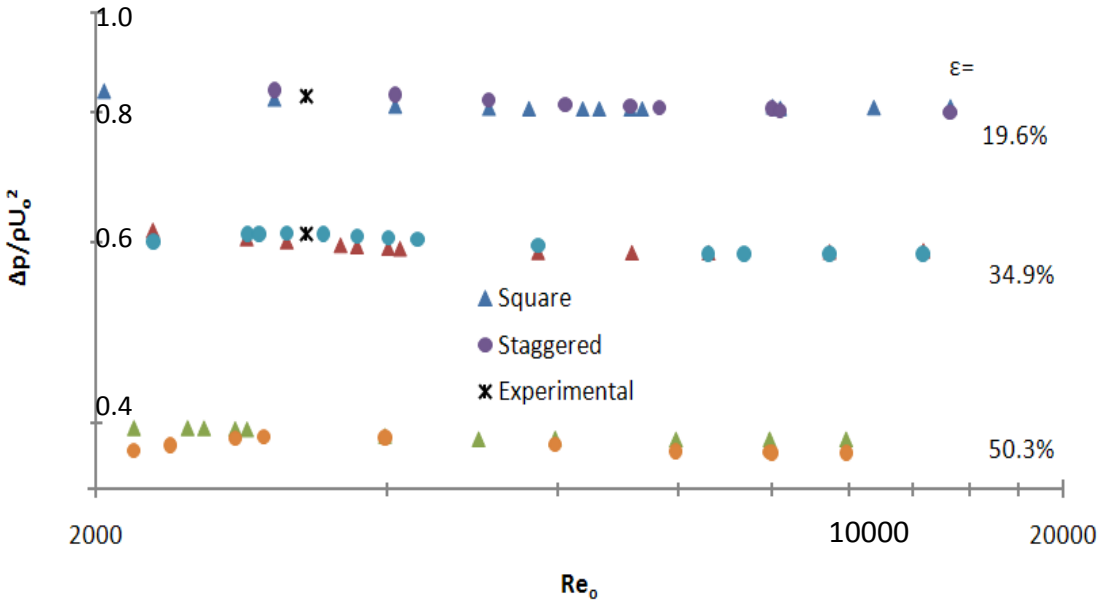

Fig. 13. Turbulent-flow pressure drops for the plate thickness t/D = 0.5, for the square and staggered hole deployments, and for porosities between 20 and 50%.

for the thicker plate than for the thinner plate. This issue will be resolved shortly, after a correlation of the turbulent-flow pressure drops is presented.

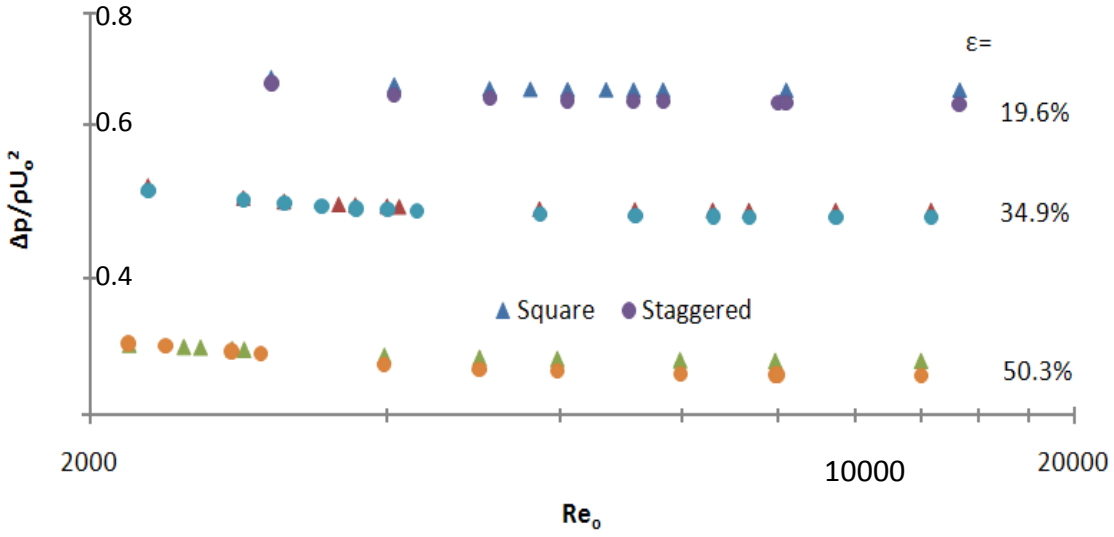

Fig. 14. Turbulent-flow pressure drops for the plate thickness t/D = 1, for the square and staggered hole deployment, and for porosities between 20 and 50%.

The fully turbulent results displayed in Figs. 13 and 14 are brought together in Fig. 15. In this figure, the results for the two plate thicknesses and the two hole layouts are presented as a function of the porosity. These results are independent of the Reynolds number as already been established. Inspection of the figure shows that the thickness

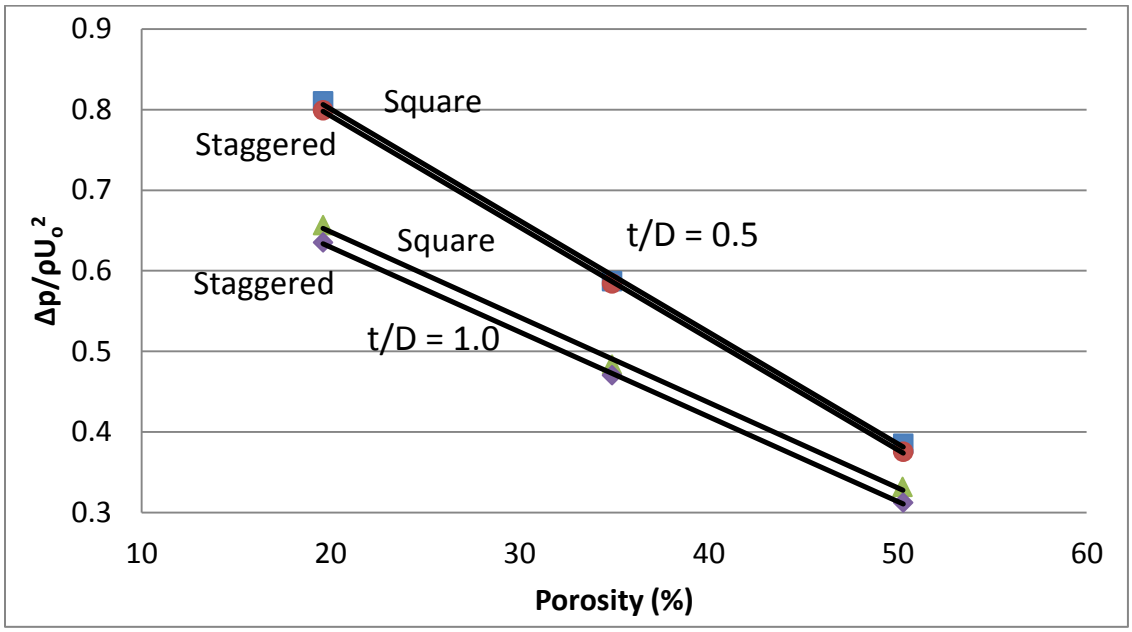

Fig. 15. Universal dimensionless turbulent pressure drop results for perforated plates with apertures deployed in square and staggered arrays, for plate thicknesses t/D = 0.5 and 1.0, and for porosities ranging from 19.6 to 50.3%.

variation has the greatest impact on the results, with the hole layout being of secondary importance. The presentation corroborates the already identified finding that the thinner plate gives rise to a greater pressure drop than does the thicker plate. Not only does the thinner plate display a higher pressure drop, but also the dependence of the pressure drop on the porosity is greater than that for the thicker plate. The results for the two plate thicknesses can be expressed algebraically as

$\Delta p/\rho U_o^2 = 1.072 - 0.0138\varepsilon$, t/D = 0.5

$\Delta p/\rho U_o^2 = 0.8484 - 0.0155\varepsilon$, t/D = 1.0

These equations apply for $Re_o > 4000$, for porosities between 19.6 and 50.3%, and for both the square and staggered arrays.

4.3. Flow separation

The pattern of fluid flow within the aperture bore is strongly affected by flow separation and subsequent reattachment. The onset and termination locations of the recirculation zone that is situated in the bore is presented in Tables 2 and 3, respectively for the laminar friction-dominated and turbulent cases. The table lists the locations in terms of the dimensionless ratio x/D, where x = 0 at the upstream face of the perforated plate.

To illustrate the flow pattern, a color-contour diagram is presented in Fig. 16. This information pertains to turbulent flow. Inspection of the figure shows flow separation and subsequent reattachment at the upstream end of the flow passage. At the downstream end of the passage, the flow expands and spawns a large recirculation zone.

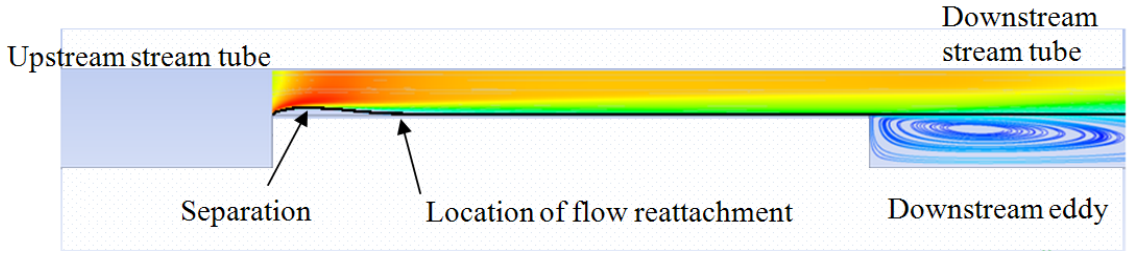

Fig. 16. Pattern of fluid flow showing the physical processes of separation and reattachment near the upstream end of the flow passage end the formation of a large eddy downstream of the plate.

Attention may first be focused on the laminar case. For the thinner plate (t/D = 0.5), Table 2, the length of the separated region extends from x/D of about 0.05 to 0.45, independent of the Reynolds number and the porosity. Therefore, most

of the aperture bore experiences recirculation. Results for the thicker plate (t/D = 1.0) are also displayed in Table 3. Once again, the onset and the termination of the separated region are independent of the Reynolds number and porosity. The length of the separated region extends between x/D of 0.07 and 0.93. It is clear that the bore of the thicker plate has a much longer recirculation region than does the thinner plate. It is believed that the higher pressure drop experienced by the former is directly related to the greater length of the recirculation zone.

Table 2: Locations x/D marking the onset and termination of flow separation for laminar friction-dominated flow

	t/D = 0.5		t/D = 1.0	
Re_o	Onset	Termination	Onset	Termination
0.2	0.05	0.45	0.07	0.93
0.5	0.06	0.44	0.07	0.93
5	0.06	0.44	0.07	0.93
10	0.06	0.44	0.07	0.93
20	0.05	0.44	0.07	0.92

Focus will now be directed to the turbulent flow situation for which information about the onset and termination of recirculation is listed in Table 3. For the thinner plate, the onset of separation is at x/D = 0.02 for all of the investigated Reynolds numbers and porosities. However, the recirculation zone does not close within the length of the bore. For the thicker plate, the initiation of separation occurs approximately at the same location as for the thinner plate. On the other hand, the recirculation zone for the thicker plate does reattach within the length of the bore at a value of x/D of 0.90.

The different characteristics of the respective recirculation zones for turbulent flow for the thinner and thicker plates is believed to be the decisive factor in giving rise to a higher dimensionless pressure drop for the former. The critical characteristic is that the recirculation zone for the thinner plate does not close

within the confines of the bore, while the thicker-plate recirculation zone is fully contained within the bore. The issue of closure versus non-closure is believed to have a major effect on the nature of the wake downstream of the plate. It is apparent that the non-closed recirculation zone creates a much more chaotic wake than does the closed recirculation zone. This chaotic wake motion definitely is a source of higher pressure drop. This phenomenon is the major reason for the thinner-plate pressure drop to be larger than that of the thicker plate.

Table 3: Locations x/D marking the onset and termination of flow separation for turbulent flow

	t/D = 0.5		t/D = 1.0	
Re_o	Onset	Termination	Onset	Termination
7500	0.02	>0.5	0.03	0.90
10000	0.02	>0.5	0.03	0.90
15000	0.02	>0.5	0.03	0.90
20000	0.02	>0.5	0.03	0.90
25000	0.02	>0.5	0.03	0.90

4.4. Downstream Length of the Plate-Induced Flow Disturbance

In practice, it is not uncommon for more than one perforated plate to be used to achieve flow homogenization. The effectiveness of two or more plates is sensitive to whether or not the second or subsequent plates are washed by the wake of upstream-positioned plates. To enable the logical positioning of additional plates beyond the first, information will now be provided for the downstream length which marks the termination of the effect of the presence of an upstream plate. Since the downstream flow disturbance due to a perforated plate dies away asymptotically, it is appropriate to define a practically relevant downstream length. Here, that length is defined as the distance L from the downstream face of the plate at which the dimensionless pressure drop has achieved 95% of its full value.

Fig. 17 presents the downstream length L for laminar friction-dominated flow in a dimensionless ratio with respect to the diameter D. Inspection of the figure shows that the downstream length at which the flow disturbance becomes negligible is on the order of one diameter. There are minor effects of porosity and of the pattern of hole deployment which are of marginal practical significance.

Corresponding information for turbulent flow is presented in Fig. 18. It is seen that the downstream lengths fall in the range of 5-6 diameters. The downstream lengths for the thicker plate are approximately half a diameter greater than those for thinner plates. If a typical bore diameter is 6 mm, than the plate-induced disturbances terminate at approximately 30 to 35 mm downstream of the plate.

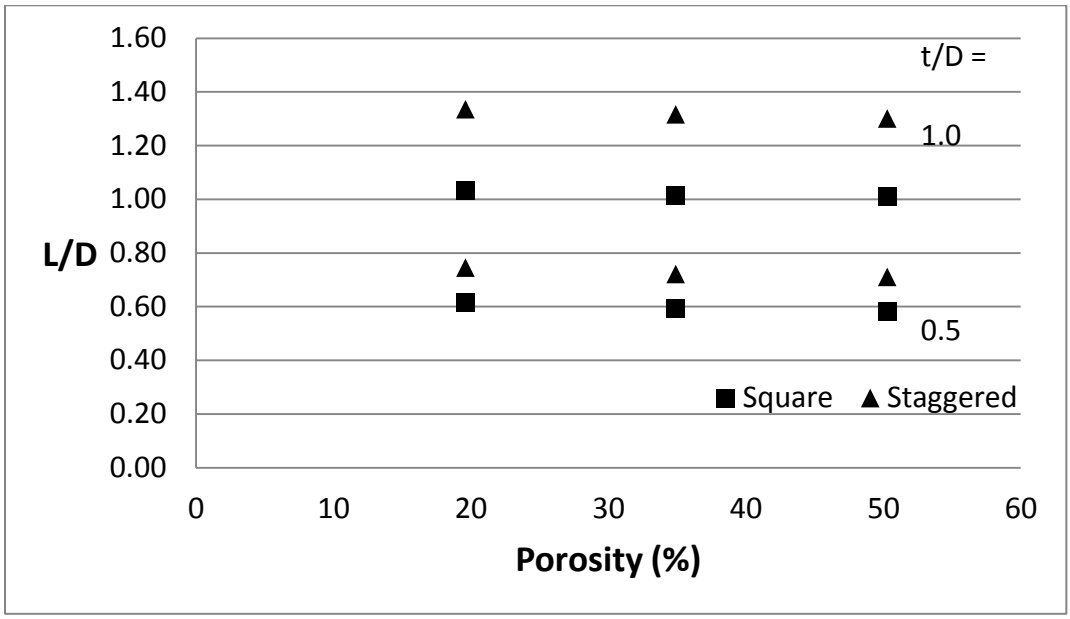

Fig. 17. Downstream length for the cessation of plate-induced flow disturbances for laminar friction-dominated flow.

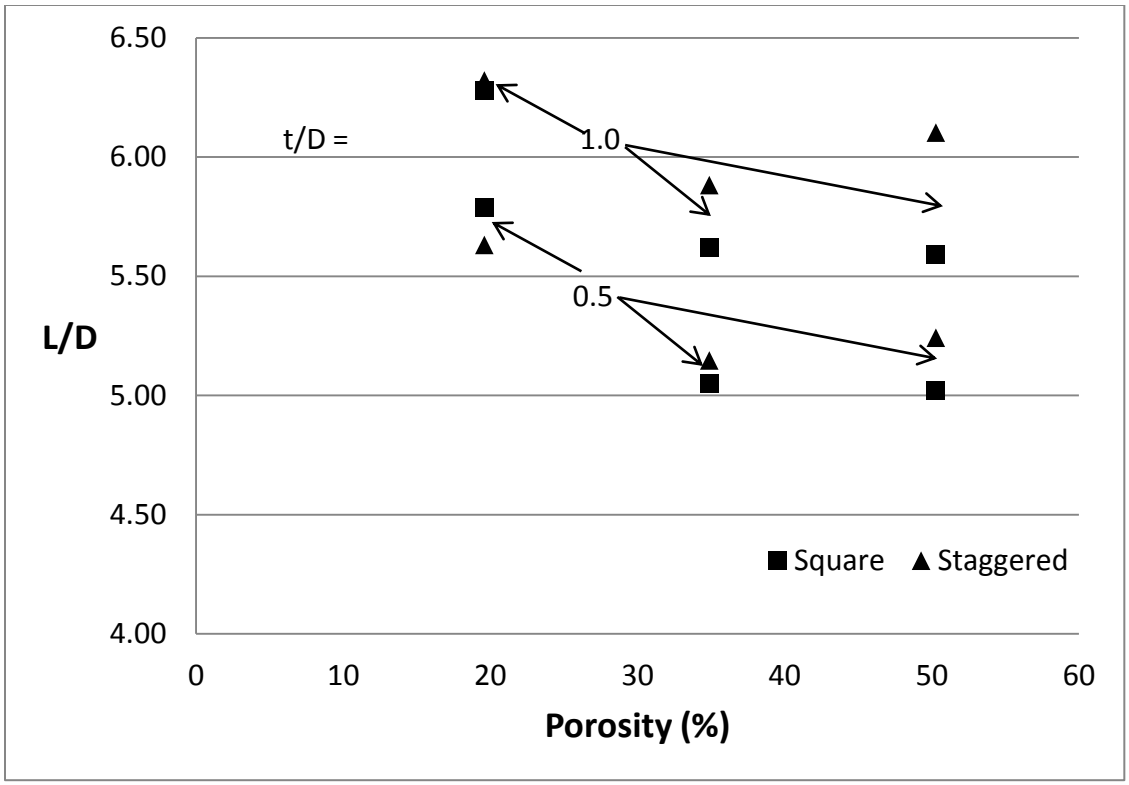

Fig. 18. Downstream length for the cessation of plate-induced flow disturbances for turbulent flow.

5. Uncertainty analysis on experimental results

Prior to the execution of the experiments described in Chapter 2, an uncertainty analysis was performed to estimate the expected accuracy of the results. The goal of that analysis was to identify the importance of various measurements and to gain guidance as to which of the measurements required special attention. Since, the evaluation of uncertainty can be a time and resource consuming process, well established analysis techniques, particularly regarding statistical analysis, were followed in this research.

A method of estimating uncertainty in experimental results has been presented by Kline and McClintock [35]. This method is based on a careful specification of the individual uncertainties present in various primary experimental measurements. To be specific, an uncertainty analysis will be performed on the expected accuracy of the Reynolds number.

In the present work, a Pitot tube is used to determine the wind tunnel velocity by means of the measured difference between the static and impact pressures Δp_p, where the subscript p denotes Pitot. Since the first focus of this analysis is on the Reynolds number, the natural starting point is its definition.

$$Re = \frac{\rho U D}{\mu} \tag{1}$$

In this equation, *U* is the wind tunnel velocity, D is the diameter of the apertures in the perforated plate, and ρ and μ are the density and viscosity of the flowing fluid.

Since the velocity *U* is obtained from the Pitot tube by means of the equation,

$$U = \sqrt{\frac{2\Delta p_p}{\rho}} \tag{2}$$

The substitution of Eq. (2) into Eq. (1) leads to

$$Re = \frac{\sqrt{2}\sqrt{\Delta p_1}\sqrt{\rho}D}{\mu} \tag{3}$$

Hence, it can be said that the Reynolds number is a function of pressure difference, density, dynamic viscosity, and diameter. In formal terms,

$$Re=f(\rho,\mu,D,\Delta p_p) \tag{4}$$

The uncertainty in the value of the Reynolds number can be determined from the well-established Eq. (5) [36],

$$w_{Re} = \sqrt{\left(\frac{\partial Re}{\partial \Delta P} w_{\Delta P}\right)^2 + \left(\frac{\partial Re}{\partial \rho} w_\rho\right)^2 + \left(\frac{\partial Re}{\partial \mu} w_\mu\right)^2 + \left(\frac{\partial Re}{\partial D} w_D\right)^2} \tag{5}$$

where the symbol *w* denotes the uncertainty.

To proceed, it is necessary to evaluate the partial derivatives that appear in Eq. (5).

The relevant partial derivatives are,

$$\frac{\partial Re}{\partial \Delta P} = \frac{\sqrt{2\rho}D}{\mu} \tag{6a}$$

$$\frac{\partial Re}{\partial \rho} = \frac{\sqrt{2\Delta p}D}{\mu} \tag{6b}$$

$$\frac{\partial Re}{\partial D} = \frac{\sqrt{2\Delta P\rho}}{\mu} \tag{6c}$$

$$\frac{\partial Re}{\partial \mu} = -\frac{\sqrt{2\Delta P\rho}D}{\mu^2} \tag{6d}$$

A more instructive form of Eq. (5) is to rephrase the equation in the form of w_{Re}/Re.

The introduction of the partial derivatives from Eqs. (6) and subsequent dividing by Re gives

$$\frac{w_{Re}}{Re} = \sqrt{\left(\frac{w_{\Delta P}}{\sqrt{\Delta P}}\right)^2 + \left(\frac{w_\rho}{\sqrt{\rho}}\right)^2 + \left(\frac{w_D}{D}\right)^2 + \left(-\frac{w_\mu}{\mu}\right)^2} \qquad (7)$$

Also needed for the evaluation Eq. (5) are the uncertainties *w* for the four quantities that appear on the right hand side of the equation. Careful consideration of the instrumentation led to the following estimates:

- ✓ Uncertainty of pressure difference, $w_{\Delta P}$ = ±0.125 Pa
- ✓ Uncertainty of density [35]; w_ρ = ± 0.47% or ±5.36x10^{-3} kg/m^3
- ✓ Uncertainty of diameter [35]; w_D = ± 0.1-0.2% or ± 9.53x10^{-6} m
- ✓ Uncertainty of dynamic viscosity [35]; w_μ = ± 0.1-0.2%, or ±2.76x10^{-8} kg/m-sec

In addition, the values of Δp_p, D, ρ, and μ are needed. For the application in question, they are

Δp_p = 0.022 inches of H_2O = (0.022*248.82) Pa = 5.41 Pa

D = 0.00635 m

ρ = 1.14 kg/m^3

μ = 1.84x 10^{-5} kg/m-sec

When all of the available information is introduced into Eq. (7), there is obtained

$$\frac{w_{Re}}{Re} = \sqrt{\left(\frac{0.125}{\sqrt{5.41}}\right)^2 + \left(\frac{5.36x10^{-3}}{\sqrt{1.14}}\right)^2 + \left(\frac{9.53x10^{-6}}{0.00635}\right)^2 + \left(-\frac{2.76x10^{-8}}{1.84x10^{-5}}\right)^2} = 0.054\%$$

This outcome states that the fractional uncertainty in the Reynolds number is about 1/20 of one percent.

6. Concluding remarks

The goal of the investigation set forth here is to examine the flow characteristics of perforated plates in a manner that is both more fundamental but also of more practical utility compared with the published literature on the subject. Two different plate thicknesses were considered as well as two different hole patterns. The porosity of the plate was also varied over the practical range.

A number of new results have emerged from this investigation. The Reynolds number ranges that define laminar friction-dominated flow and fully turbulent flow have been identified for the first time. For the laminar regime, the pressure drop varies linearly with the Reynolds number. Among the geometrical parameters, the plate thickness is dominant, with the pressure drop for the thicker plate being substantially greater than for the thinner plate. The staggered hole pattern gives rise to a higher pressure drop than does the square hole pattern, and higher porosities lead to lower pressure drops. All of these characteristics were well correlated to provide universal results.

For the turbulent case, the pressure drop was shown to depend on the square of the Reynolds number, indicating the dominance of momentum-based losses. Once again, the plate thickness was the most important of the geometrical parameters. Remarkably, it was found that the pressure drop is smaller for the thicker plate than for the thinner plate. A careful investigation of the pattern of fluid flow within the respective apertures disclosed that the absence of reattachment of a recirculation zone was the factor that gave rise to the higher pressure drop for the thinner plate. The influence of the pattern of hole distribution was found to be of minor significance, and, as expected, the magnitude of the pressure drop correlated inversely with the porosity.

The aforementioned results unearthed both fundamental flow behaviors and provided information for engineering design. Another design issue is the potential use of more than one perforated plate to achieve the desired flow control. In this

regard, it is of importance to assess possible interactions between successive perforated plates. A critical issue in this assessment is the downstream distance from a plate at which the plate-induced flow disturbances die away. For the laminar friction-dominated regime, those disturbances effectively ceased to exist at a distance of approximately one hole diameter downstream of the plate. On the other hand, about five hole diameters were required to dampen the disturbances for the case of turbulent flow.

CHAPTER 3: PERFORATED PLATES FOR FLUID MANAGEMENT: PLATE INCLINATION EFFECTS AND FLOW REGIMES

1. Introduction

Perforated surfaces are frequently encountered in applications involving flowing fluids. Prominent among these applications is flow control and its many facets, including homogenization of maldistributed flow, drag increase and speed brakes for aircraft flight control, reduction of jet noise, lift augmentation, attenuation of the onset of cavitation in liquid pipeline flows, insect control for greenhouse applications, automotive cooling systems, and many others. This plethora of applications has evoked a substantial literature. The segment of that literature that relates to flat perforated plates is of particular relevance here. For that highly relevant situation, it appears that the prior publications have focused almost exclusively on flows that impinge perpendicular to the plate surface, whereas non-perpendicular impingement has been given little consideration.

The motivation for the present investigation is control and tracking of flows that impinge on flat perforated plates at an angle of attack. In the situations considered here, flat perforated plates are positioned in rectangular ducts of various aspect ratios and at several angles of attack. Both laminar and turbulent flows are investigated by means of numerical simulation. Such flows are intrinsically three dimensional and execute a complex trajectory as they turn to enter and leave the open areas of the plate. As many as three distinct zones of flow separation appear to be possible. The work will have a dual focus of determining results of direct practical utility and exploring fundamental fluid-flow processes.

Although the literature search did not unearth prior work on flows inclined at an angle of attack to flat perforated plates situated in rectangular ducts, other situations were encountered that involved inclined flows and perforated surfaces. Yavuzkurt [37] experimentally determined the pressure drop experienced by flow in a round pipe in which a circular perforated plate was positioned at an angle of attack to the pipe axis. The layout pattern of holes in a circular plate differs markedly from the uniform pattern that is standard in rectangular configurations. In [38], the cross section of a rectangular wind tunnel was subdivided into an upper and lower half. The upper half was fully unobstructed while the lower half contained a flat perforated plate at an angle of attack. In a similar cross-section partitioning, a solid baffle replaced the perforated plate [39]. A flat plate with a single centered round hole was impinged by a flow at an angle of attack and the corresponding pressure determined Guo [40].

A woven-wire screen on which an inclined flow impinged was studied by Brundrett [41]. Similarly, Gerova [42] investigated a heat exchanger application involving inclined screens and honeycombs. In aerodynamic applications, permeable flaps and deflectors have been evaluated as means for jet noise reduction [43] and control of drag [44]. The use of aircraft drag brakes is phenomenologically related to a perforated plate impinged at an angle of attack [45, 44]. In a unique application, screens inclined to the flow direction have been used to control both turbulence level and downwash on the flight deck of a naval vessel from which aircraft take off and land [46]. Those applications involve oblique but uncontrolled impingement.

Screens also see service for control of turbulence intensity, and [47] is representative of the work in that area.

2. Numerical Simulation

2.1 Physical model and solution strategy

As was discussed in the Introduction, the fluid mechanics of flat perforated plates at angle of attack has not been treated in the published literature, while the companion problem of perpendicular incidence has been extensively studied. This state of affairs may well be due to the relative complexity of the two situations. Based on prevailing symmetries, the case of perpendicular incidence may be treated by focusing only on a single aperture among the multitude that constitute the perforated plate. Neither the dimensions of the plate cross section nor those of the host duct need be considered. In contrast, for the plate at angle of attack, consideration must be given to the entire cross section of the plate, taking account of plate and duct-wall interactions and the dimensions of the plate and duct cross sections.

The goal of this research is to determine both the fundamental fluid flow processes and results of practical utility relating to perforated plates at angle of attack. This goal was accomplished by means of computational fluid dynamics. The numerical simulations modeled the three-dimensional, steady-state fluid flow encompassing both the laminar and turbulent regimes. The full Navier-Stokes equations were solved for the laminar-flow simulations whereas the turbulent-flow simulations were accomplished by solving the RANS equations supplemented by a suitable turbulence model.

An isometric CAD drawing has been created and displayed in Fig. 19 to clarify the physical situation. As seen there, the plate is situated within a rectangular duct of accommodating dimensions. Note that the corners of the plate fit precisely into the corners of the duct. The corners are numbered to facilitate a discussion of the spatial modeling of the plate.

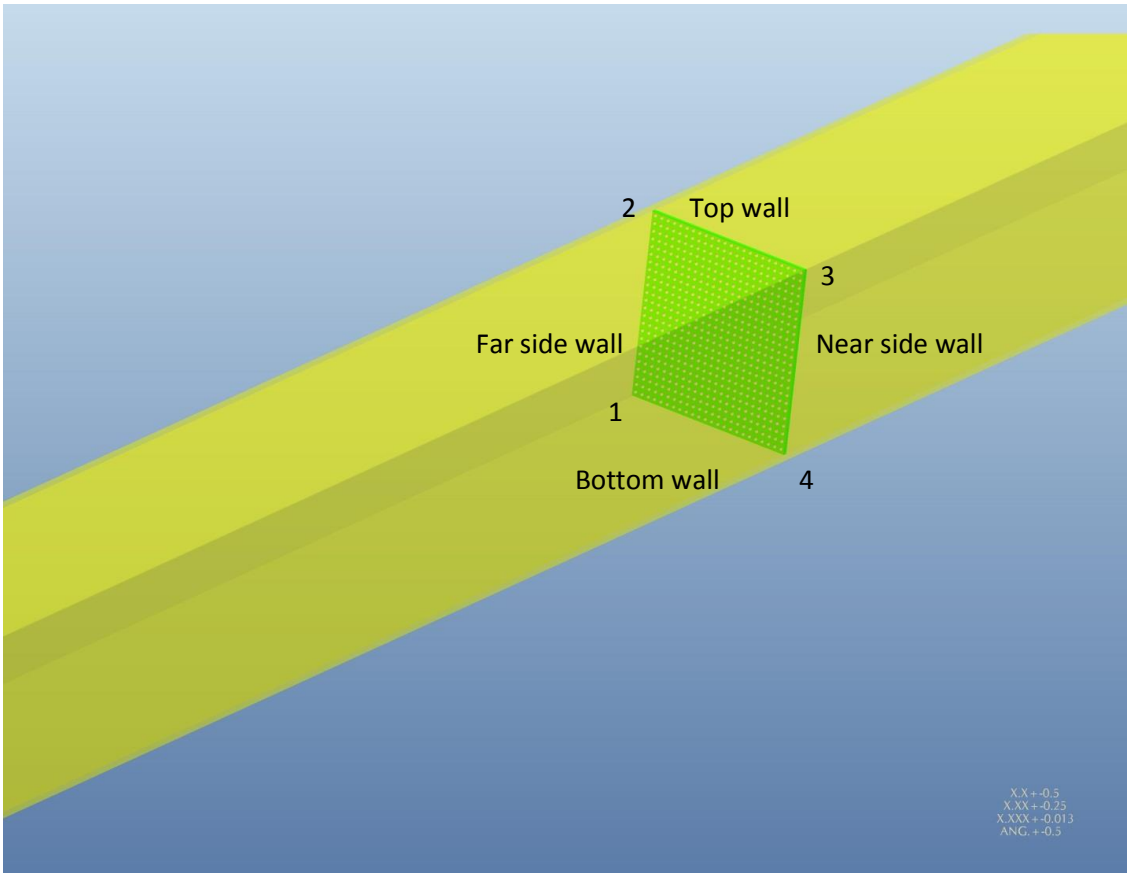

Fig. 19. Isometric CAD Model of the inclined perforated plate positioned in a duct.

The simulation strategy will be elaborated with the aid of Fig. 20. That figure is a head-on view of the perforated plate, with corners numbered as in Fig. 19. The side edges of the plate, 12 and 34, are in intimate contact with the side walls of the duct, and the top and bottom edges, 23 and 41 respectively, are also in intimate contact with their contiguous duct walls. Aside from the vertical arrays of holes adjacent to the side edges 12 and 34, it can be argued that all other vertical arrays of holes are oblivious to the presence of the side walls. This is certainly true for vertical arrays of holes that are situated midway between the side walls.

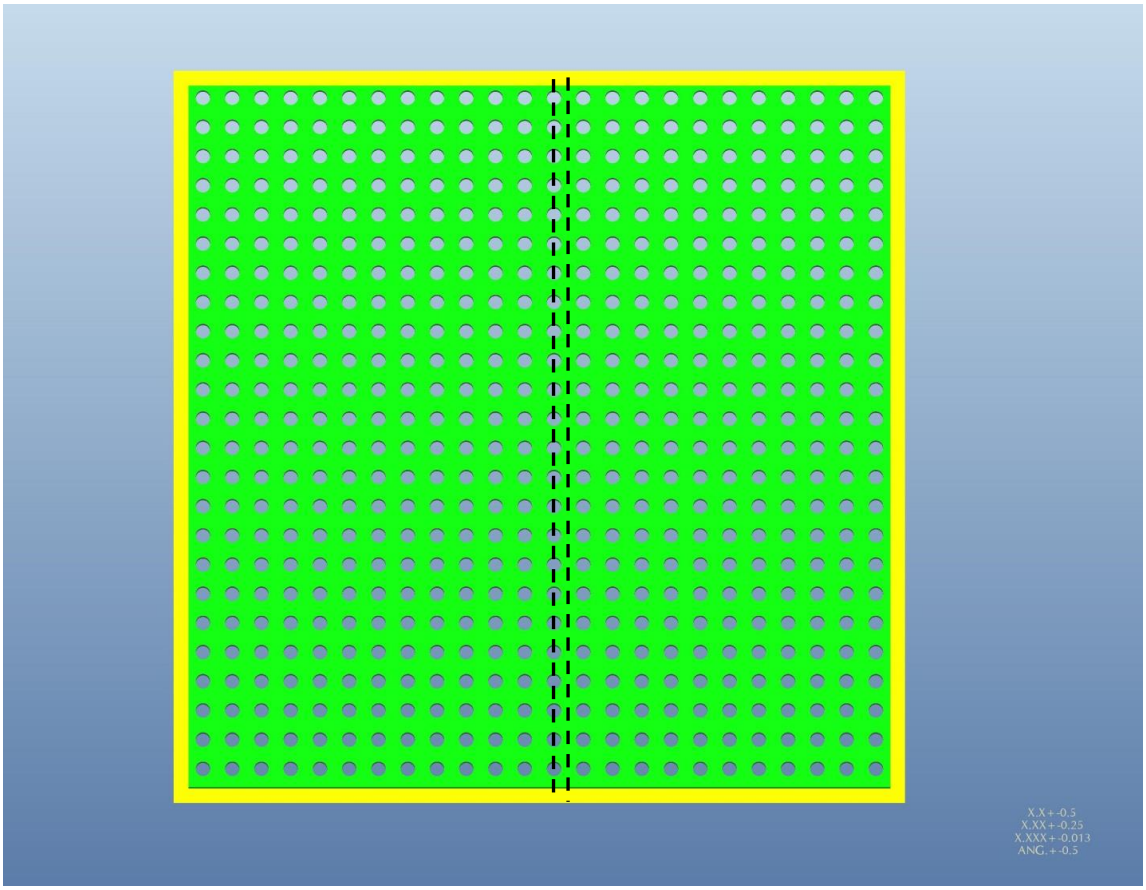

Fig. 20. Head-on view of a perforated plate including features to elucidate the description of the solution strategy.

This reasoning leads to the identification of the portion of the plate that has been selected to be included in the numerical simulation model. That portion is defined by the space confined between dashed symmetry lines in Figure 20.

2.2 Mathematical model

The goal of this investigation is to simulate the fluid flow in all regimes: laminar, intermittent, and turbulent. The starting point of the laminar flow simulations is the three-dimensional, incompressible, constant-property Navier-Stokes equations supplemented by the equation of continuity. For the intermittent and turbulent regimes, the simulations are based on the RANS, the continuity equation, and supplementary equations for a turbulence model and for a

damping function to facilitate the intermittent regime. The governing equations for the laminar flow case are set forth in Chapter 2. Here, attention will be focused on the turbulent-flow. The starting point is the RANS generalization of the Navier-Stokes equations. These equations are

$$\rho\left(u_i \frac{\partial u_j}{\partial x_i}\right) = -\frac{\partial p}{\partial x_i} + \frac{\partial}{\partial x_i}\left((\mu + \mu_{turb})\frac{\partial u_j}{\partial x_i}\right) \quad j = 1,2,3 \tag{1}$$

As written, these equations are applicable for incompressible flow with constant viscosity. The quantity μ_{turb} is the turbulent viscosity, which is a facsimile of the Reynolds stress terms. In the RANS formulation, turbulence isotropy is intrinsic. These equations are supplemented by the equation of continuity

$$\frac{\partial u_i}{\partial x_i} = 0 \tag{2}$$

The choice of a suitable turbulence model will now be addressed. There are a number of two-equation models that are available to supplement the RANS equations. Upon due consideration, the SST model, due to Menter [48], was chosen The several reasons for this choice are: (a) its prediction for pressure drop for normal impingement was verified by experiment (Chapter 2), (b) it auto-transforms to laminar flow for suitably small Reynolds numbers, and (c) it has been extended to deal with the intermittent flow regime. The SST model is a merging of two other well-established turbulence models, the κ-ε and the κ-ω models. SST combines the respective accuracies of the κ-ω model near the wall and the κ-ε model in the free stream.

The equations of the SST model are partial differential equations for the turbulence kinetic energy κ and the turbulent eddy frequency ω. They are

$$\frac{\partial(\rho u_i \kappa)}{\partial x_i} = \gamma \cdot P_\kappa - \beta_1 \rho \kappa \omega + \frac{\partial}{\partial x_i}\left[\left(\mu + \frac{\mu_{turb}}{\sigma_\kappa}\right)\frac{\partial \kappa}{\partial x_i}\right] \tag{3}$$

$$\frac{\partial(\rho u_i \omega)}{\partial x_i} = A\rho S^2 - \beta_2 \rho \omega^2 + \frac{\partial}{\partial x_i}\left[\left(\mu + \frac{\mu_{turb}}{\sigma_\omega}\right)\frac{\partial \omega}{\partial x_i}\right] + 2(1-F_1)\rho \frac{1}{\sigma_{\omega 2}\omega}\frac{\partial \kappa}{\partial x_i}\frac{\partial \omega}{\partial x_i} \tag{4}$$

The solution of Eqs. (3) and (4) yields the values of κ and ω, which give the turbulent viscosity μ_{turb} from

$$\mu_{turb} = \frac{\alpha \rho \kappa}{\max(\alpha\omega, SF_2)} \tag{5}$$

In the intermittent flow regime, turbulence is partially damped. Menter [48] created a damping model which has been tested for both internal and external flows. The key outcome of that model is the damping parameter γ. It is a quantity whose value is between 0 and 1. It multiplies the turbulence production term P_k on the right-hand side of Eq. (3). The equations for the damping parameter are

$$\frac{\partial(\rho u_i \gamma)}{\partial x_i} = P_{\gamma,1} - E_{\gamma,1} + P_{\gamma,2} - E_{\gamma,2} + \frac{\partial}{\partial x_i}\left[\left(\mu + \frac{\mu_{turb}}{\sigma_\gamma}\right)\frac{\partial \gamma}{\partial x_i}\right] \tag{6}$$

and

$$\frac{\partial(\rho u_i \Pi)}{\partial x_i} = P_{\Pi,t} + \frac{\partial}{\partial x_i}\left[\sigma_{\Pi,t}(\mu + \mu_{turb})\frac{\partial \Pi}{\partial x_i}\right] \tag{7}$$

These equations contain numerous unique symbols, so that a symbol list is appropriate at this point.

Nomenclature

A	model constant
$E_{\gamma 1}$, $E_{\gamma 2}$	intermittency destruction terms
F_1, F_2	blending functions in the SST model
P_k	production term for the turbulent kinetic energy
$P_{\gamma 1}$, $P_{\gamma 2}$	intermittency production terms
$P_{\Pi,t}$	production term for the transition onset Reynolds number
S	absolute value of the shear strain rate
u	local velocity
x_i	tensor coordinate direction
α	SST model constant
$\boldsymbol{\gamma}$	damping parameter
β_1, β_2	SST model constants
ω	turbulent eddy frequency
$\boldsymbol{\kappa}$	turbulence kinetic energy
μ	molecular viscosity
μ_{turb}	turbulent viscosity
σ	Prandtl-number-like diffusion coefficient
γ	damping factor
ρ	fluid density
Π	turbulent adjunct function

2. 3 Boundary conditions

To complete the mathematical description of the problem, boundary conditions have to be specified in the space upstream of the perforated plate where the flow is not disturbed by the presence of the plate and at a sufficient downstream distance where the plate-generated disturbances have died away. The other relevant boundary conditions are no-slip and impermeability at all solid surfaces. To establish the upstream boundary condition, supplementary numerical solutions were performed for flow in the containment duct in the absence of the perforated plate. These solutions were run for a sufficiently great length of duct to assure the attainment of fully developed flow. The thus-determined fully developed velocity profiles were used as the upstream boundary condition and were applied at a location that is 24 plate-hole diameters upstream from the leading edge of the inclined plate. The location for applying the downstream boundary condition was determined from computer runs with the perforated plate in place. At that location, the very weak condition was applied that all streamwise second derivatives of the velocities be zero. In addition, the (gauge) pressure was specified to be zero.

A representative solution domain is presented in Figure 21. As can be seen from the figure, there are three discrete but connected parts of the domain. The entry region is the upstream zone. Flow is initialized at the entrance of this zone with the fully developed velocity-profile results from the numerical simulation of the flow in the containment duct in the absence of the perforated plate. The second zone is the one occupied by the inclined perforated plate, and the no-slip and impermeable wall conditions were applied in this zone as the boundary condition. The top and bottom duct walls also have the same no-slip and impermeability boundary condition. The region downstream of the perforated plate in which the flow recovers from plate-based disturbances completes the solution domain. The remaining bounding surfaces of the solution domain are the symmetry lines displayed in Figure 20 and the outflow cross section at the downstream end.

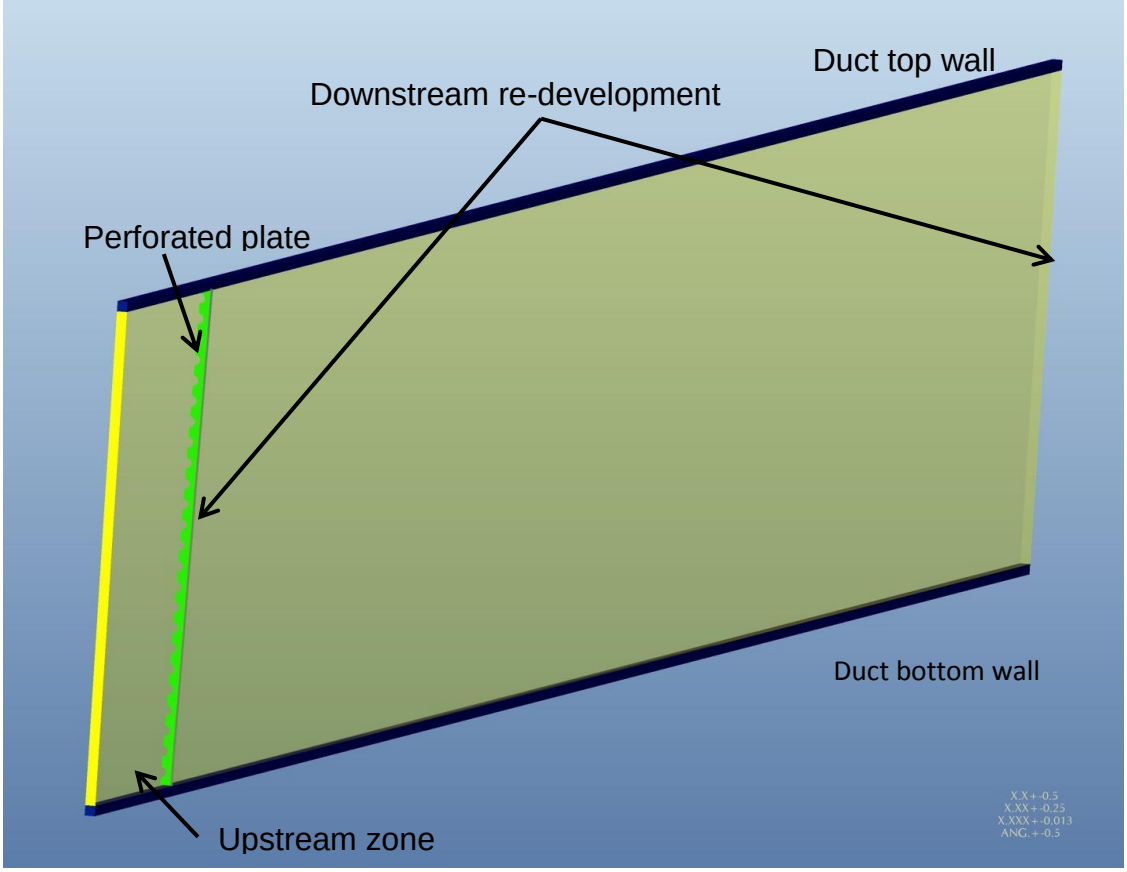

Fig. 21. Representative solution domain. The figure is specific to the five-degree inclined perforated plate.

2. 4 Model discretization

The partial differential equations encountered in this numerical simulation were solved by employing the ANSYS CFX 14.0 software. The discretization of the partial differential equations was performed via the application of the finite-volume method. The solution domain was meshed by between 3,000,000 and 4,000,000 nodes for the different cases that were investigated. A mesh independence study was performed to determine the accuracy of the discretization. The overall pressure drop due to the inclined plate was selected as the metric for the mesh independence study. Another accuracy test was the

identification of the dimensionless distance y+ between the wall-adjacent nodes and the wall. The maximum value of y+ was found to be four, a value well within the guideline for the accurate use of the software. Also, a convergence criterion of 10^{-6} was also used.

2. 5 Geometry

During this research, three different duct heights were considered: 127, 152, and 178 mm. To identify the relevant plate geometries and the angle of attacks, Figure 44 was prepared. This figure shows the dimensional information and the plate inclinations for 127 mm duct height which is typical of the different heights. For each duct height, three different plate inclinations, 5, 15, and 22.5 degrees were investigated. The Reynolds numbers ranged from 0.1 to 25,000 encompassing the laminar, transition, and turbulent regimes.

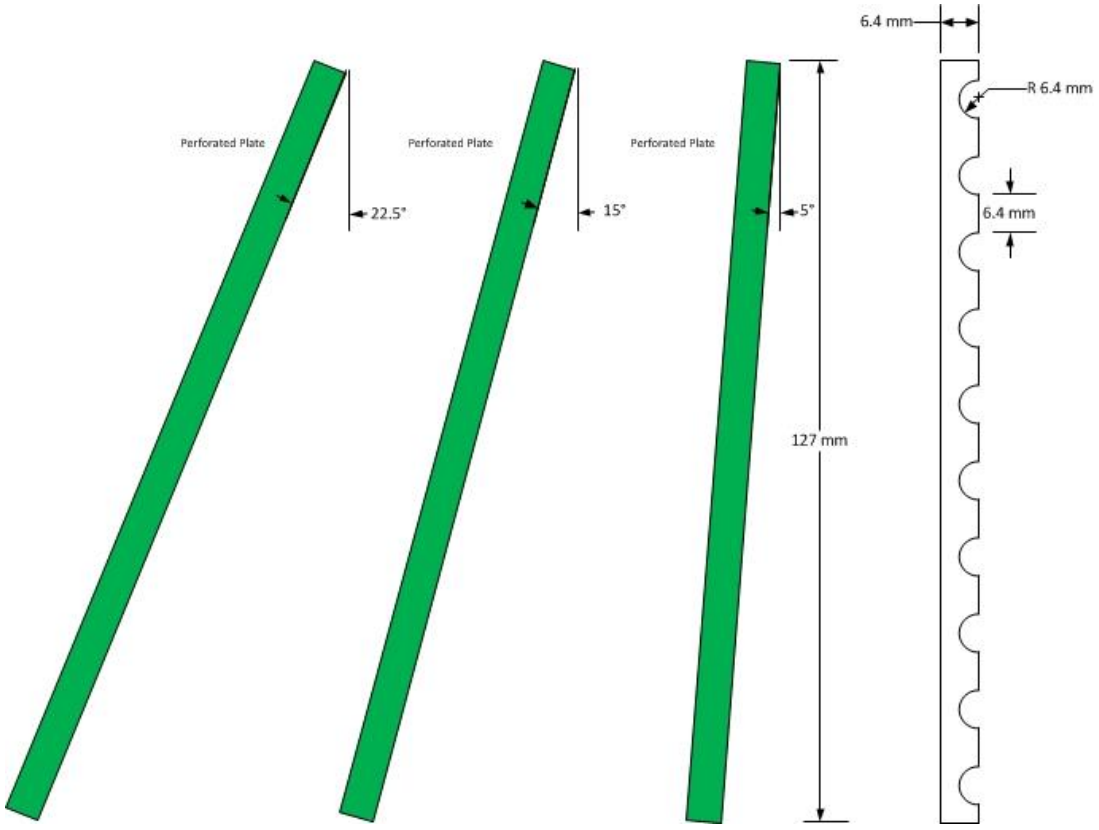

Fig. 22. Typical plate inclinations and plate geometry shown for 127mm duct height.

3. Pressure Drop Results for Laminar and Turbulent Flow

3. 1 Laminar Flow Pressure Drop and Breakdown

The quantification of the pressure drop results requires identification of the prevailing flow regime. The simplest flow regime is laminar friction-dominated flow. For such flows, it is well established that the pressure drop is a linear function of the mean velocity. In terms of the dimensionless representations used here, this relationship reduces to the quantity $(\Delta p/\rho U_o^2)Re_o$ being independent of the Reynolds number. To determine the conditions under which the foregoing quantity is Reynolds number independent, Fig. 23 has been prepared. In the

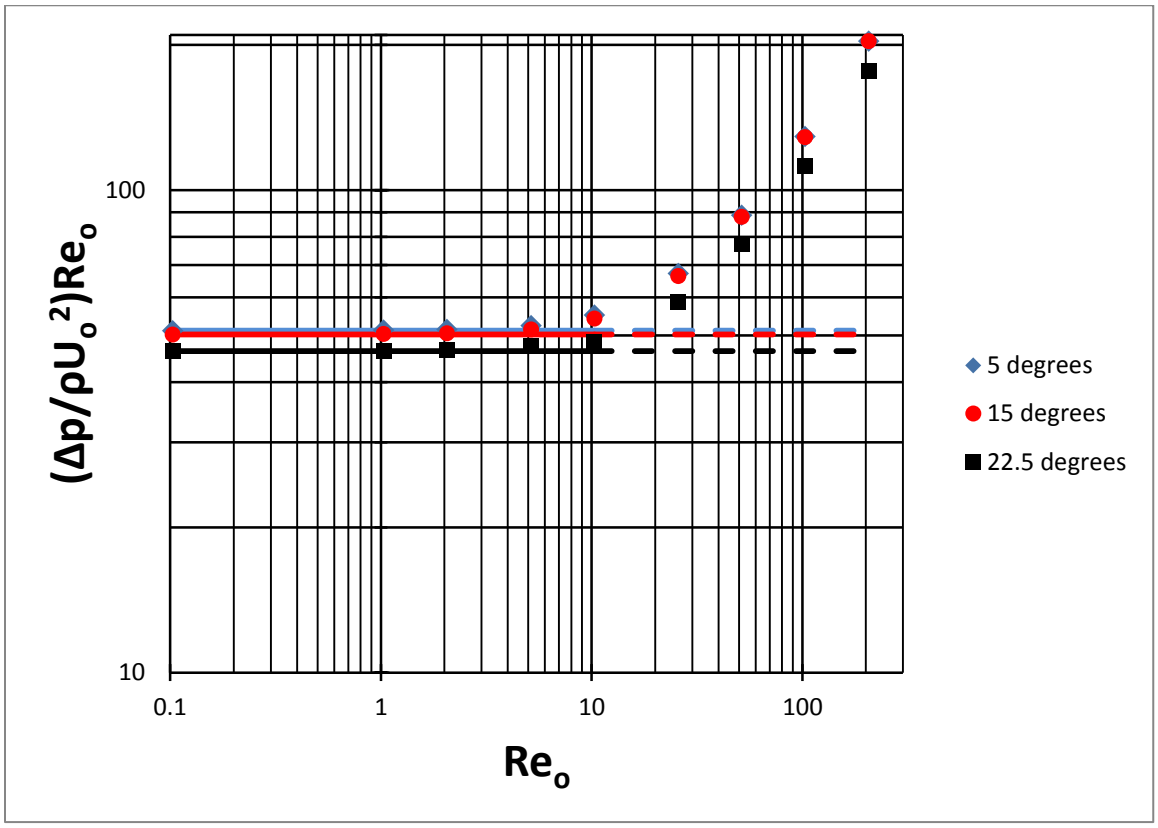

Fig. 23. Dimensionless pressure drop results for a 19.6% porosity perforated plate inclined at angles of 5, 15 and 22.5 degrees. The figure illustrates the breakdown of the laminar friction-dominated flow.

figure, $(\Delta p/\rho U_o^2)Re_o$ is plotted as a function of the Reynolds number for parametric values of the angle of inclination of the plate.

Inspection of the figure shows that the laminar, fiction-dominated regime is terminated at approximately $Re_o = 4$ independent of the inclination angle. Not plotted in Fig. 23 are the results for the zero-degree inclination angle. Those results could not be distinguished from those for the five-degree inclination. Subsequent to laminar breakdown, $(\Delta p/\rho U_o^2)Re_o$ increases monotonically with increasing Reynolds number. This trend indicates that the pressure drop itself sustains a greater than linear dependence on the velocity.

3. 2 Pressure Drop for Turbulent Separated Flow

Turbulent flow in its simplest manifestation displays a pressure drop whose dependence on the velocity is approximately to the power 1.75. On the other hand, when the flow is turbulent and separated, the pressure drop varies with the square of the velocity. Information as to the pressure-drop dependence on the Reynolds number for turbulent flow is conveyed in Fig. 24. In the figure, $(\Delta p/\rho U_o^2)$ is plotted as a function of the Reynolds number for parametric values of the angle of inclination. It can be seen from the figure that for the lower Reynolds numbers, the data have a slight downward trend. This trend indicates that the dependence of the pressure drop on the velocity is less than the square. On the other hand, for the higher Reynolds numbers, the quantity $(\Delta p/\rho U_o^2)$ is independent of the Reynolds number, a definitive indication that the pressure drop varies with the square of the velocity. The onset of this regime is approximately at Re = 10000. It is also seen from the figure that the pressure drop decreases with increasing plate inclination.

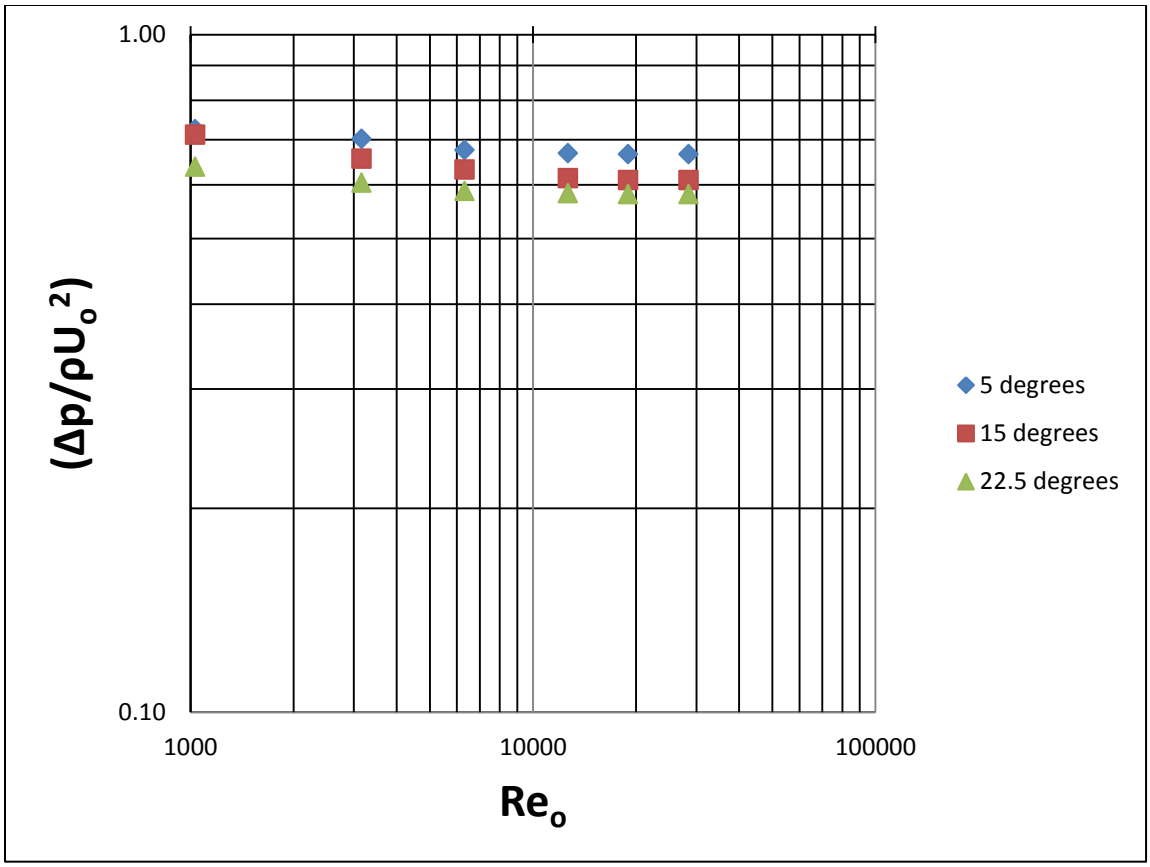

Fig. 24. Turbulent-flow pressure drop results for a 19.6% porosity perforated plate inclined at angles of 5, 15 and 22.5 degrees.

A more focused display of the effect of inclination angle on the pressure drop is conveyed in Fig. 25. The figure was prepared to exhibit the degree to which the pressure drop depends on the height of the wind tunnel in which the perforated plate is situated. The specific information with respect to the height effect is contained in a table that is inset into the figure. Inspection of the table indicates that the wind tunnel height is a second-order effect. The data plotted in the figure are averaged over the three heights. From the plotted data, it may be concluded that the inclination angle is not a major parameter for the magnitude of the pressure drop.

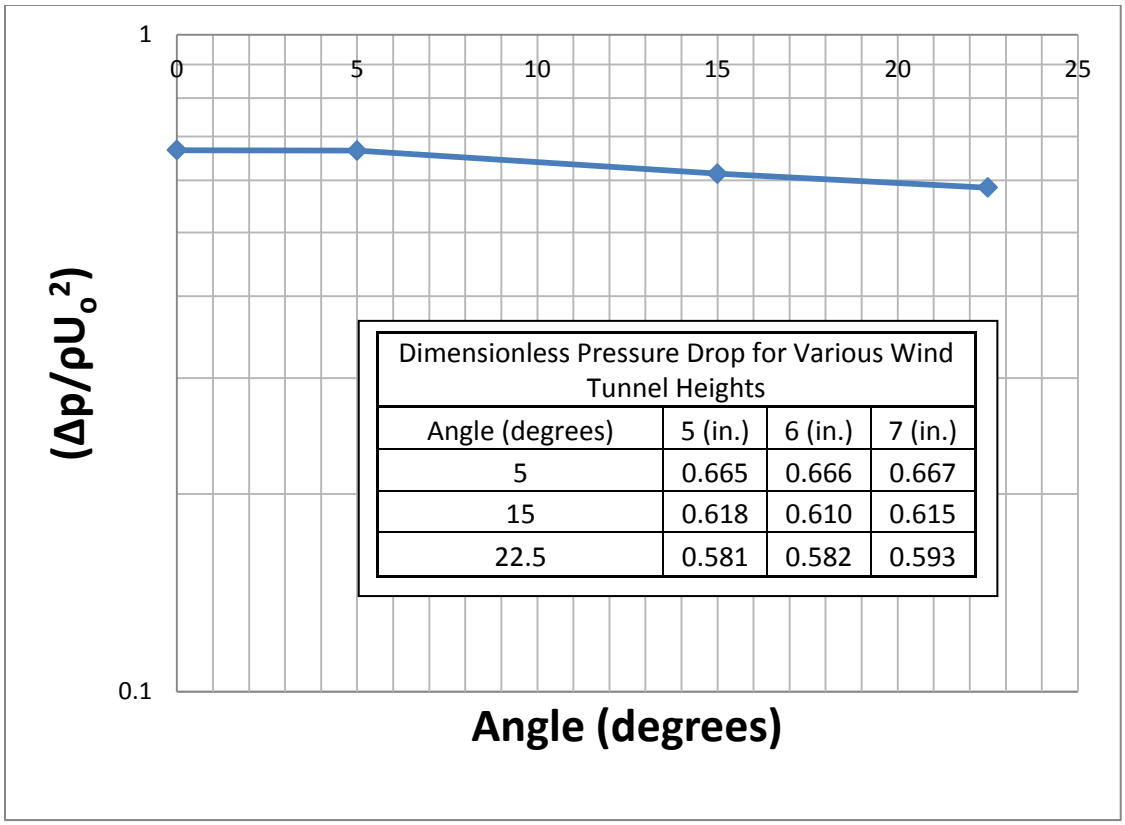

Fig. 25. Universal dimensionless turbulent-separated pressure drop results for a 19.6% porosity perforated plate inclined at angles of 0, 5, 15 and 22.5 degrees.

4. Vector Diagrams Showing Velocity Field Details

The complexity of the fluid flow merits a careful examination of the details of the flow field. In that regard, it was deemed appropriate to use vector diagrams as the most revealing means of conveying this information. The locations selected for the display of flow field details are displayed in Fig. 26. This figure is an

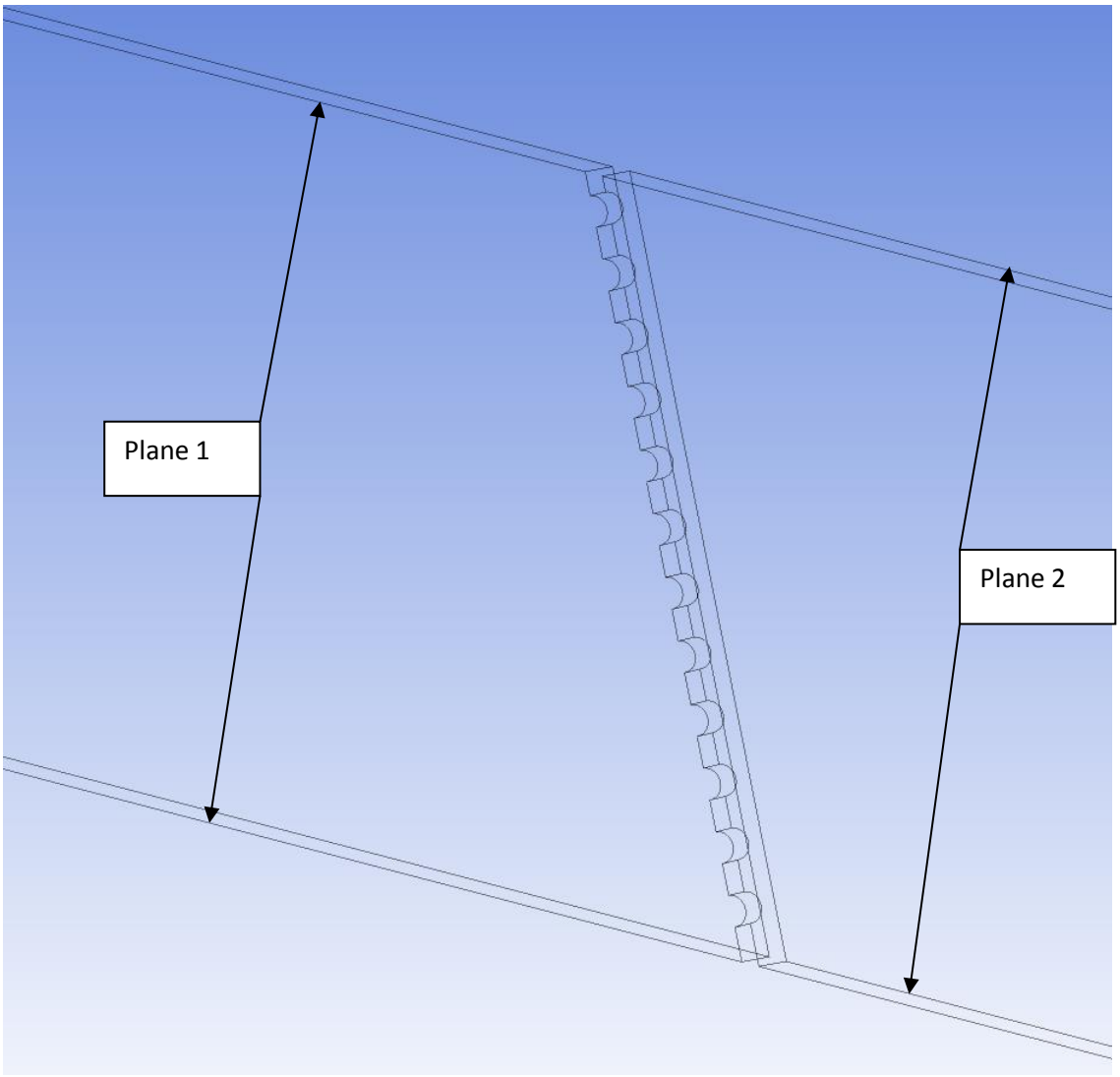

Fig. 26. Symmetry planes for subsequent display of the velocity field. Plane 1 passes through the centers of an array of holes extending from the top to the bottom of the perforated symmetry module within which plate Plane 2 is situated

along the locus of the midpoint between side-by-side holes. Further elucidation is available in Fig. 20.

isometric view revealing the numerical solutions were obtained. For each case defined by the Reynolds number, the plate inclination angle, and the duct height, velocity vector fields in the plane passing through the centers of the holes and in the plane defined by the locus of midpoints are presented. For economy of presentation and without loss of generality, the duct height of six inches has been selected for all the results to be presented.

The starting point of the presentation is the case characterized by a Reynolds number of 12500. Reference to Fig. 24 indicates that this Reynolds number represents a turbulent-separation situation. For this Reynolds number, a total of six flow field vector diagrams are to be presented, respectively for inclination angles of 5, 15 and 22.5 degrees and, for each inclination angle, the flow field in the two planes described in connection with Fig. 27.

Figure 27 corresponds to the 5-degree inclination angle and to the plane that cuts through the holes in the perforated plate. As seen in the figure, the perforated plate appears as a succession of open holes interspersed with blockages. The flow, passing from right to left, seeks the open holes as it encounters the perforated plate. In the lower part of the duct, the approach flow experiences a slight downward cant as it passes through the plate, and this cant continues downstream. In contrast, an upward cant is experienced by the flow that approaches the upper part of the plate, and this flow direction also persists downstream. However, this upflow is blocked by a large eddy situated at the top wall of the duct just downstream of the perforated plate. The presence of the eddy entrains the upflow and transforms it into a downflow.

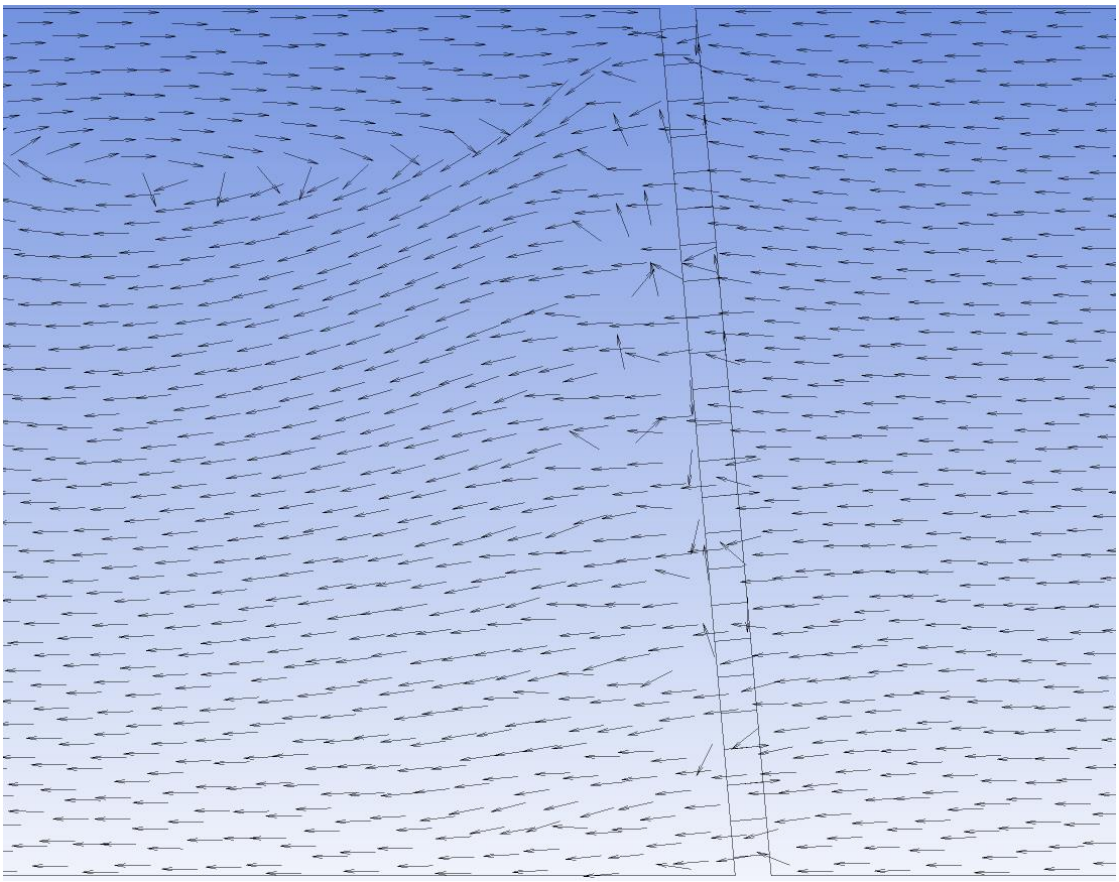

Fig. 27. Velocity field for flow passing through the holes of a 5-degree inclined plate. Re = 12500 (turbulent separated flow).

Figure 28 is the counterpart of Fig. 27, but with the oncoming flow incident on the solid portion of the perforated plate between holes. Observation of this figure reveals significant differences between the displayed flow pattern and that of Fig. 27. In particular, just downstream of the plate, there is a downflow near its upper part which morphs into a strong backflow with descending distance along the plate.

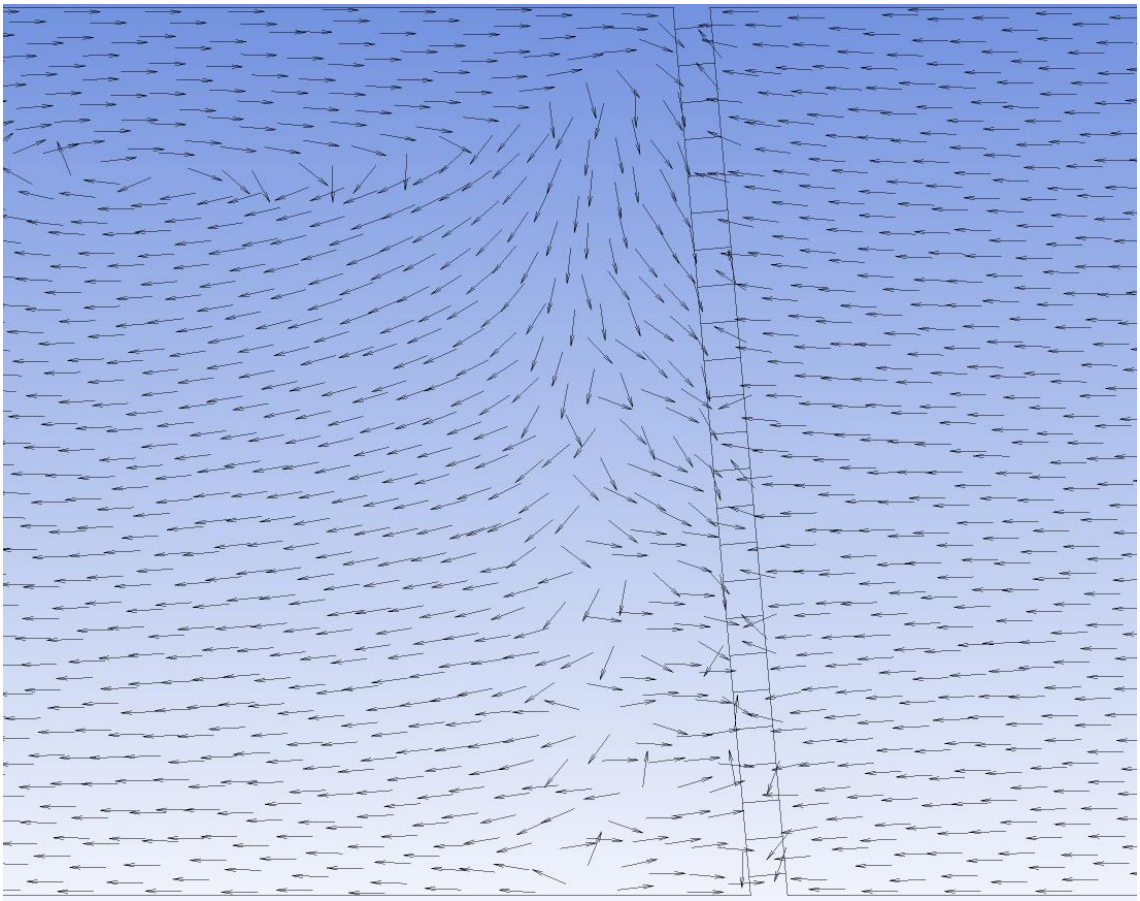

Fig. 28. Velocity field for flow incident on the solid region between holes of a 5-degree inclined plate. Re = 12500 (turbulent separated flow).

Attention is now refocused on the 15-degree plate inclination and on the flow through the open holes of the perforated plate, for which results are shown in Fig. 29. The turbulent separation Reynolds number of 12500 is continued. The first comparison of interest is with Fig. 27, which corresponded to the 5-degree inclination. The most easily observed difference between these figures is the significant growth of the size of the recirculation zone which lies adjacent to the upper wall of the duct, just downstream of the perforated plate. This growth in the recirculation zone creates a major blockage for flow passing through the plate, so that the flow field after the plate has a distinct downward component.

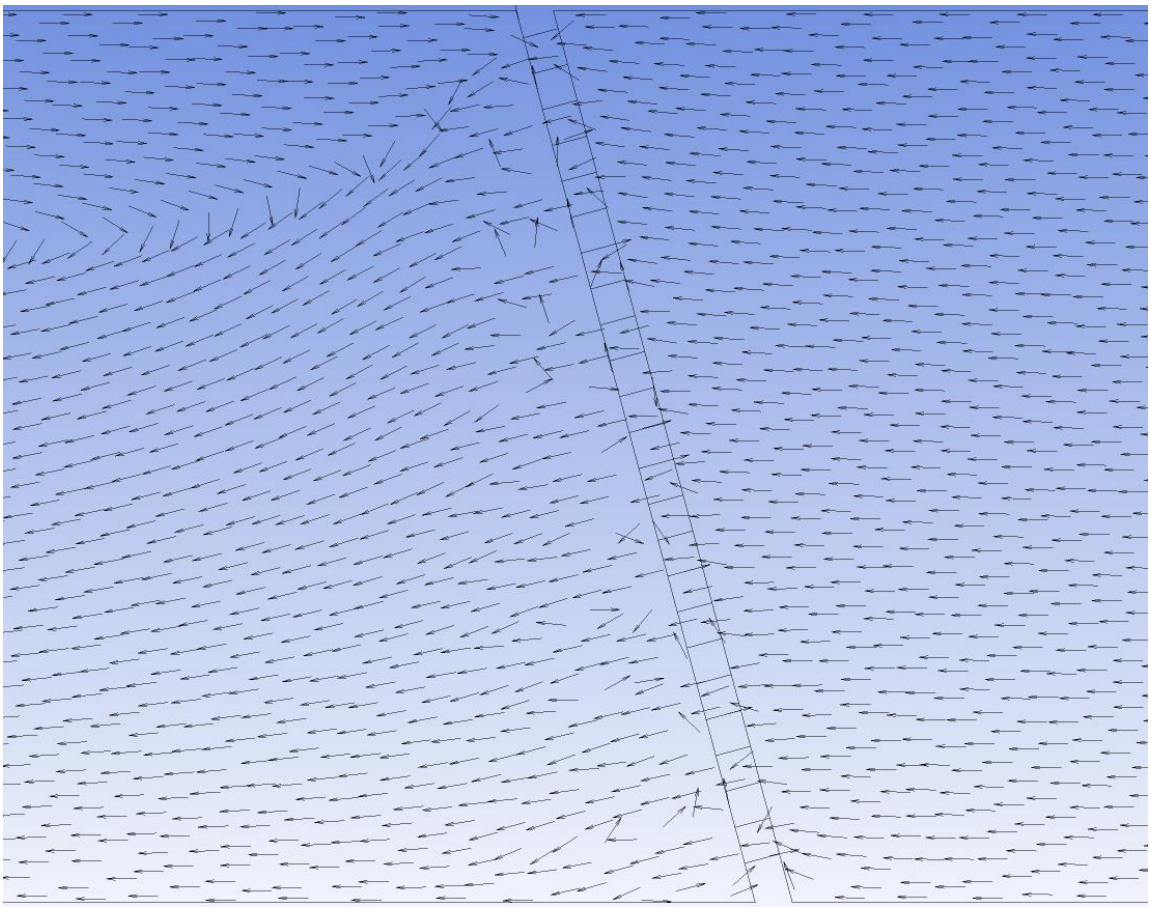

Fig. 29. Velocity field for flow passing through the holes of a 15-degree inclined plate. Re = 12500 (turbulent separated flow).

The next relevant comparison is between the 5- and 15- degree inclined plates for the flow pattern that is incident on the solid portion of the plate between the holes. For this purpose, Figs. 28 and 30 may be consulted. Although there are some minor differences in detail, the general nature of the flow field does not change materially with this change of inclination angle.

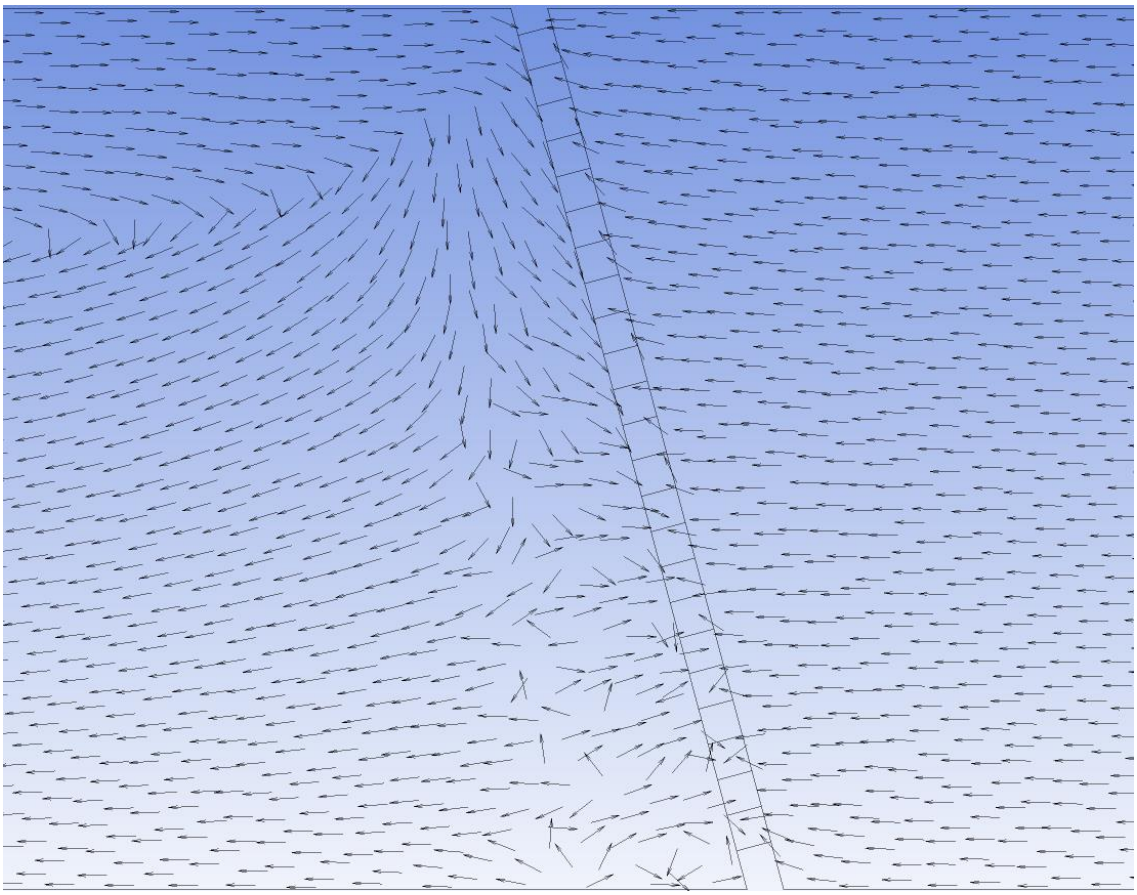

Fig. 30. Velocity field for flow incident on the solid region between holes of a 15-degree inclined plate. Re = 12500 (turbulent separated flow).

The next display of results is for the plate inclined at 22.5 degrees, and attention will first be given to the flow passing through the holes in the plate. Figure 31 has been prepared for this purpose. Inspection of this figure shows only moderate differences from its counterpart for the 15-degree inclination (Fig. 29). The main difference is in the downflow that is induced in the flow approaching the plate in the lower part of the duct. This downflow can be attributed to the stronger downstream-region downflow that is created by enlargement of the recirculation zone.

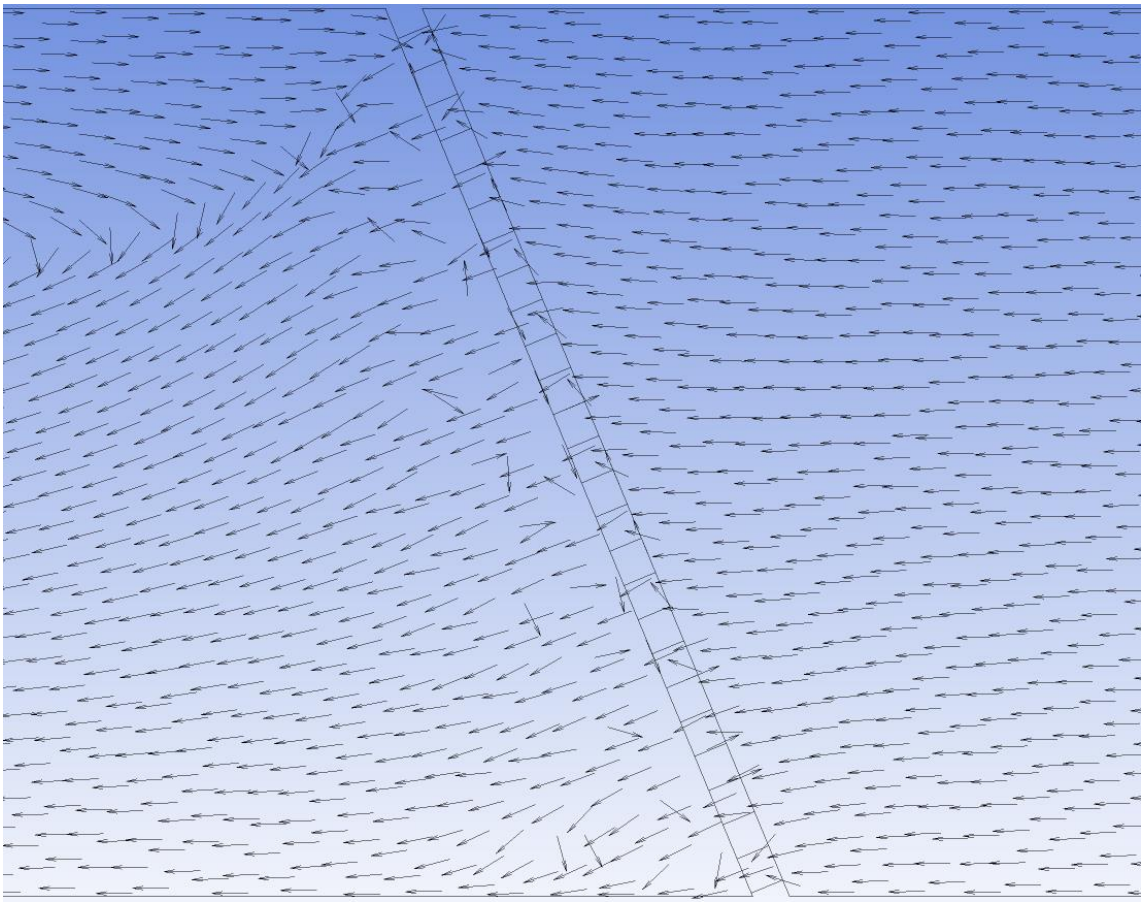

Fig. 31. Velocity field for flow passing through the holes of a 22.5-degree inclined plate. Re = 12500 (turbulent separated flow).

The last figure to be presented in this sequence, Fig. 32, is for the flow incident on the solid portion of the 22.5-degree inclined plate. Compared with its 15-degree counterpart (Fig. 30), the major difference is the presence of a well-organized eddy adjacent to the bottom wall of the duct just downstream of the plate.

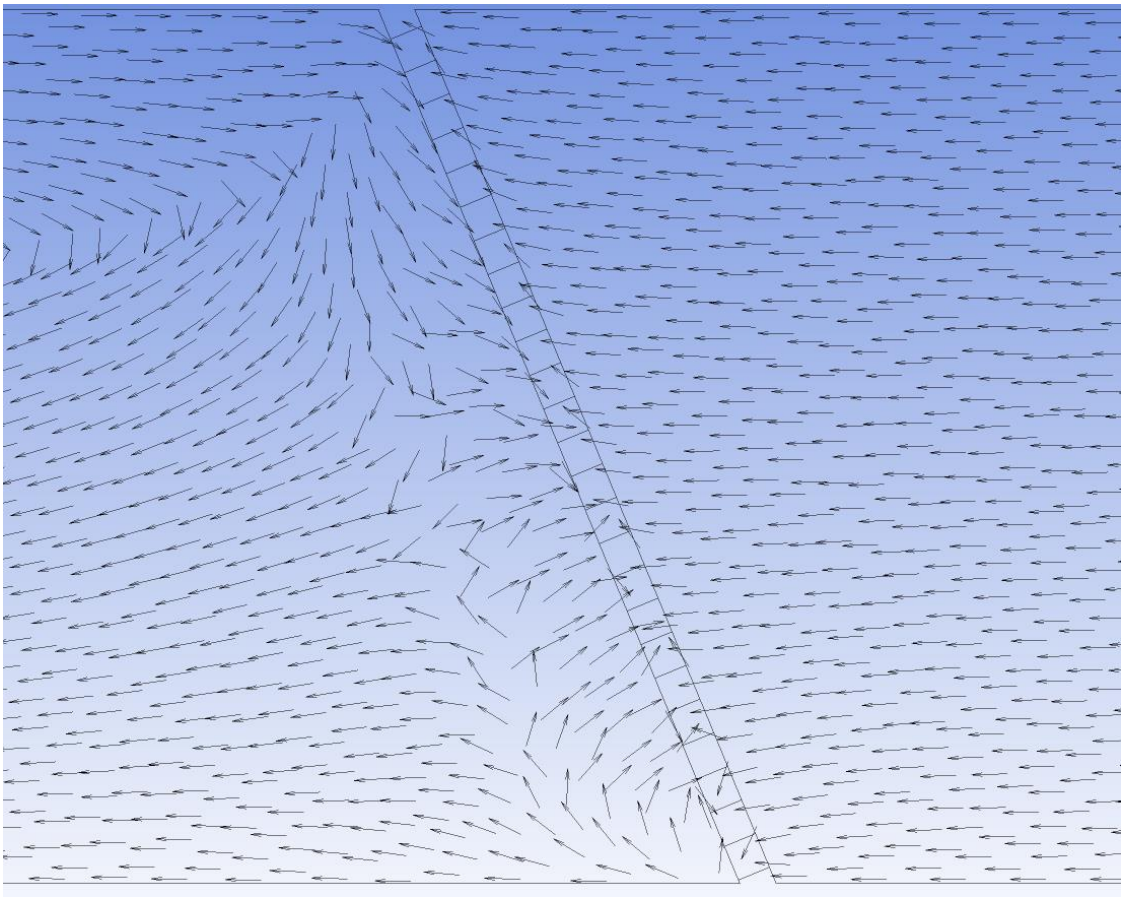

Fig. 32. Velocity field for flow incident on the solid region between holes of a 22.5-degree inclined plate. Re = 12500 (turbulent separated flow).

A retrospective view of the velocity field display reveals the great effect of the size of the recirculation zone on the flow downstream of the plate which, in turn, also affects the flow structure adjacent to the upstream face of the plate. For the flow that passes through the holes in the plate, its downstream flow pattern is given an increasingly stronger downward cant with increasing angle of plate inclination. On the other hand, for the case where the flow impinges on the solid portion of the plate between the holes, a significant backflow is induced.

5. Streamlines Showing Velocity Field Details

An alternative view of the velocity fields can be obtained by the observation of the patterns of the streamlines both upstream and downstream of the perforated plate. The presentation consists of a three-graph cluster for each of three Reynolds numbers, respectively are Re = 2, 400, and 12500. This information is respectively conveyed in Figs. 33-35. Each figure encompasses three graphs labeled (a), (b), and (c), each which corresponds to inclination angles of 5, 15, and 22.5 degrees.

The results for a purely laminar flow corresponding to Re = 2 are conveyed in the graphs that follow. An overview of Parts (a)-(c) reveals the absence of recirculation zones. This outcome can be attributed to the minimal momentum associated with flows of very low Reynolds numbers. These flows are viscous dominated. Another interesting trend is the reversal in the direction of the flow as the fluid crosses the perforated plate. It can be that the flow just upstream of the plate has an upward inclination in the upper part of the duct. On the other hand, the approach flow in the upper part of the duct has a downward inclination. As the flow passes through the perforations, these inclinations are reversed. In particular, in the upper part of the duct, these streamlines have a downward inclination while in the lower part of the duct, the streamline inclination is upward.

5 degrees (a)

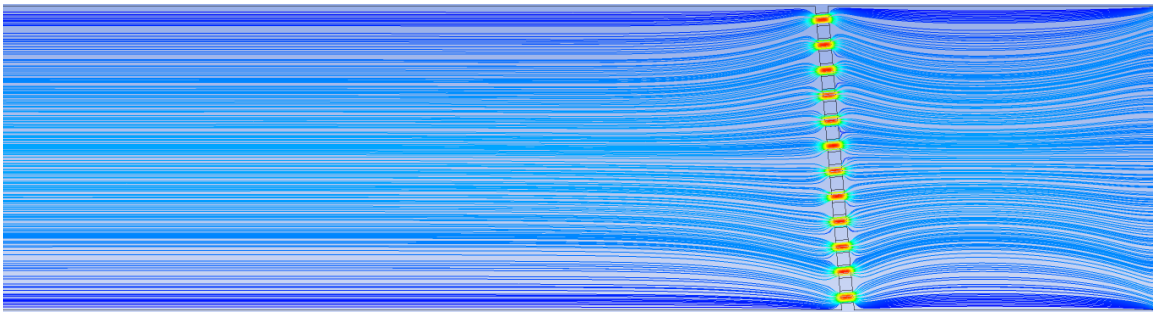

15 degrees (b)

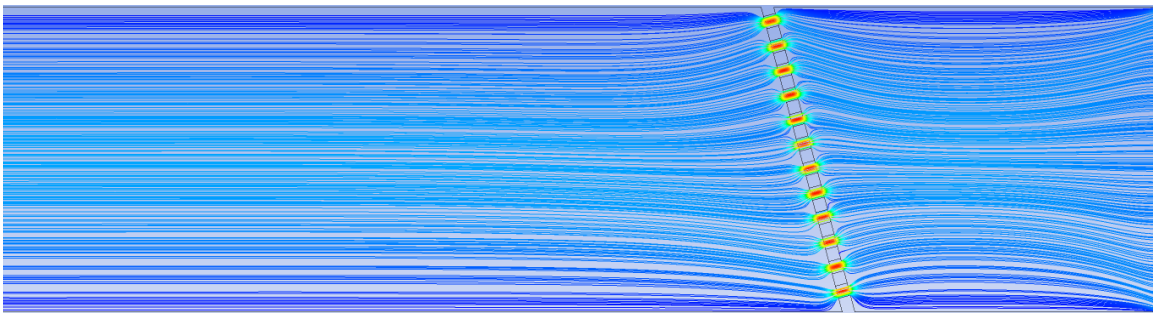

22.5 degrees (c)

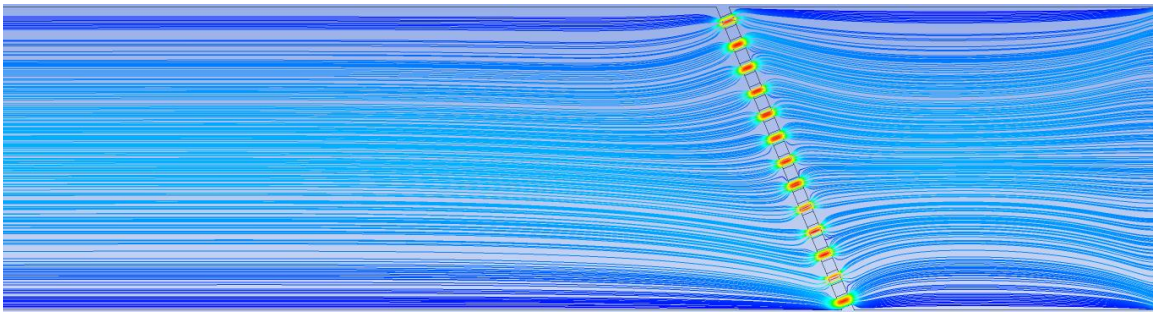

Fig. 33. Streamline patterns for Reynolds number Re = 2: (a) plate inclination = 5, (b) 15, and (c) 22.5 degrees.

Attention is now directed to the results for a Reynolds number of 400. The streamline pattern for the plate inclination of 5 degrees shows that the flow approaching the plate is more or less straight and parallel except for a slight upward inclination near the top of the plate and even more slight downward inclination near the bottom of the plate. The flow passing through the plate appears to have a vector direction that is perpendicular to the plate surface. This five-degree offset is followed by straight and parallel streamlines downstream of the plate.

The 15-degree plate inclination offers an interesting panorama of fluid flow phenomena. First of all, a separated region exists just downstream of the plate in the upper part of the duct. The presence of that region forces a strong downflow of the fluid that passes through the plate. However, that downflow inclination is arrested by another physical occurrence, which is the termination of the separated region. That occurrence requires fluid to fill the space downstream of the separated region which, in turn, creates an upflow. That upflow gives rise to a separated region adjacent to the bottom of the duct. That such occurrences exist in the real world is witnessed by plaque accumulations in branching artery systems. In particular, the recirculation zone observed adjacent to the bottom of the duct would, in a biological application, be a site of a heavy plaque deposit. The streamline pattern for the 22.5-degree plate inclination is virtually identical to that for the 15-degree inclination.

5 degrees (a)

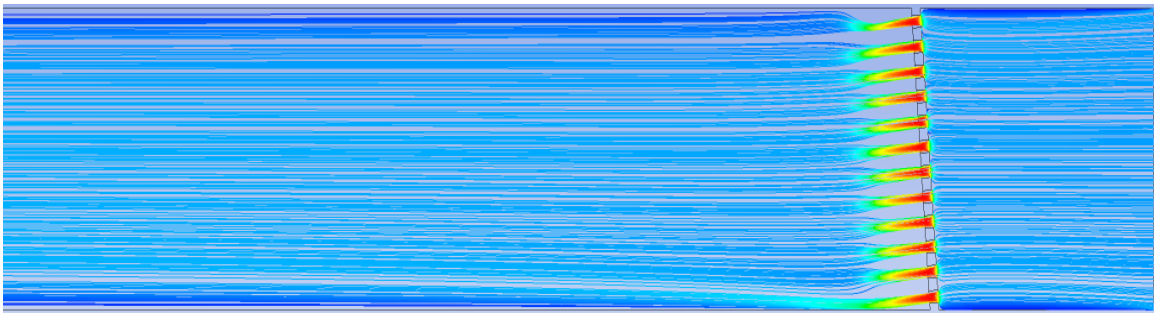

15 degrees (b)

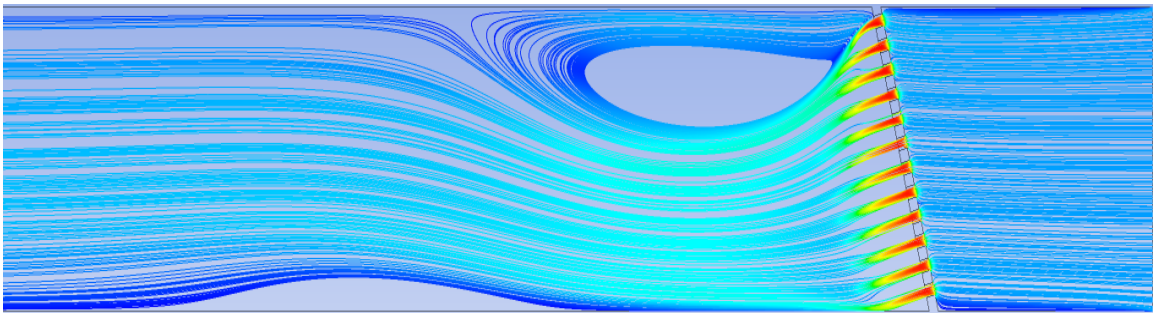

22.5 degrees (c)

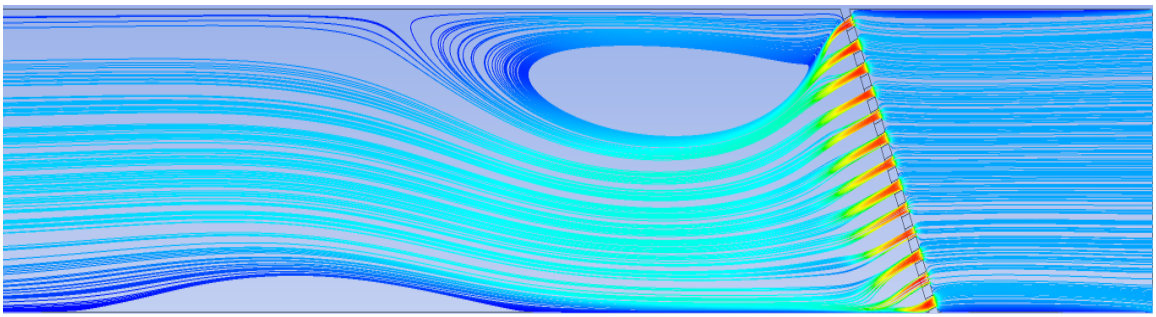

Fig. 34. Streamline patterns for Reynolds number Re = 400: (a) plate inclination = 5, (b) 15, and (c) 22.5 degrees.

The last case to be considered in this series is that for Re = 12500. For the five-degree plate inclination, a small recirculation zone is present for the first time, inasmuch as no circulation was in evidence for Re = 4 and Re = 400 at this inclination. For the 15- and 22.5-degree inclinations, the secondary recirculation zones that were displayed in Figs. 35(b) and (c) for Re = 400 are no longer present at this high Reynolds number. This absence can be attributed to a much more gradual closing of the primary recirculation zone relative to the more rapid closing observed for Re = 400.

5 degrees (a)

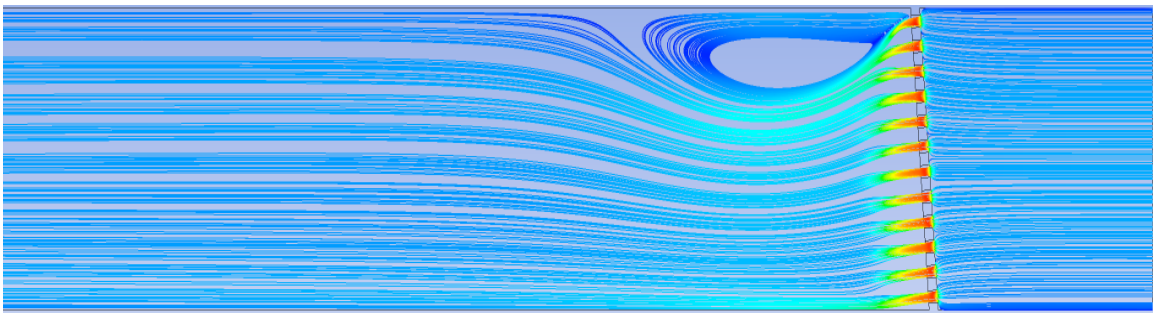

15 degrees (b)

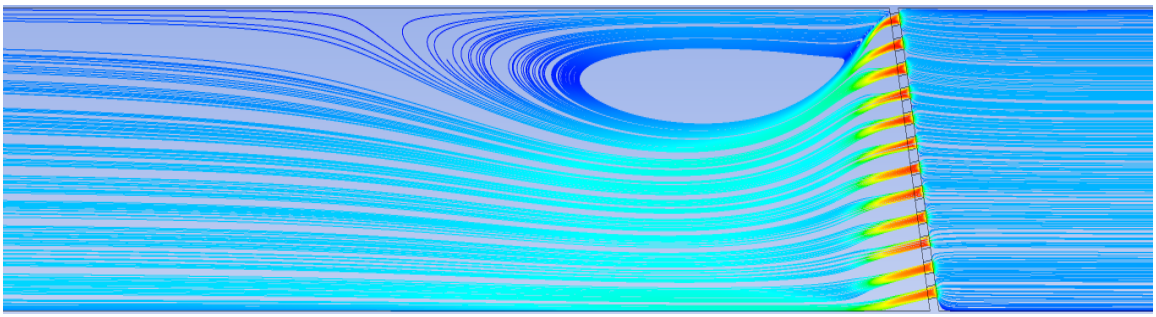

22.5 degrees (c)

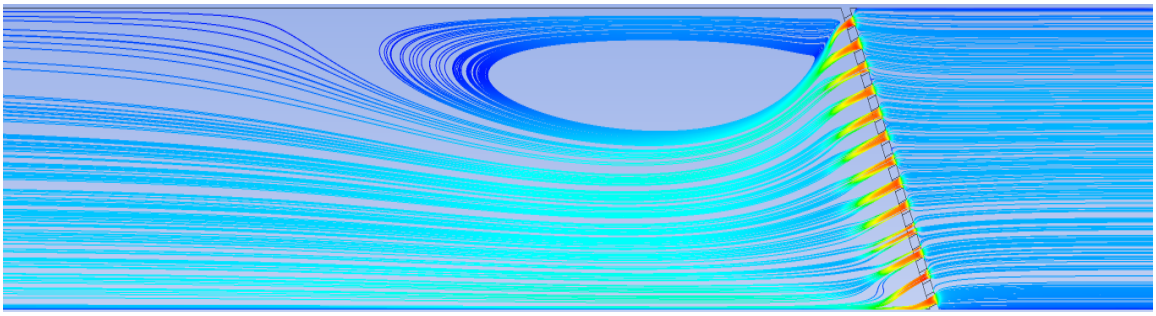

Fig. 35. Streamline patterns for Reynolds number Re = 12500: (a) plate inclination = 5, (b) 15, and (c) 22.5 degrees.

Some of the information that was visually displayed in Figs. 33-35 is quantitatively presented in Fig. 36 where the length of the separation zone is plotted as a function of the angle of inclination of the plate. The information conveyed in the figure is parameterized by the duct height as a curve label. The solid curves correspond to a Reynolds number 12500, and the dashed curve is for a Reynolds number of 400. Note that for the former, separate curves are plotted for duct heights of 5, 6, and 7 inches. On the other hand, for the Reynolds number of 400, information is only available for the duct height of 6 inches. No separation zone occurred for Re = 4.

It can be seen from the figure that the length of the separation zone increases monotonically with increasing angle of inclination. The most rapid increase in the length of the zone occurs at smaller values of inclination. For the 12500

Reynolds number case for which complete information is available, the spread in the length of the recirculation zone is approximately 0.1 meter among the three duct heights.

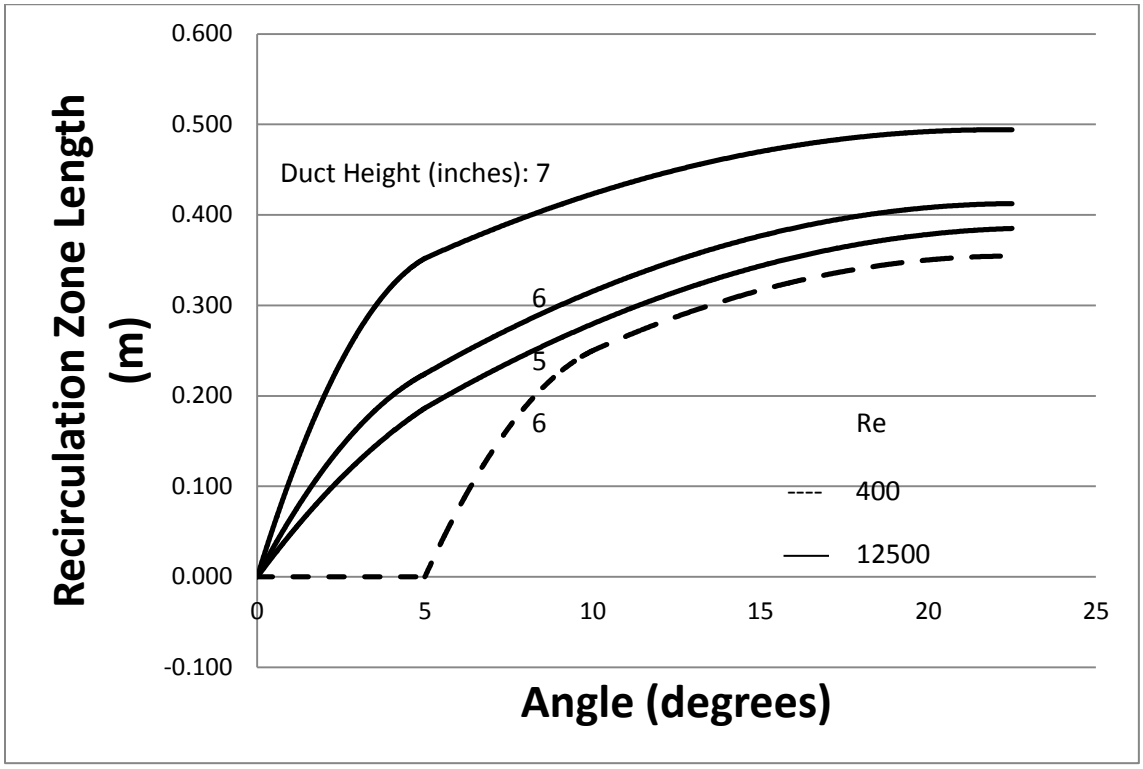

Fig. 36. Length of recirculation zone as a function of plate inclination angle, duct height, and Reynolds number. No recirculation zone appeared for Re = 4. For Re = 400, information is available only for a duct height six inches.

6. Flow Regime Identification

In simple flows such as pipe flows, there are simple rules of thumb which enable the flow regime to be readily inferred. However, for more complex flows, such rules do not exist. Fortunately, there are other means by which flow regimes can be inferred. For example, Fig. 24 indicates a regime where the dimensionless pressure drop is a constant independent of the velocity. From prior knowledge, it is known that turbulent flow separation gives rise to pressure drops that vary with the square of the velocity. In this way, the flow regime is identified.

Another approach is to examine the magnitude of the turbulent viscosity μ_{Turb}. For a flow that is strictly laminar, μ_{Turb} is essentially zero. For situations where μ_{Turb} is more or less on the same order as the viscosity μ, turbulence is present but is not dominating. If the ratio μ_{Turb}/μ is greater than 10, it may be inferred that turbulence is playing a major role.

The foregoing discussion motivates an examination of the μ_{Turb}/μ ratio. This quantity can be extracted from the numerical simulations. A color contour display of this information is made in Figs. 37-39, respectively for Re = 2, 400, and 12500. Each of the figures is subdivided into (a), (b), and (c) parts, with each successive part corresponding to inclination angles of 5, 15, and 22.5 degrees. The results presented in these figures is for a duct height of six inches.

Attention will first be directed to Fig. 37 which corresponds to Re = 2. It is fully expected that the flow will be strictly laminar for such a low Reynolds number. This expectation is fulfilled from the information provided in the figure. Regardless of the inclination angle, the viscosity ratio is on the order of 10^{-18}.

5 degrees (a)

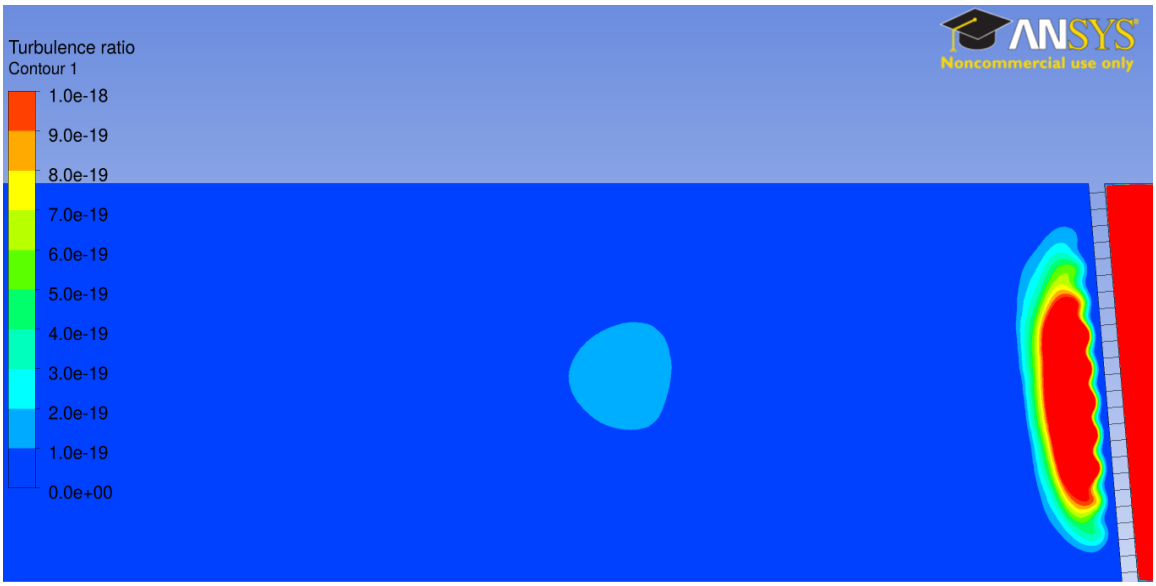

15 degrees (b)

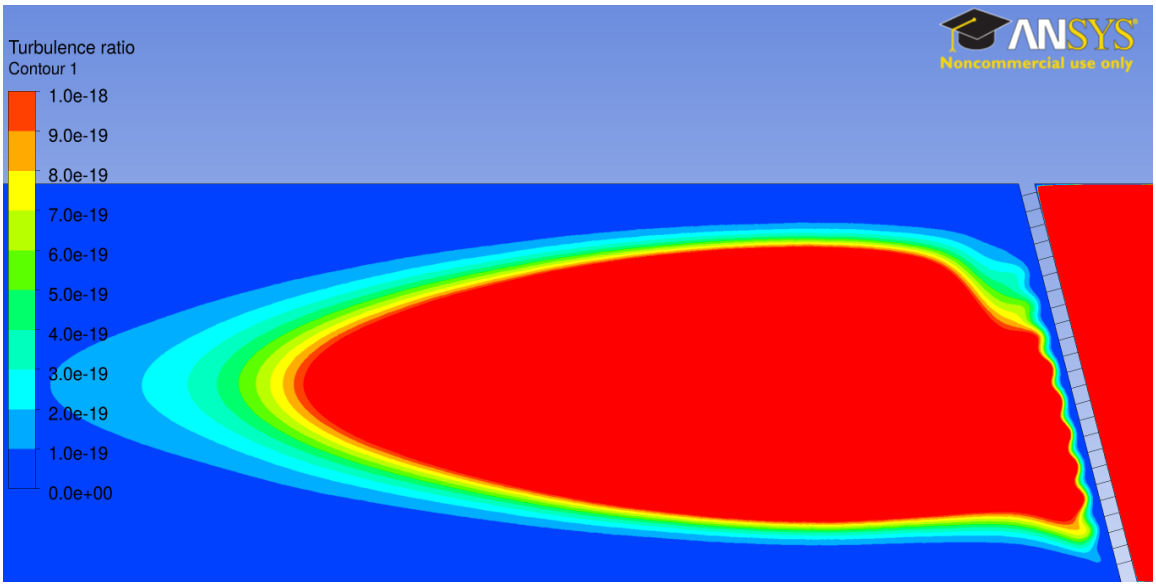

22.5 degrees (c)

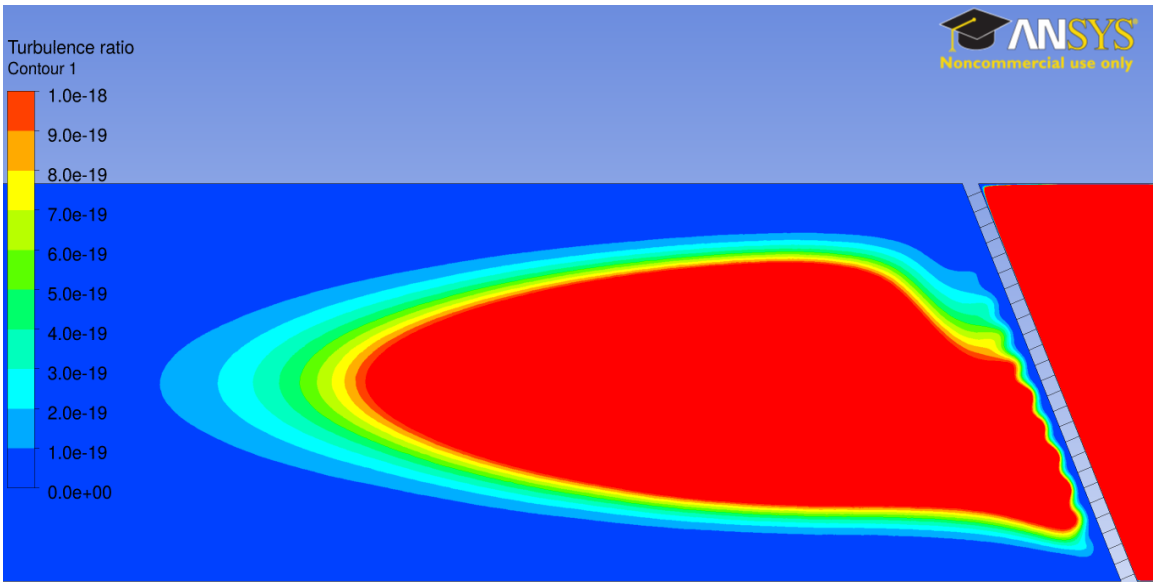

Fig 37. Turbulence ratio μ_{Turb}/μ corresponding to Re = 2 for perforated plates positioned at 5, 15 and 22.5 degrees.

A similar presentation is set forth in Fig. 38 for Re = 400. For this case, there is substantial variation as a function of the inclination angle of the perforated plate. For the lowest angle, 5 degrees, viscosity ratios as large as 11 can be seen in the majority of the flow cross section. Only in the immediate neighborhood of the wall is there a laminar zone. It is interesting to observe that the region of highest turbulence is just downstream of the perforated plate.

Both the magnitude of the viscosity ratio and the deployment of the zone of high turbulence differ drastically for the 15-degree inclination relative to those of the 5-degree inclination. For one thing, the viscosity ratio achieves values as large as 33 for the higher inclination angle. What is even more interesting are the locations of high and low turbulence. The highest turbulence level occurs in the recirculation zone situated adjacent to the top wall of the duct. In contrast, the recirculation zone adjacent to the lower wall experiences considerably weaker turbulence. The magnitude and location characteristics set forth in the

5 degrees (a)

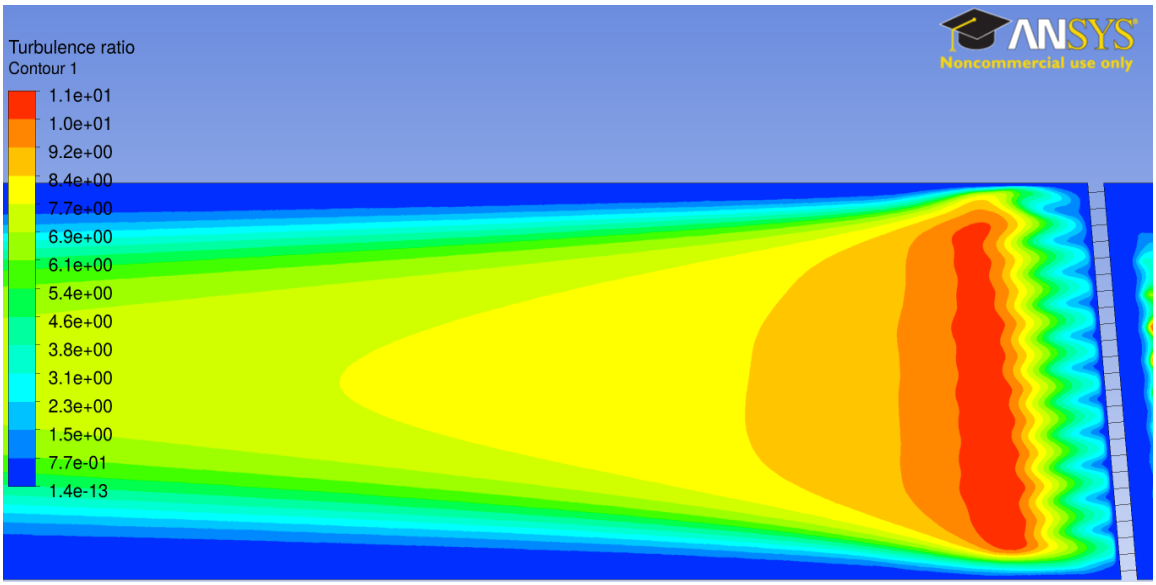

15 degrees (b)

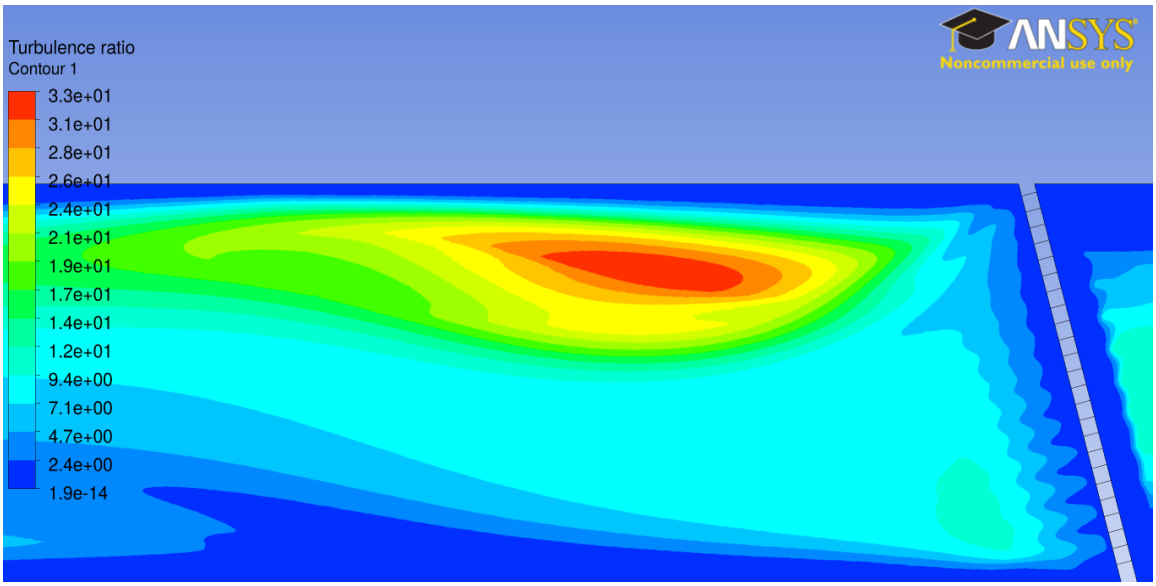

22.5 degrees (c)

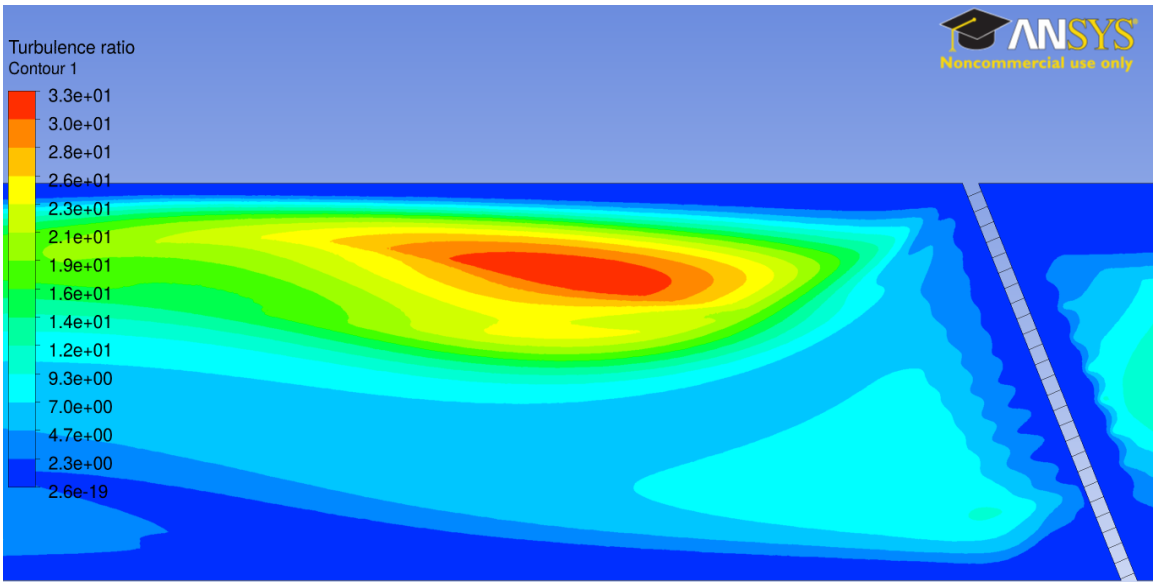

Fig 38. Turbulence ratio μ_{Turb}/μ corresponding to Re = 400 for perforated plates positioned at 5, 15 and 22.5 degrees.

foregoing for the 15- degree inclination are closely repeated for the 22.5-degree case.

The last figure, Fig. 39, in this sequence displays results for a Reynolds number of 12500. The deployment of the zones of highest turbulence are similar for the three angles of inclination. Those zones are concentrated in the recirculation bubble situated adjacent to the upper wall of the duct. The length of the recirculation zone increases with increasing angle, as can be verified from inspection of Fig. 35. By the same token, the region of highest turbulence increases in size with increasing inclination. The actual magnitude of the viscosity ratio takes on very high values for this Reynolds number. At the inclination angle of 5 degrees, the viscosity ratio has a maximum value of 820. With further inclination, that maximum value increases to 1100.

5 degrees (a)

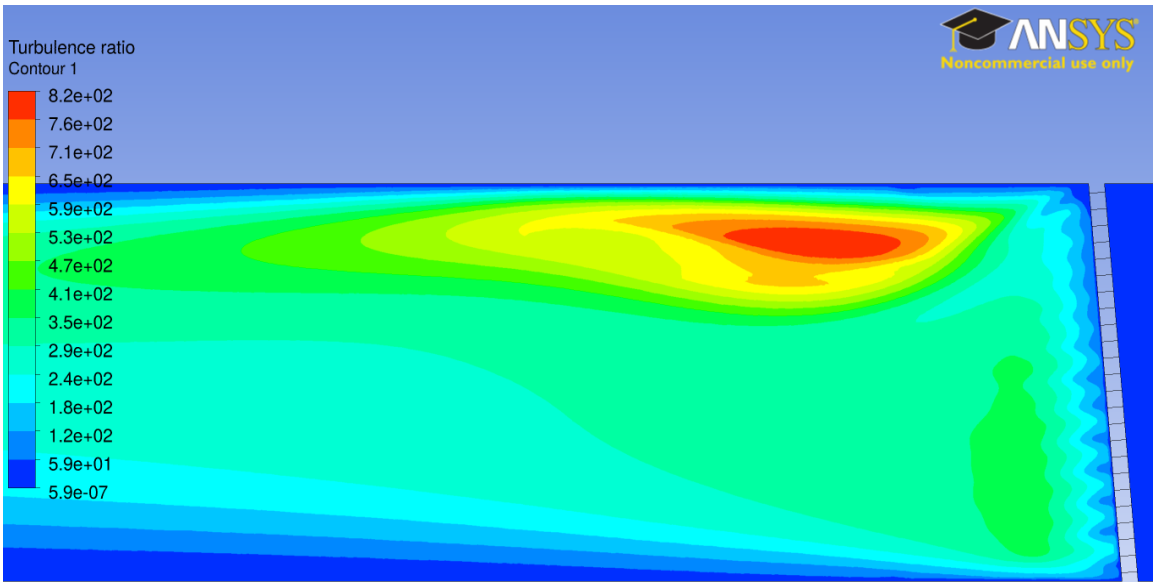

15 degrees (b)

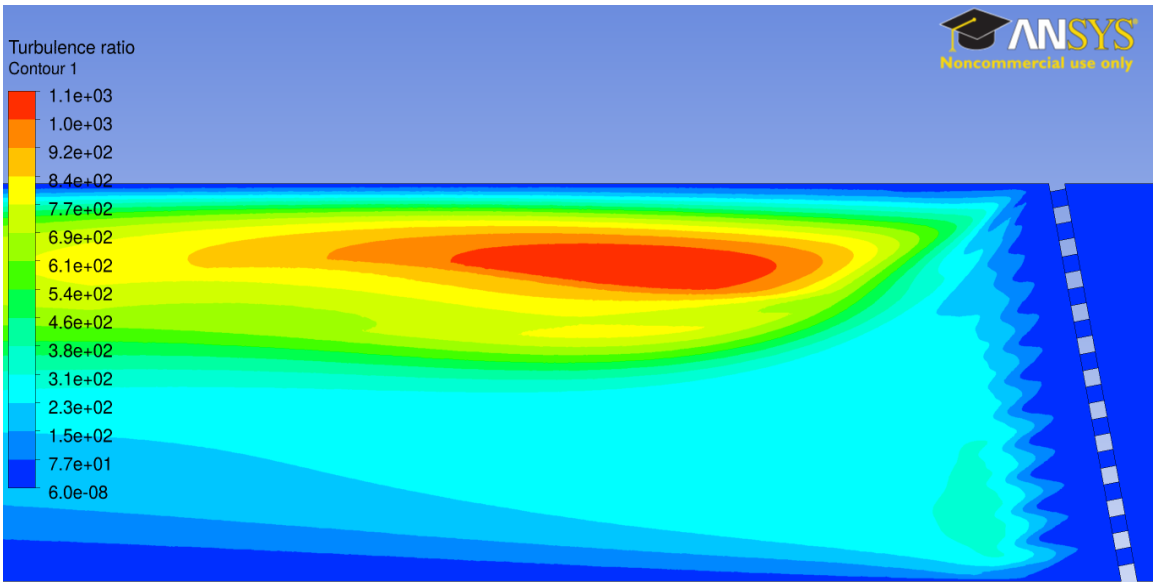

22.5 degrees

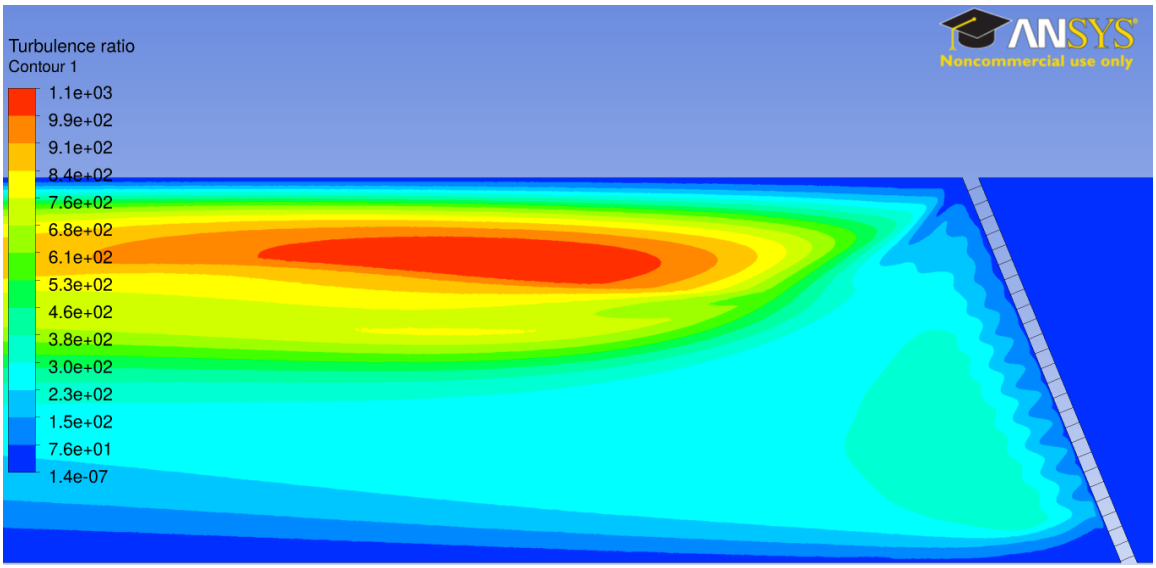

Fig 39. Turbulence ratio μ_{Turb}/μ corresponding to Re = 12500 for perforated plates positioned at 5, 15 and 22.5 degrees.

7. Concluding Remarks

This research has obtained definitive information on numerous aspects of the flow passing through the apertures of perforated plates inclined at angles of 5, 15, and 22.5 degrees. In this situation, the flow is inherently three-dimensional and wall effects are necessarily relevant. In addition to the parametric values of inclination, the other parameters include the Reynolds number whose range extended from 0.1 to approximately 30000. This range encompasses all possible flow regimes. Another parameter is the height of the duct in which the perforated plate is situated.

The presented results include the pressure drop due to the presence of the perforated plate, vector diagrams and streamlines displaying the details of the flow field, and the magnitude and location of zones of turbulence. The latter encompasses zones of no turbulence where the flow is laminar.

For low Reynolds numbers, the linear relation between pressure drop and laminar friction-dominated flow enabled a precise identification of the breakdown of that flow regime, which occurs at Re = 4. With increasing values of the Reynolds number, laminar-turbulent intermittency takes over, and for Re = 10000 the flow is turbulent and separated. Definitive information on pressure drop is presented here for the first time.

The vector diagrams are focused on the case where Re = 12500 and a duct height of six inches with the inclination angle varying from 5, 15, and 22.5. It was clearly seen that the presence of a large recirculation zone situated just downstream of the perforated plate and adjacent to the upper wall of the duct played a dominant role on the flow pattern. In particular, the recirculation zone played the role of a blockage whose presence forced the flow to adopt a deviant path such that a strong downflow was created.

The streamlines provided corroboration of the flow patterns inferred from the vector diagrams and revealed the presence secondary recirculation zones situated in the neighborhood of the lower wall of the duct.

Turbulence levels were identified by a metric which is the ratio of the turbulent viscosity to the molecular viscosity. This metric sharply delineated zones of low, intermediate, and of high turbulence.

CHAPTER 4: GENERALIZED PRESSURE DROP INFORMATION FOR FLOW THROUGH PERFORATED PLATES

1. Introduction

The numerous applications of flow through perforated plates motivate the development of a convenient and generalized means of bringing together available pressure drop information in a form that extends its utility. In this regard, it is relevant to note that perforated-plate fluid flows experience at least two readily identified flow regimes as demonstrated in Chapters 2 and 3 of this thesis. For the laminar, friction-dominated regime, the pressure drop varies linearly with the pore velocity. For high velocity turbulent-separated flows, the pressure drop variation is proportional to the square of the velocity. These observations suggest the possibility that an equation of the form

$$\Delta p = AU + BU^2 \qquad (1)$$

might serve to correlate not only the results for the low- and high-velocity regimes, but might also function as an interpolation formula for flows that are intermediate to those regimes.

It is noteworthy that the form of Eq. (1) is identical to the Darcy-Forchheimer equation that is widely used to characterize flows in porous media. Porous media are, admittedly, more geometrically complex than are perforated plates. In this light, the success of the Darcy-Forchheimer equation for bringing together porous-media pressure drop results motivates an assessment of Eq. (1) as a means for correlating pressure drop information for perforated plates.

To evaluate the suitability of Eq. (1) as means of generalizing the available information for perforated-plate pressure drop as determined in Chapters 2 and 3, the first step is to recast the equation in dimensionless form as

$$(\Delta p/\rho U_o^2)Re_o = \alpha + \beta Re_o \qquad (2)$$

where U_o is the pore velocity, and the Reynolds number is defined as

$$Re_o = \rho U_o D/\mu \qquad (3)$$

In this equation, D is the diameter of the apertures in the perforated plate.

The rationale for using Eq. (2) is that it enables the determination of coefficients α and β as the intercept and slope of a graph in which $(\Delta p/\rho U_o^2)Re_o$ is plotted as a function of Reynolds number.

The information available for evaluating α and β is:

(a) For flow perpendicular to a perforated plate (Chapter 2):

1. t/D = 0.5 and 1.0
2. porosity ≈ 20, 35 and 50%
3. Re_o from 0.001 to 14000

(b) For flow inclined to a perforated plate (Chapter 3):

1. t/D = 1.0
2. porosity ≈ 20%
3. Re_o from 0.01 to 28500
4. Inclination angle = 5, 15 and 22.5^o

2. Generalized Dimensionless Presentation of Results for Perpendicular Impingement

2.1 t/D = 0.5

As described in the foregoing, a graph in which the dimensionless pressure drop $(\Delta p/\rho U_o^2)Re_o$ is plotted as a function of Re_o is an efficient means of determining the critical constants α and β in Eq. (2). The successful determination of these constants depends upon whether the resulting graph displays a straight line. If the outcome is a straight line, β is the slope of the line and α is the intercept of the line with the vertical axis.

For the plate thickness parameter t/D = 0.5, Figs. 1 through 3 present information for the square array of holes and for porosities of 20, 35, and 50%. Fig. 40 pertains to the least porous

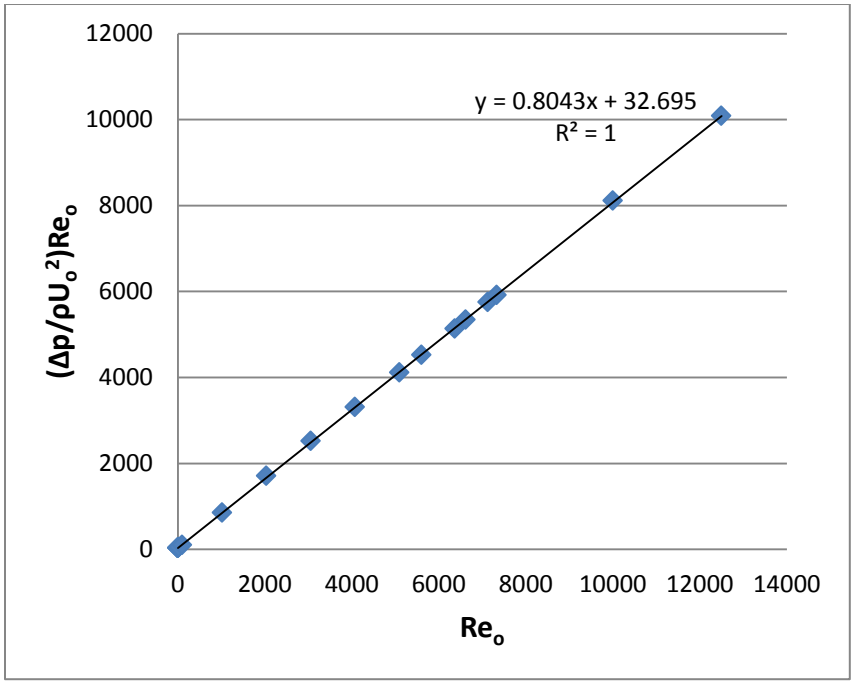

Fig. 40. Generalized pressure drop representation: Square array and ε = 20%.

porous case of 20%. From an inspection of the figure, it is seen that all the data fall perfectly on a straight line. The slope of the line is 0.804 while the intercept is 32.7.

The same mode of presentation for the 35% porosity case, displayed in Fig. 41, yields an intercept of 33.4, which is virtually identical to the corresponding result for 20% porosity. On the other hand, the slope of the Fig. 41 curve, 0.585, differs appreciably from that of 20% case, signaling substantial sensitivity to the value of the porosity. These comparisons indicate trends that will persist throughout the presentation of the results for perpendicular impingement, that is, an intercept which is insensitive to porosity, and a slope which is sensitive to the value of porosity.

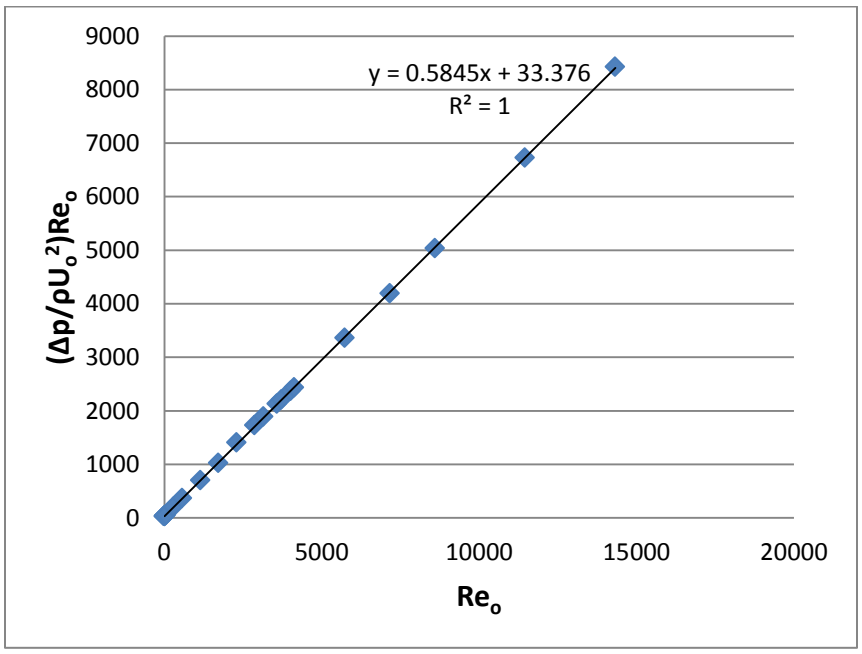

Fig. 41. Generalized pressure drop representation: Square array and ε = 35%.

These characteristics are reinforced in Fig. 42. Here, the intercept is 30.9, and the slope is 0.382.

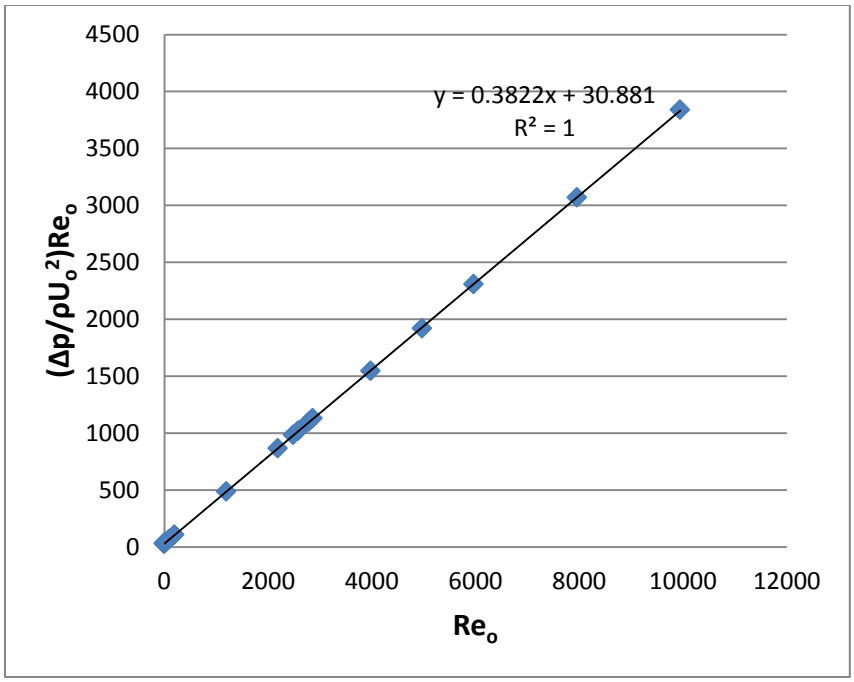

Fig. 42. Generalized pressure drop representation: Square array and ε = 50%.

Figs. 43-45 are the counterparts of Figs. 40-42, but pertain to the staggered array. From these figures, the intercepts can be read as 40.0, 39.4, and 38.2.

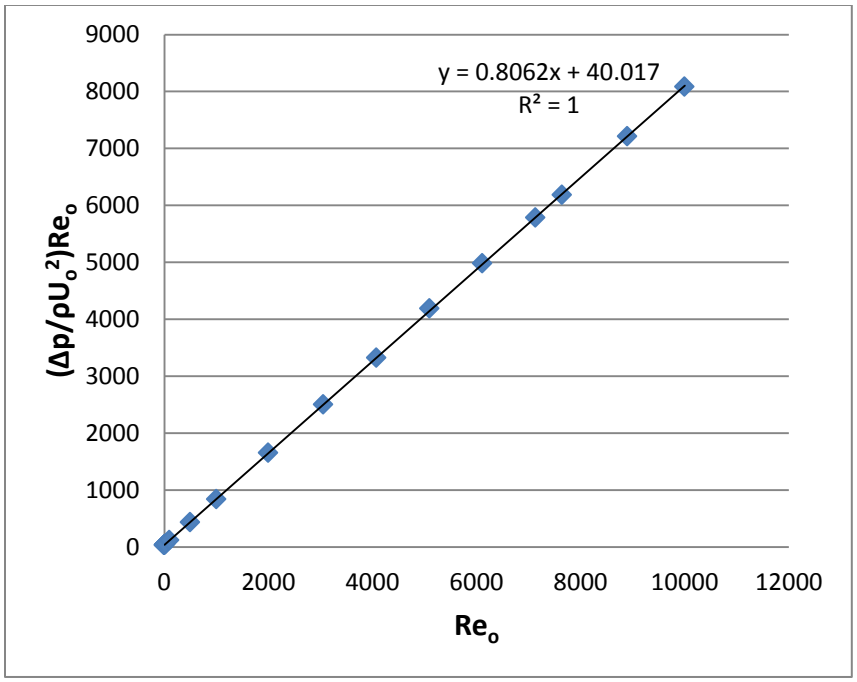

Fig. 43. Generalized pressure drop representation: Staggered array and ε =20%.

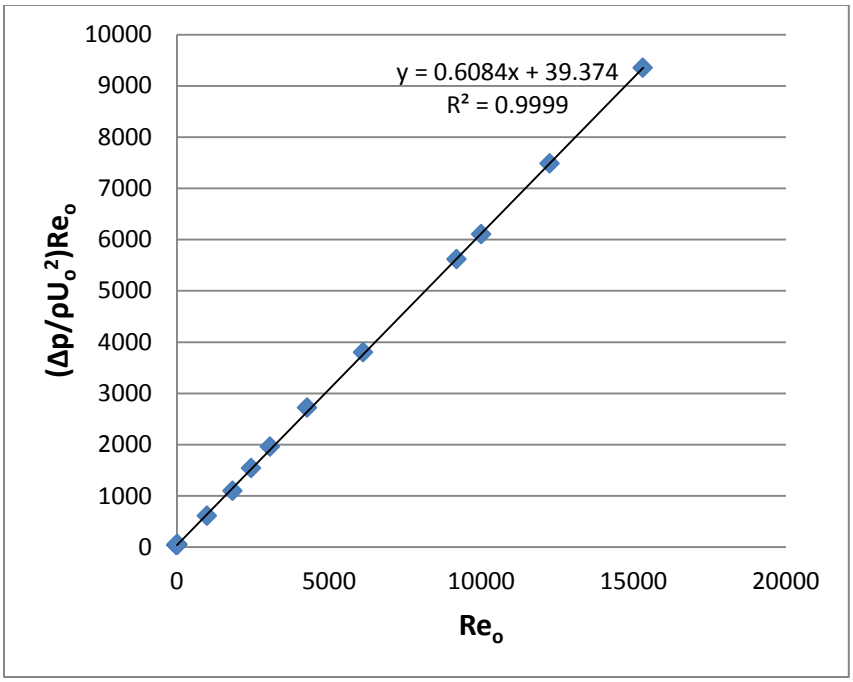

Fig. 44. Generalized pressure drop representation: Staggered array and ε =35%.

These are to be compared with the values of 32.7, 33.4, and 30.9. For both cases, the respective intercepts are insensitive to the permeability. However, the nature of the array, square versus staggered, is a significant parameter.

Further inspection of Figs. 43-45 indicates slopes of 0.806, 0.608, and 0.372. For the square array, the corresponding values are 0.804, 0.585, and 0.382. These results indicate sensitivity to the porosity, but are insensitive to whether the array pattern is square or staggered. The just-displayed reversal of sensitivity and insensitivity to the geometry of the array and to the porosity is noteworthy.

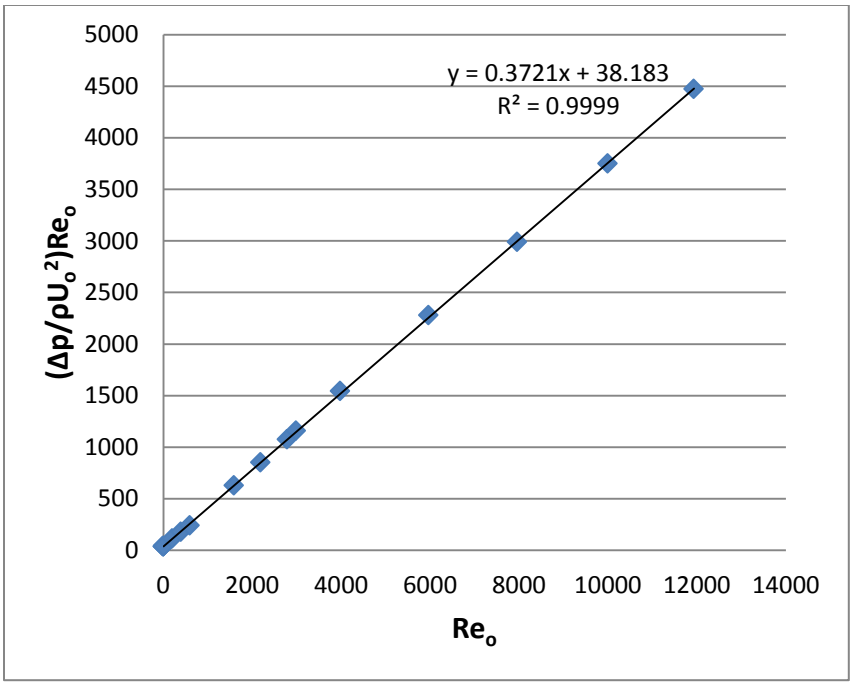

Fig. 45. Generalized pressure drop representation: Staggered array and ε = 50%.

A summary of the findings that were discussed in the preceding paragraphs is exhibited in Table 4.

Table 4: Critical parameters for t/D = 0.5 for normal impingement

Porosity	**Array**	**α**	**β**
20	Square	32.7	0.804
20	Staggered	40	0.806
35	Square	33.4	0.585
35	Staggered	39	0.608
50	Square	30.9	0.382
50	Staggered	38.2	0.372

2.2 t/D = 1.0

Focus is now directed to the thicker plate for which dimensionless pressure drop results are presented in Figs. 46-51. The first three of these figures correspond to the square pitch layout while the second three are for the staggered pitch. It is appropriate to analyze these results in a manner that is similar to that which has been used in the foregoing to assess the results for the t/D = 0.5 plate. For convenience, the results of Figs. 46-51 are brought together in Table 5. It can

Table 5: Critical parameters for t/D = 1.0 for normal impingement

Porosity	Array	α	β
20	Square	51.1	0.660
20	Staggered	61.4	0.628
35	Square	48.9	0.474
35	Staggered	61.2	0.483
50	Square	48.0	0.317
50	Staggered	60.1	0.305

be seen from the table that the slope β is relatively insensitive to whether the array layout is square or staggered. On the other hand, the intercept α displays mild sensitivity, on the order of 20%, to the specifics of the layout. With respect to porosity, there is very little sensitivity (2-4% square array and about 1.5% for the staggered array) to the variation of porosity over the investigated range of 20 to 50% for a given array layout.

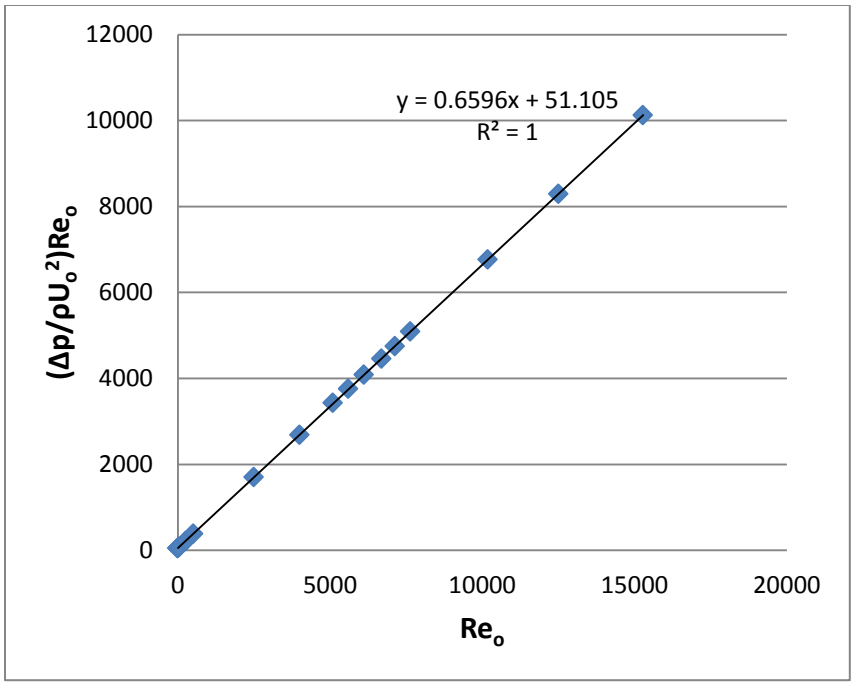

Fig. 46. Generalized pressure drop representation: Square array and ε = 20%.

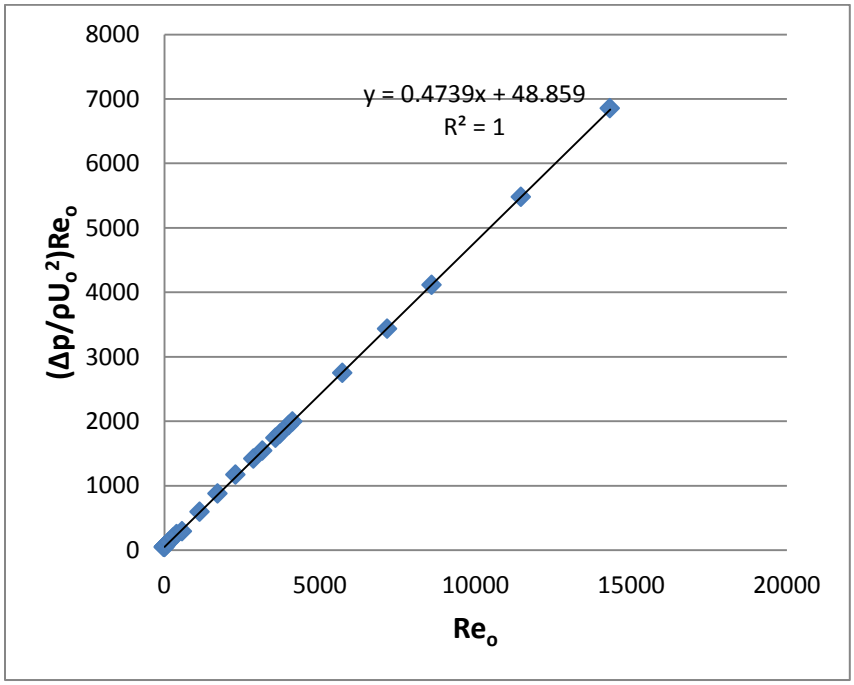

Fig. 47. Generalized pressure drop representation: Square array and ε = 35%.

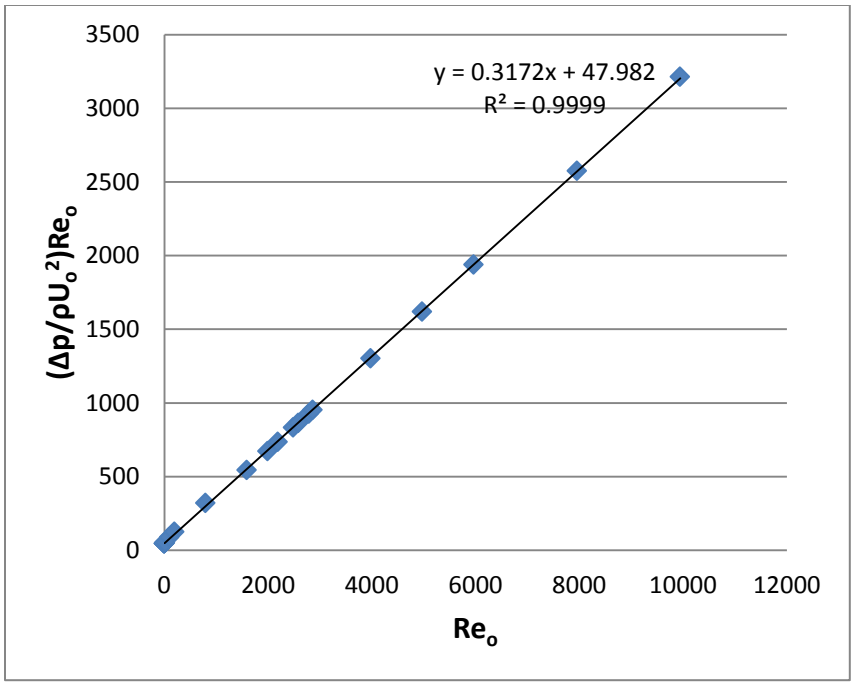

Fig. 48. Generalized pressure drop representation: Square array and ε = 50%.

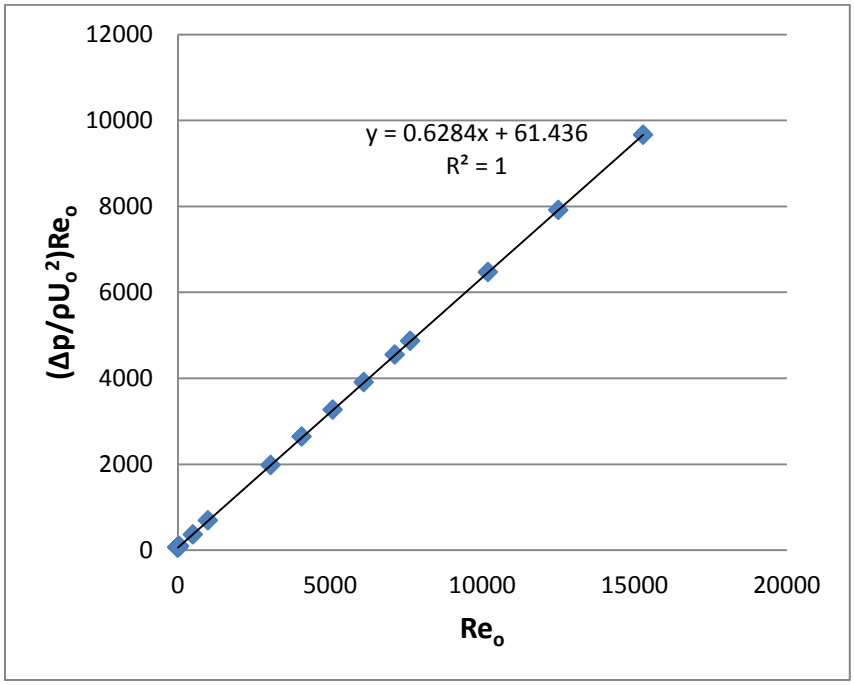

Fig. 49. Generalized pressure drop representation: Staggered array and ε = 20%.

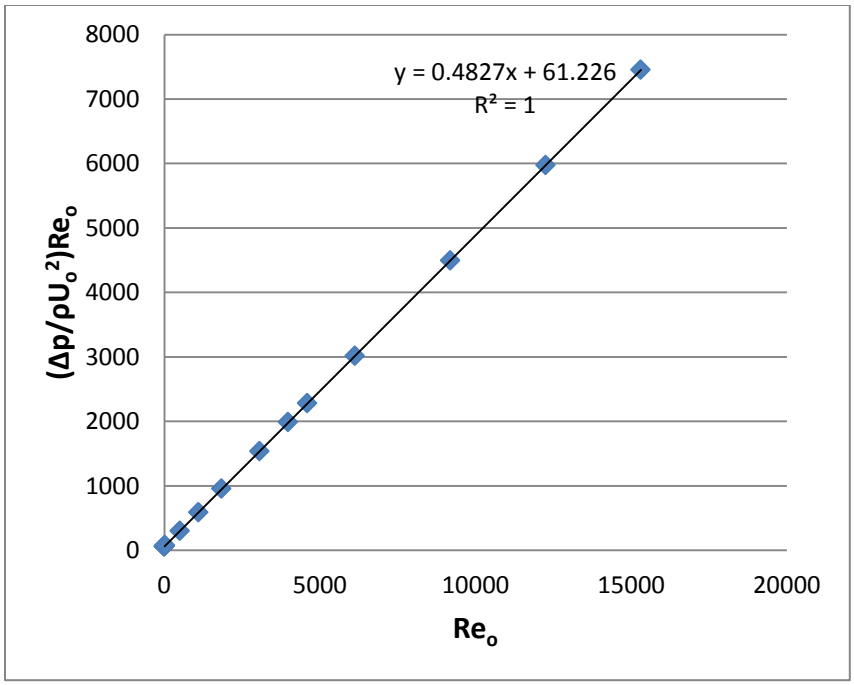

Fig. 50. Generalized pressure drop representation: Staggered array and ε = 35%.

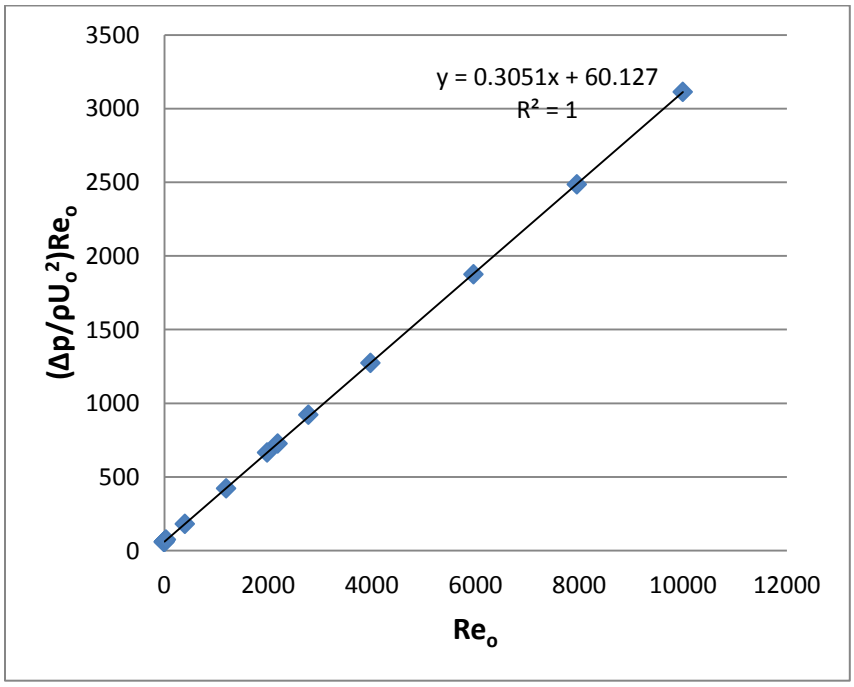

Fig. 51. Generalized pressure drop representation: Staggered array and ε = 50%.

3. Dimensionless Presentation of Results for Inclined Impingement

Attention will now be focused on the pressure drop results for non-normal impingement on perforated plates. The complexity of these flows demanded a much lengthier numerical treatment than was necessary for the case of perpendicular impingement. This greater expenditure of resources was compensated for by limiting the investigation to a single aperture layout (square array) and to a single porosity (20%). The results that were obtained for inclined impingement extended over the Reynolds number range of approximately zero to 28500. This range is considerable greater than the zero to 14000 span of Reynolds numbers that were investigated for the case of perpendicular impingement. This difference in the Reynolds number range was motivated by information relevant to practical applications.

The dimensionless pressure drop results for inclined impingement are conveyed in Figs. 52-54, respectively for inclination angles of 5, 15, and 22.5 degrees. Inspection of these figures reveals a remarkable adherence of the data to a straight line representation as witnessed by the $R^2 = 1$ statistic for all three cases. The key parameters α and β from this presentation are listed in Table 6. For purposes of comparison, Table 6 also contains the appropriate results for normal impingement.

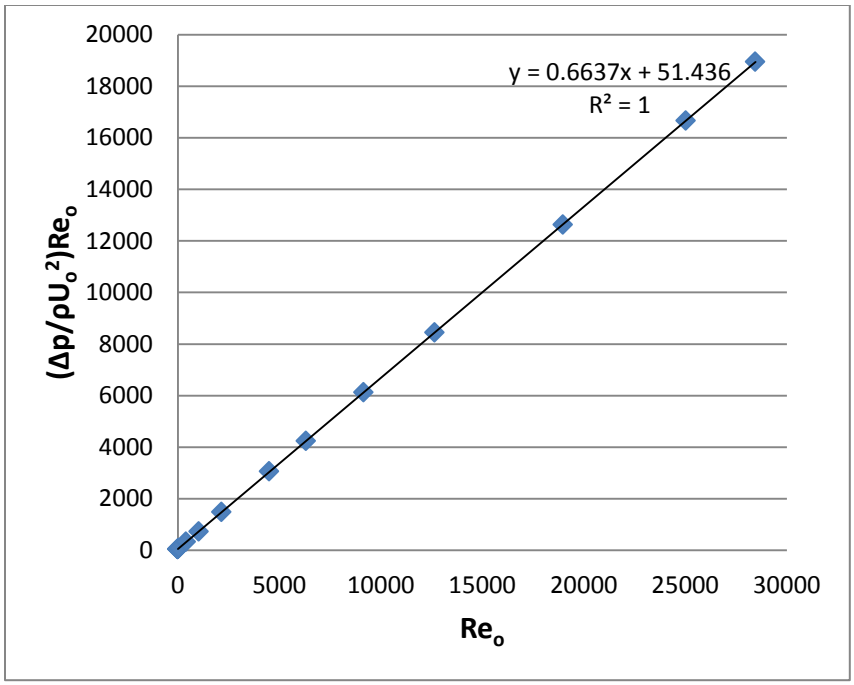

Fig. 52. Generalized pressure drop representation, inclination angle of 5 degrees and porosity of 20%.

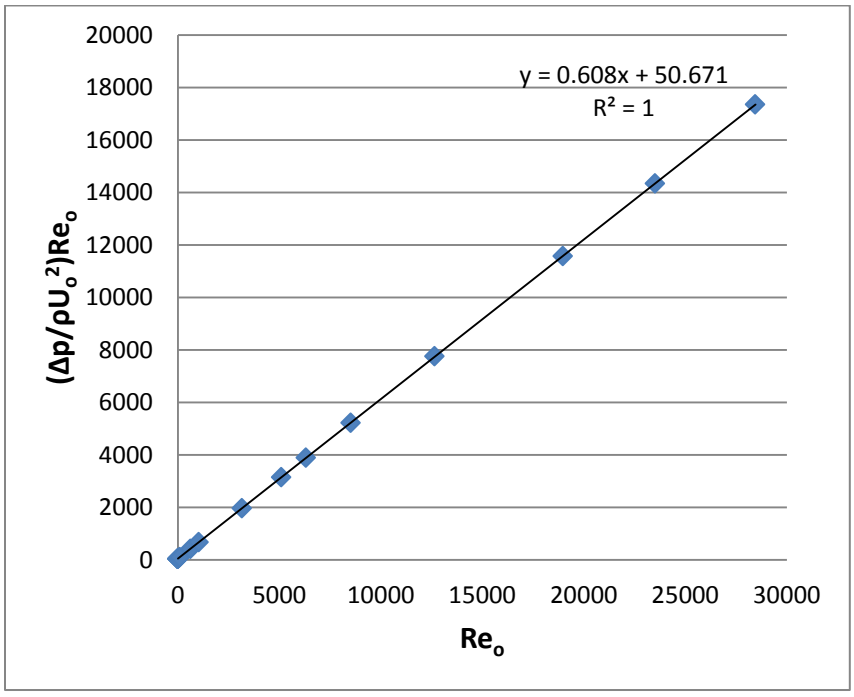

Fig. 53. Generalized pressure drop representation, inclination angle of 15 degrees and porosity of 20%.

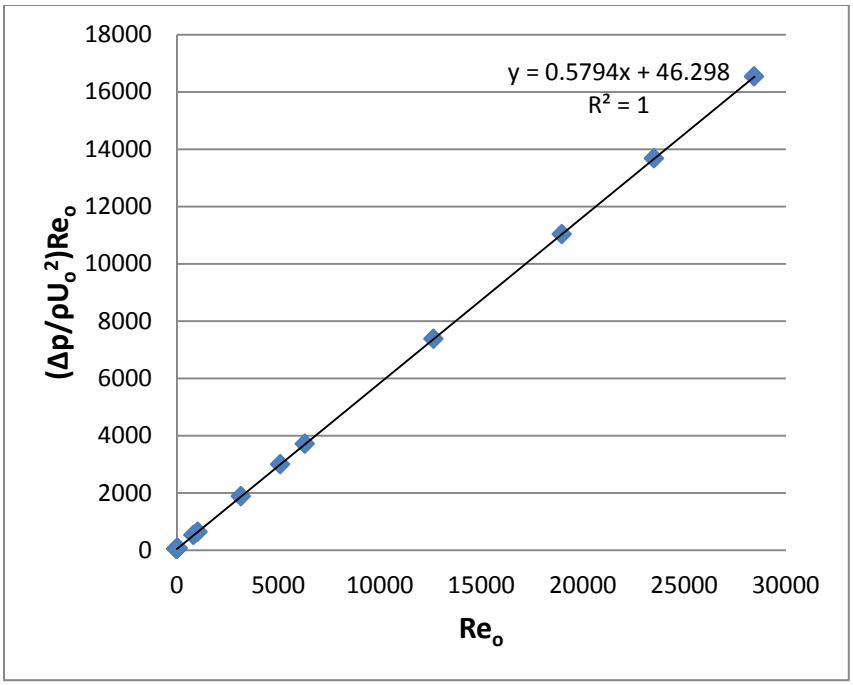

Fig. 54. Generalized pressure drop representation, inclination angle of 22.5 degrees and porosity of 20%.

Table 6: Critical parameters for inclined impingement, t/D = 1.0, and porosity of 20%.

Impingement Angle (degrees)	**α**	**β**
0	51.1	0.660
5	51.4	0.664
15	50.7	0.608
22.5	46.3	0.579

It can be seen from the table that the cases of normal and five-degree impingement yield virtually identical results for the thickness and porosity for which information is available for the latter case. In this light, it seems reasonable to accept the normal impingement results as being applicable for five-degree

inclined impingement for the other thickness and porosity results. The values of the results for the larger inclination angles, 15 and 22.5 are slightly smaller than those for perpendicular impingement, but only by five percent. This finding substantiates earlier observations about the insensitivity of β to inclination.

4. Correlation of β with Porosity

As a further generalization of the results, the coefficient β will be correlated as a function of the porosity. There is no need to perform a similar correlation for the coefficient α, since it is virtually independent of porosity.

The β values are brought together in Fig. 55 for *t/D* = 0.5. The figure is for a perpendicular impingement and includes results for both the square and staggered arrays. It is seen from the figure that all of the data points are extremely well correlated by a linear representation. The quality of the fit invites both interpolation and extrapolation.

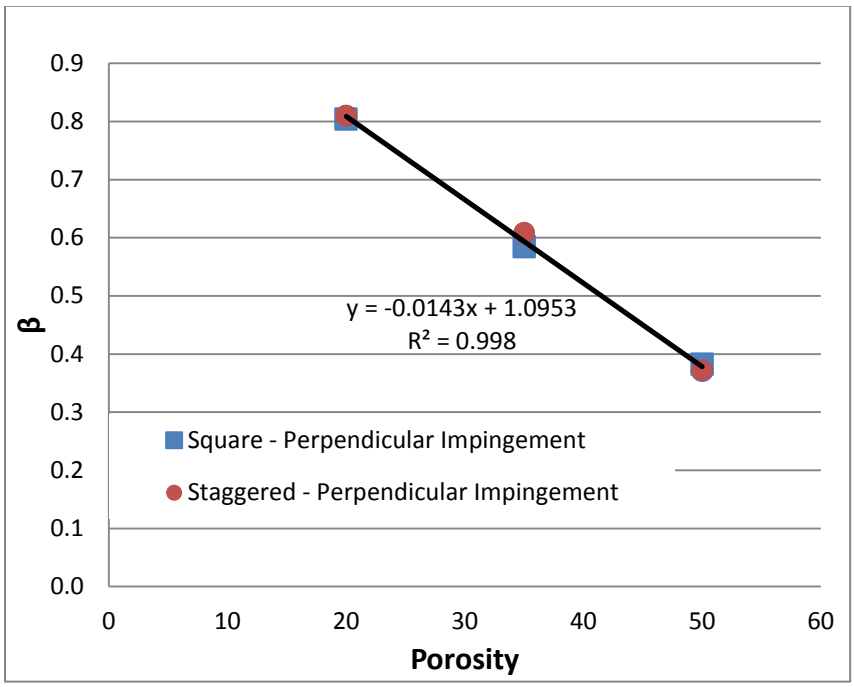

Fig. 55. Correlation of the coefficient β as a function of the porosity for *t/D* = 0.5.

The counterpart figure for the plate thickness *t/D* = 0.5 is presented as Fig. 56. The figure not only includes the information for the square and staggered arrays for perpendicular impingement, but also shows data for inclined impingement. The information for perpendicular

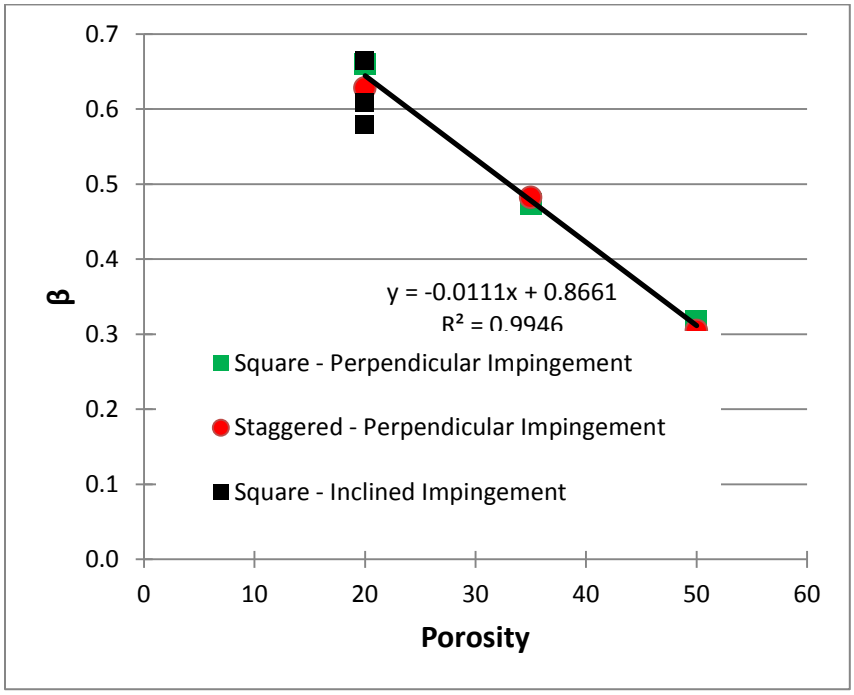

Fig. 56. Correlation of coefficient β as a function of the porosity for *t/D* = 1.0.

impingement for the square and the staggered arrays are sufficiently congruent to warrant a single correlation which is represented by the straight line in the figure. Since the R^2 statistic of the fit is 0.995, it is believed that the corresponding linear equation can be used for both interpolation and extrapolation. The black square data symbols in the figure represent the three impingement angles for the inclined flow. Of the three data, the uppermost corresponds to five-degree impingement, with decreasing β values with increasing angle of impingement. The extent of the spread among the inclined-impingement results is on the order of 10%.

5. Concluding Remarks

In this chapter, it has been demonstrated that the pressure drop results for flow impingement on a perforated plate can be brought together to enable competent generalization. Since pressure drop is the result of greatest practical relevance, the generalization can be of significance for design.

An even broader utility of the results is their possible impact on commercial software packages. In that regard, guidance may be taken from the numerical treatment of porous media. Major software packages avoid a direct assault to determine porous-media pressure drop. Instead, the software in question makes use of an equation comparable to Eq. (2). By the same token, a similar strategy can be performed for perforated plates whereby Eq. (2) can be utilized to determine pressure drop while avoiding a direct numerical assault.

Chapter 5: Application of the Taguchi Method for Extracting Cause and Effect Relations

1. Introduction

The Taguchi method is a statistical methodology which was developed and introduced by the Japanese scientist *Genichi Taguchi* to improve the quality of manufactured items. It has been employed in numerous diverse applications including engineering [49], biotechnology [50, 51], and marketing and advertising [52]. In particular, Taguchi's method can be used for designing experiments in order to (i) investigate how various parameters affect the mean target and (ii) determine the variance of a process-performance characteristic that defines how well the process is functioning.

In the Taguchi method, an experimental-design methodology is employed where orthogonal arrays are used to organize the parameters in a manner that diminishes the number of experiments or computer runs that are required to differentiate among the importance of the participating parameters. Instead of having to test all possible combinations as in the familiar Design of Experiments (DOE) methodology, the Taguchi method tests pairs of combinations of the independent variables. This enables the collected data to be processed in such a way as to determine which parameters have the greatest effect on product quality with a minimum amount of experimentation, thus saving time and resources. The Taguchi method is best used when there is an intermediate number of participating variables (3 to 50), few interactions between variables, and only a few of the variables contribute significantly [53]. Thus, it can be said that the Taguchi approach provides two advantages: (i) the reduction in the variability (improved quality) of a product or process represents a lower loss to

society and (ii) the optimal development strategy can directly reduce variation [54].

Although the Taguchi method is, in general, used as the basis of “design of experiments”, the method can also be applied to numerical analysis since its goal is to evaluate the effects of the design parameters on the performance characteristics employed in either numerical or experimental analyses. In this chapter, the specific steps involved in the application of the Taguchi method to the flow perpendicular to perforated plates will be described. The method is applied to evaluate the effects of design parameters such as Reynolds number, plate thicknesses, hole patterns, and the porosity of the plate on pressure drop [55, 56].

2. Analysis

In the Taguchi method, process parameters which influence the products are separated into two main groups: control factors and noise factors. Control factors are those which are set by the designer and cannot be directly changed by anyone. Noise factors are those over which the designer has no direct control and may vary with the environment and application [54]. The control factors are used to select the best conditions for stability in the design of a manufacturing process, whereas the noise factors denote all quantities that cause variation.

The Taguchi method enables the researcher to perform an investigation with the use of orthogonal arrays. The researcher can determine the optimal process parameters by employing these arrays [54, 56]. The greatest benefit of this method is the reduced number of experiments required to study the entire parameter space. The orthogonal arrays that are relevant to the method can be derived or found in the literature [57]. Small arrays can be derived mathematically in contrast to the large arrays which are derived from deterministic algorithms. In general, most researchers use the arrays that are readily available in the

literature [58]. The selected arrays include the independent parameters (variables) and their levels (states). Analysis of variance of the collected data from the Taguchi design of experiments can be used to select new parameter values to optimize the performance characteristics. These parameters can be operational characteristics such as speed or pressure or can be due to geometry, such as thickness. Common methods of data analysis are conducted by plotting the data and performing a visual appraisal or by use of statistical methods such as ANOVA, bin yield and Fisher's exact test, or the Chi-squared test to evaluate significance [53, 54].

For the study described in Chapter 2, Reynolds number (3000 to 15000), porosity of the perforated plates (19.6 and 50.3), plate thickness (t/D = 0.5 and 1), and hole pattern (staggered and square) are independent parameters also referred to as control factors within the Taguchi method. The control parameters and their levels are listed in Table 7. These parameters are organized according to the Taguchi quality design concept, and an L_{16} orthogonal array with 16 rows (corresponding to the number of experiments) is set up and presented in Table 8.

Table 7 Control factors used in the experiments

Factors	Symbol	Level 1	Level 2	Level 3	Level 4	Level 5	Level 6	Level 7	Level 8
Reynolds	A	3000	4000	5000	7000	9000	11000	13000	15000
Porosity	B	19.6	50.3	---	---	---	---	---	---
Thickness	C	0.5	1	---	---	---	---	---	---
Pattern	D	staggered	square	---	---	---	---	---	---

In the Taguchi method, a loss function is used to calculate the deviation between the experimental values and the optimum output values. These ideal output values are defined by Taguchi. If the researcher is looking to create a design that would minimize a performance characteristic, Taguchi defines the optimum output value as zero. In the analysis stage, this loss function is transformed into a signal-to-noise (*S*/*N*) ratio. There are several *S/N* ratio definitions available; lower is better (*LB*), nominal is best (*NB*), or higher is better (*HB*). The selection of the *S/N* ratio depends on the type of performance criteria that is being evaluated. In this study, a lower pressure drop is the indication of better performance. Therefore, the *LB* for the pressure drop is selected to obtain optimum-performance characteristics. For the *LB*, the definition of the loss function (*L*) for performance results y_i of *n* repeated number is

$$L_{LB} = \frac{1}{n}\sum_{i=1}^{n} y_i^2 \tag{1}$$

The y_i is the pressure drop for each experiment run and the loss function L_{LB} for each of these runs are then calculated. The *S*/*N* ratio η_{ij} for the i_{th} performance characteristic in the j_{th} experiment can be expressed as

$$\eta_{ij} = -10\log\left(L_{ij}\right) \tag{2}$$

where the loss function L_{LB} for each performance characteristic *i* in the j_{th} experiment is identified as L_{ij}. Regardless of the category of performance characteristic, a greater η value corresponds to a better performance. Therefore, the optimal level of the design parameters is the level with the greatest η value. By applying Eqs. (1) and (2), the η values for each experiment of the L_{16} array (Table 8) is calculated and exhibited in Table 3.

Table 8 Experimental design using L_{16} orthogonal array

Experiment no	**Control factors**				***S/N* ratio (η)**
	A	**B**	**C**	**D**	**ΔP**
1	1	1	1	1	1.494
2	1	2	2	2	9.564
3	2	1	1	1	1.587
4	2	2	2	2	9.698
5	3	1	1	2	1.849
6	3	2	2	1	10.01
7	4	1	1	2	1.864
8	4	2	2	1	10.12
9	5	1	2	1	3.945
10	5	2	1	2	8.268
11	6	1	2	1	3.945
12	6	2	1	2	8.268
13	7	1	2	2	3.670
14	7	2	1	1	8.519
15	8	1	2	2	3.662
16	8	2	1	1	8.589

The values in Table 9 are calculated by taking the average of the S/N values in Table 8. As an example, parameter A from Table 8 is averaged to get the S/N value (1.494+9.561)/2 = 5.529

Table 9 η values for pressure drop

Factors	Symbol	Level 1	Level 2	Level 3	Level 4	Level 5	Level 6	Level 7	Level 8
Reynolds	A	5.529	5.643	5.927	5.990	6.106	6.106	6.095	6.126*
Porosity	B	2.752	9.129*	--	--	--	--		
t/D	C	5.055	6.826*	--	--	--	--		
Shape	D	6.025*	5.855	--	--	--	--		

* Optimum level. Overall mean = 5.940 dB (calculated on average of all η values in Table 9)

Based on the analysis of *S*/*N* ratio, the effects of the optimal Reynolds number, porosity, thickness of the plate, and the pattern of the holes are found to be 6.126 (Level 8-A8), 9.133 (Level 2-B2), 6.833 (Level 2–C2) and 6.033 (Level 1-D1), respectively. This means that the Reynolds number of 15,000 in combination with porosity at 50.3%, t/D at 1, and the staggered pattern provides the highest signal over noise ratio. In other words, if the levels A8B2C2D1 are considered, the optimal pressure drop value is obtained. This comparison between parameters using the S/N ratio is shown in Fig. 57. The black lines in the figure are used to sort the parameters into four groups and also, the overall mean is outlined with the red line.

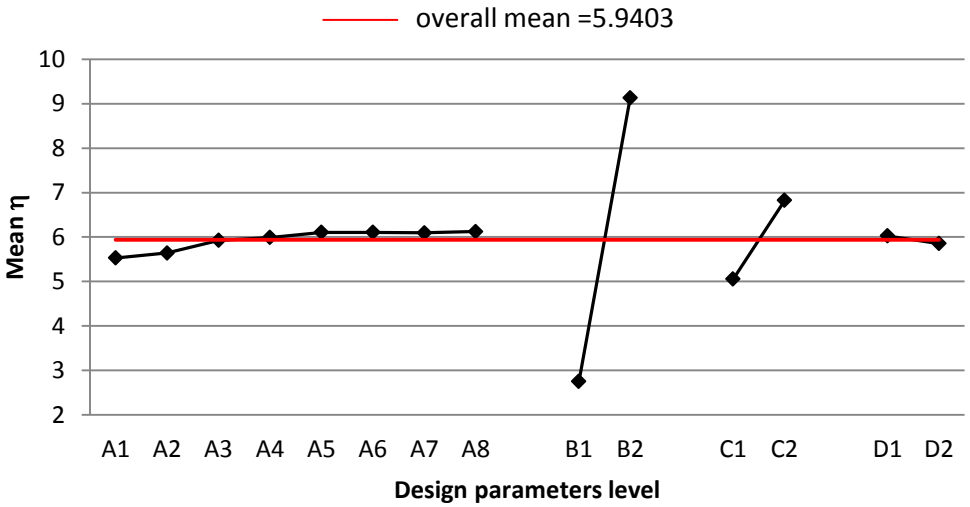

Fig. 57: The effect of design parameters on pressure drop

3. ANOVA Analysis

A more accurate result for the relative effects of the different experimental parameters on pressure drop is obtained by variance decomposition, which is referred to in the literature as the analysis of variance (ANOVA) [58]. The magnitude of the effects of the experimental parameters on the pressure drop is determined by means of the variance analysis method, ANOVA. By the use of this method, the experimental errors are evaluated, and the effects of various factors are resolved. The equations of the ANOVA analysis are as follows [58]

$$SS_m = \frac{(\sum \eta_i)^2}{n} \tag{3}$$

$$SS_{factor} = \frac{\sum \eta^2_{factor-i}}{N} - SS_m \tag{4}$$

$$SS_T = \sum \eta_i^2 - SS_m \tag{5}$$

$$SS_e = SS_T - \sum SS_A \quad (6)$$

$$df_{total} = n - 1 \quad (7)$$

$$df_{factor} = k - 1 \quad (8)$$

$$V_{factor} = \frac{SS_{factor}}{df_{factor}} \quad (9)$$

$$F_{factor} = \frac{V_{factor}}{V_{error}} \quad (10)$$

where SS_T is the total sum of squares, SS_m is the sum of squares due to the mean, SS_{factor} is the sum of squares due to inputs which are also referred to as parameters , SS_e is the sum of squares due to error, $\eta_{factor\text{-}i}$ is the sum of *i*th level of factor, *N* is the repeating number of each level of factors, *df* is the number of degrees of freedom, *n* is the number of the experiments, *k* is the number of the factor's level, V_{factor} is the variance of the factor, and F_{factor} is the *F-test* value of the factor. The results of the ANOVA analysis are presented in Table 10.

Table 10 Results of ANOVA

Factor	Degree of freedom (*df*)	Sum of square (*SS*)	Variance (*V*)	F-test	$F_{.05}$	Contribution (%)
A	7	0.747	0.107	9.75*	4.88	0.38
B	1	162.7	162.7	14843*	6.61	92.24
C	1	12.55	12.55	1145*	6.61	7.11
D	1	0.115	0.115	10.49*	6.61	0.059
Error	5	0.055	0.0110			0.211
Total		176.1				

* at least 95% confidence level

The *F* test is used for quantifying the effects; in other words, the magnitude of the results of the analyses is evaluated by means of the *F* test. The calculated *F*

values are compared to appropriate standard confidence tables which are presented in Ross's textbook [54]. If the F values calculated in this analysis are larger than the F values in the standard confidence tables, the analysis is concluded to be at that assumed confidence level.

According to this analysis, the most effective parameter with respect to pressure drop is the porosity, followed by the thickness of the plate, whereas the effects of the hole pattern and the Reynolds number on the pressure drop were insignificant. Percent contribution indicates the relative influence of a factor to reduce variance. For a factor with a high percentage of contribution, a small variation will have a great influence on the performance. The percentage of contributions of the design parameters on the pressure drop are shown in Table 4. According to this table, the porosity was found to be the major factor affecting the pressure drop with 92% of the contribution, followed by the thickness of the plate with 7.1%. The Reynolds number is found to be the third ranking factor at 0.38%. Finally, the least effective parameter on the pressure drop is found to be the hole-pattern of the plate, with a value of 0.059%.

4. Confirmation Experiment

The confirmation experiment is the final step in the first iteration of the design of experiments process. The purpose of the confirmation experiment is to validate the conclusions drawn during the analysis phase. This experiment is performed by conducting a test with a specific combination of factors and levels previously evaluated. In this study, after determining the optimum conditions and predicting the response under these conditions, a new experiment is designed and conducted with the optimum levels of the design parameters. The final step is to predict and verify the improvement of the performance characteristics. The predicted *S*/*N* ratio using the optimal levels of design parameters can be calculated as:

$$\hat{\eta} = \eta_m + \sum_{i=1}^{p} (\bar{\eta}_i - \eta_m) \quad (11)$$

where η_m is total mean of *S*/*N* ratio, $\bar{\eta}_i$ is the mean of *S*/*N* ratio at the optimal level, and *p* is the number of main design parameters that significantly affect the performance.

The results of experimental confirmation using optimal design parameters are shown in Fig. 58. This figure shows the comparison of the predicted pressure drop with the actual pressure drop using the optimum design parameters. It is clear from the graph that the obtained and predicted values have an excellent agreement between each other.

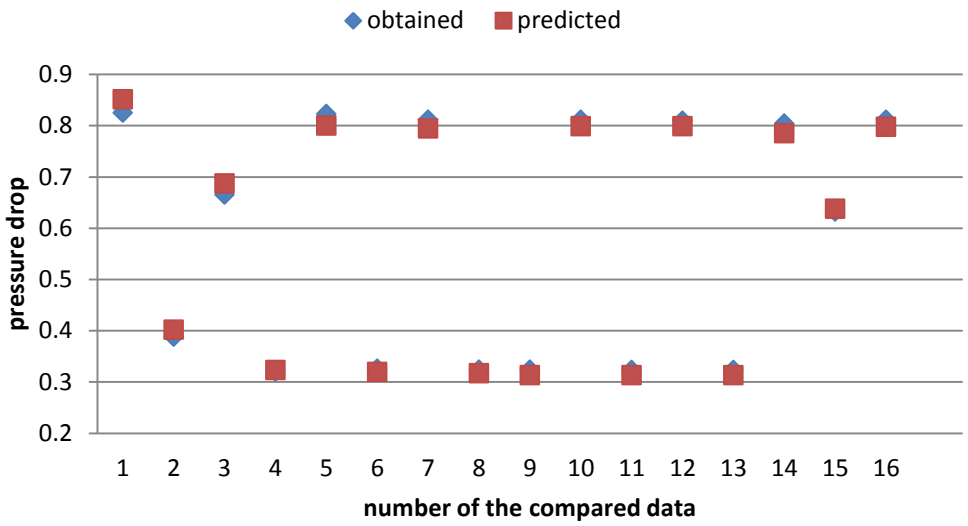

Fig. 58: Results of the confirmation

5. Concluding Remarks

It is relevant to compare the outcome of the foregoing Taguchi-based analysis with what would be gleaned from visual observation of the results that were displayed in Chapter 2. The issue at hand is whether the hierarchy of importance that was provided by the Taguchi study could be determined by mere observation of the results. According to the Taguchi evaluation, the parameter of greatest importance is porosity, with plate thickness a distant second in the importance ordering. The Reynolds number and the hole-distribution pattern were found to have little impact.

Attention will now be directed to Figs. 13 and 14 of Chapter 2. In each figure, information is conveyed as a function of the Reynolds number for parametric values of the porosity. Figure 13 corresponds to a ratio of plate thickness to diameter of ½, while Figure 14 is for a ratio of 1. For both figures, over a porosity range of 0.19 to 0.5, the dimensionless pressure drop varies by a factor of two. This degree of change is clearly a major importance and supports the Taguchi finding. Focus will now be shifted to the importance of plate thickness, and for this assessment, Figures 13 and 14 are also relevant. Inspection of the differences in the dimensionless pressure results as a function of the t/D ratio reveals a modest variation, on the order of 10%. Clearly, this is an outcome that once again is in line with the Taguchi outcome.

The final issue to be addressed is the degree of significance of variations of the Reynolds number and of the pattern of hole deployment. If Figures 13 and 14 are reexamined from the standpoint of Reynolds number and hole pattern, it is unambiguously evident that the results are virtually independent of the variations of these quantities.

CHAPTER 6: FLOW IN PUMPS INCLUDING FLUID-STRUCTURAL INTERACTIONS AND CONTROL

1. Introduction

There are very diverse applications of fluid flows where control and conditioning are a necessity. In addition to other applications and devices, this need is encountered in fluid-moving devices such as pumps for liquids and blowers and fans for gases. Here, the focus is on the pumping of liquids. The uniqueness of the work set forth in this chapter is a means of control that is rarely implemented in pump design. Specifically, the pattern of fluid flow is strongly affected by the geometry of the flow passages. Those passages are the recipients of forces exerted by the flowing fluid. The forces may distort the passage geometry and thereby distort the pattern of fluid flow. To achieve a desired flow pattern, it is necessary to be able to predict the interactions of the fluid forces and the structure of the bounding passages. This type of interaction is commonly termed FSI (Fluid-Structure Interaction).

There are two general categories of interactions that are encountered in the implementation of FSI. One of these is designated as one-way FSI. In such situations, the fluid forces are calculated by means of CFD (Computational Fluid Dynamics) in rigid passages of prescribed geometry. Those forces are then imposed on the structure of the passages, and the stresses, strains, and displacements are calculated. This information is then used to determine whether or not the structural integrity is sufficient to contain the fluid flow. The second category is termed two-way FSI. In that case, the shape of the flow passage as modified by the displacements due to fluid forces is used for the bounding walls in a second CFD simulation. This simulation yields a new fluid flow pattern and different fluid forces. It is common practice that this second CFD simulation terminates the analysis, but it is possible to continue the back-and-forth pattern of solving the structural and fluid flow problems.

The focus of this chapter is to devise a methodology that enables the implementation of the solution procedure that has been described in the foregoing.

2. Motivation

Due to ever-increasing operating costs, the end users of construction and agricultural equipment are requiring better fuel economy in their equipment. This requirement has motivated the need for better understanding of the fundamentals that underlie the equipment designs. In today's heavy equipment, the fuel-consumption pattern is well established. A large percentage of the fuel is used to propel the vehicle, and the remainder is used for powering the auxiliary systems. In most cases, these auxiliary systems as well as the propulsion mechanisms are driven by axial-piston, swash-plate-type hydrostatic pumps. This reality has focused attention on the mechanical design of these devices with regard to power density, efficiency, and interaction with the pumped fluid medium. However, the interaction dynamics of axial-piston pumps and of the pumped fluid are not sufficiently well understood to create highly efficient designs. The goal of this chapter is to analytically expand the design principles that underlie the major components of these devices; specifically, the physical interactions that take place among the structural and fluid components.

3. Background

In a hydraulic system, the function of an axial-piston pump is to convert hydraulic power to mechanical power. These pumps employ the hydraulic liquid as the working medium, which also provides lubrication and enhances sliding of the interacting surfaces. In addition, the hydraulic fluid acts as a spring within the system. Since the fluid is practically incompressible, it experiences a pressure rise when it is ducted into a cavity and gets pressed on by pistons. By this means, the force applied to the hydraulic fluid gives rise to an increase in its potential energy which can be stored as hydraulic power. Another characteristic

of these pumps is their ability to sustain high operating pressures. This capability leads to high power density within the fluid. This technology is the preferred method in the industry for moving heavy equipment rapidly.

Nomenclature

A_b pressurized cross-sectional area in a bore

A_c solid-to-solid contact area

A_p pressurized surface area of a piston

A_s shoe contact area with the swash plate

D_{bore} bore diameter

D_{piston} piston diameter

Y_{re} reaction location in the y-direction

Z_{re} reaction location in the z-direction

F viscous drag force

F_{sf} slipper friction force

F_{sr} spring force

Fr_{sp} reaction force of the swash plate on the n^{th} piston

F_v valve plate reaction force

Fr_{yp} reaction force in the y-direction on the n^{th} piston

F_{ysh} reaction force of the shaft in the y-direction

Fr_{zp} reaction force in the z-direction on the n^{th} piston

Fr_{zsh} reaction force of the shaft in z-direction

l distance

l_n reaction location of the n^{th} piston

l_s reaction location of the shaft

M mass of a piston and a shoe

M_o mass of the oil

N number of pistons

p_n fluid pressure on the n^{th} piston

r piston pitch radius

r_{si} shoe inner radius

r_{so} shoe outer radius

α swash plate angle

β cant angle

μ fluid dynamic viscosity

θ rotation angle about the shaft

ω angular speed

4. Physical Model

In Fig. 59, an isometric view of a drive shaft, swash plate, and rotating kit including a cylinder barrel and pumping pistons from a hydraulic-piston pump is displayed. These components are normally contained in a housing not displayed here. The pump drive shaft is connected to an engine which provides the necessary input torque to drive the pump. As the drive shaft rotates, the barrel and the pumping pistons also rotate. The swash plate does not rotate along with the

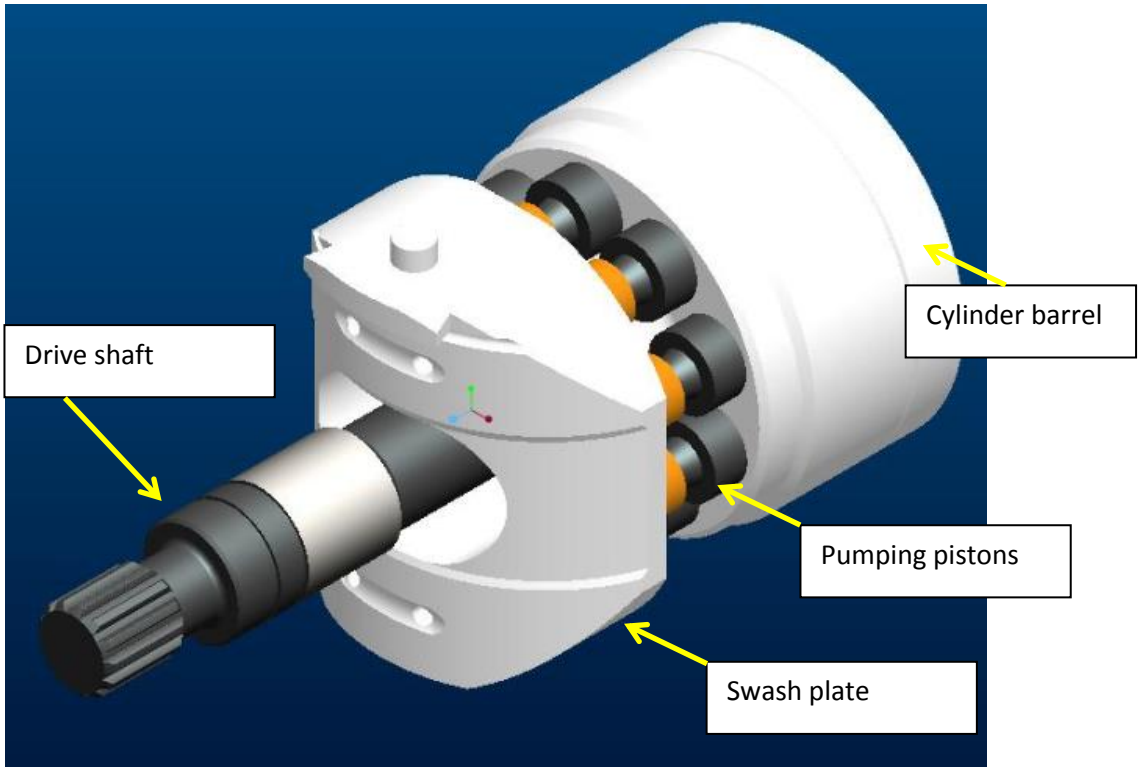

Fig. 59: Isometric of the rotating kit of a hydraulic-piston pump.

drive shaft. The hydraulic pump displacement is controlled by changing the angle of the swash plate from the perpendicular configuration with respect to the pistons. Most axial piston pumps can attain the maximum flow at an angle of 18.5 degrees.

In Fig. 60, a top view of pumping components is displayed. In Fig. 60(a), the swash plate is shown in the neutral position where the pistons are perpendicular to it. During this operational mode, no fluid would be pumped. Once the swash plate is rotated away from the neutral position as shown in Fig. 60(b),the pistons start to move in and out of the barrel as they rotate around. This results in the pumping action. The bronze shoes (depicted in orange color) are swaged around the top of the pistons providing the necessary interface between the piston and the swash plate. As the swash plate angle changes, the shoes also pivot and continually stay pressed against the swash plate.

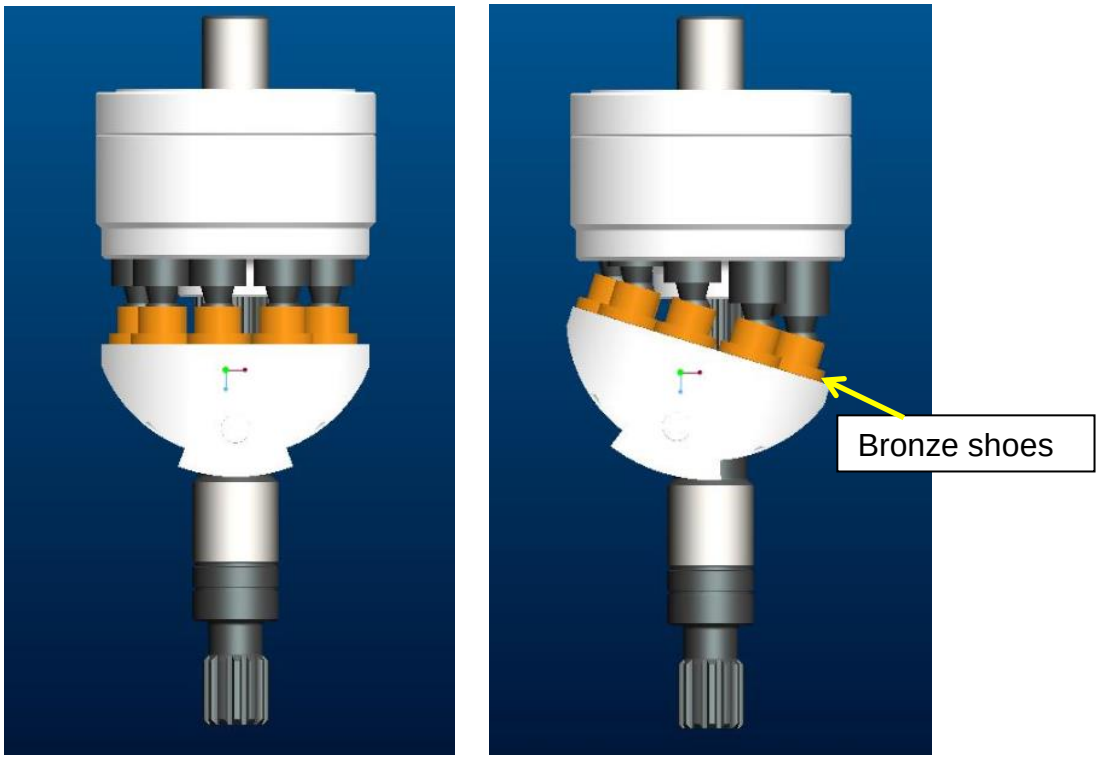

(a) **(b)**

Fig.60: Figure displaying the pump swash plate at neutral and at maximum angle respectively in (a) and (b).

Hydraulic fluid is supplied to the running surface between the shoes and the swash plate via a hole that passes through the tip of the pistons and the shoes.

Since there is pressure in the cylinder bores, the fluid is constantly ejected and creates a hydrostatic balance between the shoes and the swash plate.

In Fig. 61, an isometric view of these components as seen from the back is shown. During normal operation, hydraulic fluid is supplied to the cylinder barrel through the openings at the bottom called kidneys.

Once in the bores of the cylinder barrel, the fluid is pushed upon by the pistons. The incompressible nature of the hydraulic fluid provides a spring action, allowing the fluid to store the mechanical energy provided by means of input torque and speed, and to release this energy in the form of a flowing fluid at high pressure. The low pressure fluid entering into the cylinder barrel becomes pressurized as the cylinder barrel rotates.

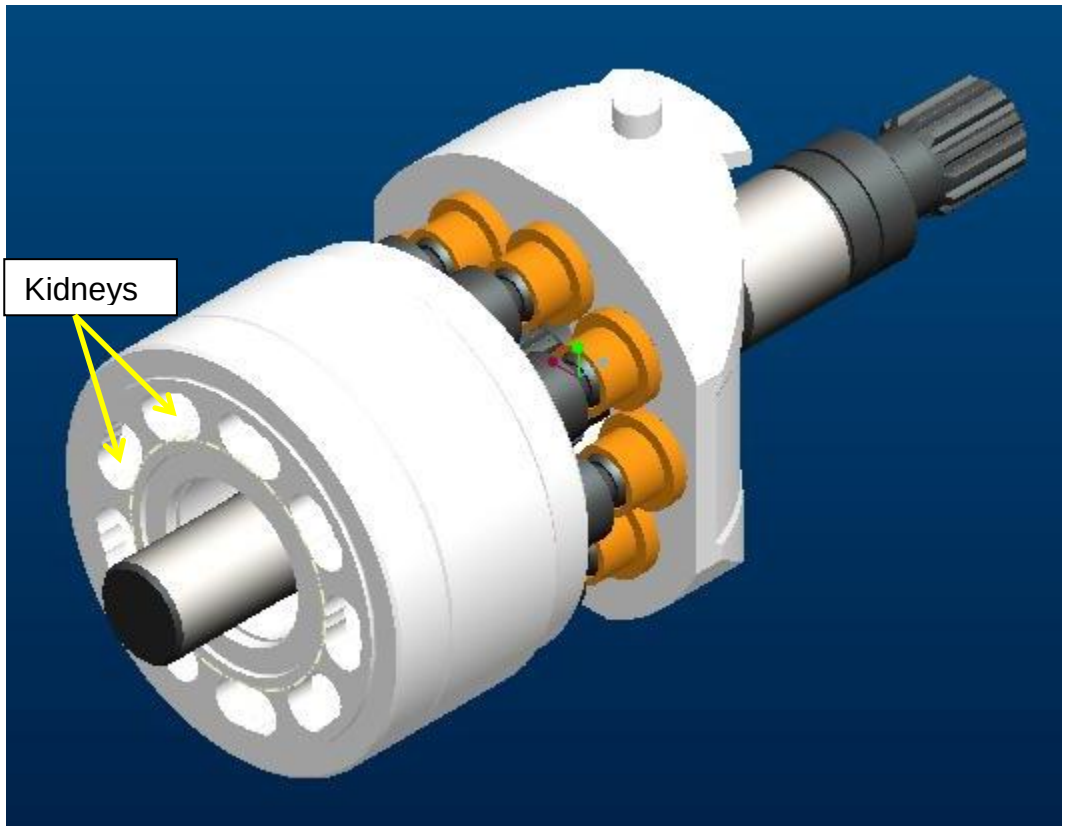

Fig. 61: Isometric view from the back of the rotating kit.

In Fig. 62, the delivery of the low-pressure fluid into the cylinder barrel and its subsequent emergence at the exit as a high pressure fluid is displayed. The hydraulic fluid is distributed from the structural component called the endcover. This part has passages that direct the high pressure fluid to the appropriate ports. When the pump is running, the low pressure fluid is supplied from the endcover and then returned back to it as high pressure. From the endcover, the high pressure fluid is ducted out of the pump for use within the hydraulic machinery. The endcover is omitted from Fig. 62 due to the fact that it is not involved in the forthcoming analysis.

The component called out as the valve plate in the figure is used as a bearing plate between the endcover and the cylinder barrel, and it experiences reaction forces from the swash plate, the pumping pistons, and the cylinder barrel. The cylinder barrel is pushed against the valve plate by means of an internal spring to maintain a constant fluid film between the two running surfaces of the barrel and the valve plate.

By consideration of the components shown in Fig. 62, a full dynamical model of the participating fluid-structural interactions can be achieved. Specifically, with the fluid and structural forces that are generated when the pump is running at its maximum pressure and speed conditions, these components need to be designed properly to withstand the rigors of this application.

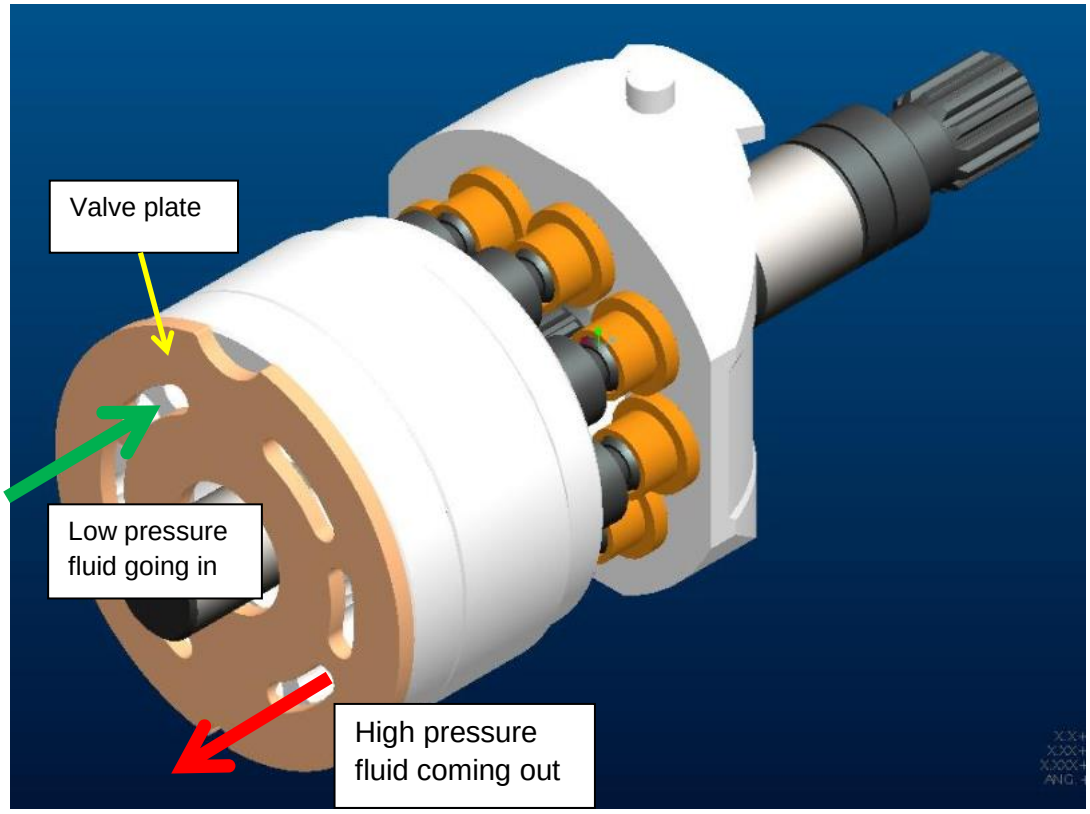

Fig. 62: Isometric view shown from the back of the rotating kit including the valve plate.

5. Literature Survey

The literature on the dynamics of hydraulic-piston pumps is broad, but disconnected. Researchers in the past have analyzed and tested parts of these pumps without creating a comprehensive dynamic model. Ivantysysnova et al. [59] have developed a set of equations based on the conservation of mass and a control volume to be solved numerically to determine the pressure rise in a cylinder barrel bore. They also showed the relationship between the swash plate moments and the valve plate design. However, their study was not extended to cylinder blocks, thereby leaving the full model incomplete. Jacazio and Vatta [60] analyzed without numerical simulation the force relationship between the cylinder block and the valve plate. The lubrication theory was used to determine the barrel lift-off conditions. In this case; the momentum was ignored which makes the analysis only applicable in restricted cases.

Manring [61] resolved the cylinder block tipping moments and outlined the machine design characteristics of hydraulic piston pumps. However, the effect of viscous drag forces and the piston-shoe friction forces were not considered. Thus, the model underestimated the necessary spring force to prevent the cylinder blocks from tipping. McCandlish et al. [62] worked on the sources of losses in hydraulic pumps, but the analysis did not consider the design aspects and only evaluated the performance of the pumps. In a related study, Pourmovahed [63] determined the loss coefficients for hydrostatic pumps and was able to correlate the theoretical loss coefficients with his experimental results.

Yamaguchi [64,65] published a pair of papers on the mechanics of cylinder blocks and valve plates. The first paper analyzed the formation of the fluid film between the cylinder block and the valve plate with hydrodynamic pads. The results do not show a stable fluid film in most cases. The second paper focuses on a cylinder block with hydrostatic pads. The investigation concludes that a fluid film can be maintained during the normal operation of the pump.

With regard to canted bores, there is a deficit in literature. Khalil [66] and Shi et al. [67] dealt with the pump kinematics and dynamics associated with the canted bores without accounting for the moments that are caused by pumping pistons.

The present contribution is a study of axial piston pumps with canted-bore cylinder blocks. Having canted bores in a cylinder block enables hydraulic pumps to run at higher speeds due to reduced inertial forces. To understand the benefits of this configuration, the dynamics of the swash plate, pumping pistons, cylinder barrel, and the valve plate have to be analyzed together.

6. Governing Equations and Analysis

The goal of this analysis is to develop a model and the corresponding set of governing equations that engineers can use to design hydraulic pumps. Specifically, these equations will enable a designer to calculate the forces that will cause the tipping of the cylinder barrel during operation and to provide the criterion that the design needs to meet to prevent this from occurring.

In a hydraulic pump, both the fluid and the structural forces need to be considered within the design. To determine the forces that play a role in the dynamic balance of the barrel, the starting point is a simple force balance. The same approach was also used by Manring [61] without the consideration of viscous drag forces.

Figure 63 shows the reaction force that is present on the swash plate. As the pressure in the barrel bores increase, the force exerted by the pistons on the swash plate also increases. This force has components in both the x and z directions due to the angle at which the swash plate is set during pumping. In barrels with canted bores, the piston bores are not parallel to the drive shaft, but are usually at an angle between 5 and 8 degrees from the parallel. This angle will be represented by the symbol β.

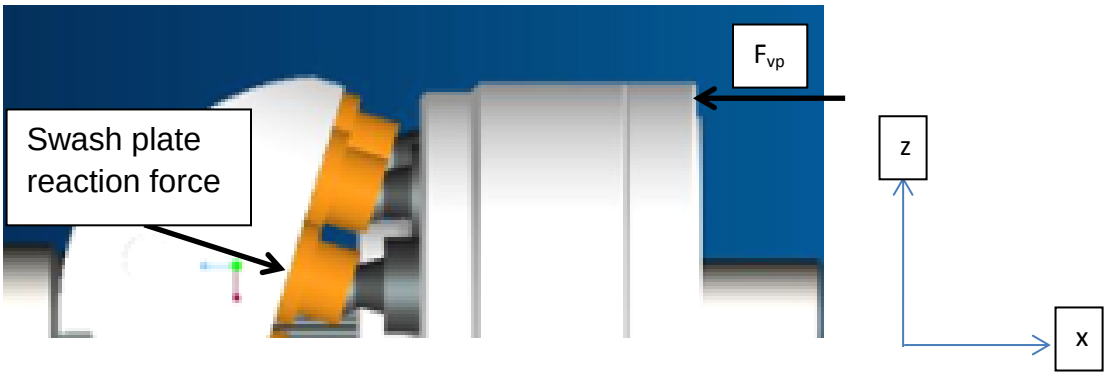

Fig. 63: The swash plate and the valve plate reaction forces

The steady-state force balances on the cylinder block in the x, y and z directions, respectively shown in Eqs. (1), (2), and (3), are as follows:

Equation (1) states that the reaction force at the valve plate is caused by the forces due to piston pressure and the force of the spring that pushes the barrel against the valve plate. This spring is located in a bore inside the barrel. In addition, the piston friction force F_{pf} acts against the motion of the pistons within the barrel bores. The term F_{pf} has been omitted from the previous works in the literature.

$$F_{vp} - A_p \sum_{n=1}^{N} p_n + \sum_{n=1}^{N} F_{pfx} = F_{sr} \tag{1}$$

where p_n is the fluid pressure exerted on piston n, and A_p is the piston area which is common to all of the N pistons.

In Eqs. (2) and (3), the forces due to the pistons are resolved into y and z components, and these result in a reaction force on the drive shaft.

$$0 = Fr_{ysh} + \sum_{n=1}^{N} Fr_{yp} - \sum_{n=1}^{N} F_{pfy} \tag{2}$$

$$0 = Fr_{zsh} + \sum_{n=1}^{N} Fr_{zp} - \sum_{n=1}^{N} F_{pfz} \tag{3}$$

The moment balances in the y and z directions with respect to the center of the y and z axes are displayed in Eqs. (4) and (5). Here, the angle θ represents the angular location of the piston as it is rotating around. In Eq. (4), the presence of θ shows that the amount of force each piston applies is dependent on the angular location around the swash plate. Also, the angle β takes into account the cant angle. For a cylindrical barrel, the cant angle would be zero.

$$F_v Z_{re} = Fr_{zsh} l_s + \sum_{n=1}^{N} Fr_{zp} l_n - \sum_{n=1}^{N} p_n r\, A_b \cos(\beta) \sin(\theta) \tag{4}$$

The rightmost term represents a departure from the corresponding moment description that is standard in the literature. In particular, the quantity cosβ

properly projects the fluid force on the piston along the x-axis. The absence of this quantity overstates the magnitude of the term in question.

As the barrel rotates, there is a moment that occurs due to the locations of all the forces. The terms E_y and E_z are the locations of the valve-plate reaction forces in y ans z directions respectively. The terms l_n and l_s represent the locations of the reaction forces for the piston and shaft respectively.

$$F_v\, Y_{re} = -Fr_{ysh} l_s - \sum_{n=1}^{N} Fr_{yp} l_n + \sum_{n=1}^{N} p_n r\, A_b\, cos(\beta)\, cos(\theta) \tag{5}$$

Next, the friction forces that are present are calculated. The first step is the area calculation.

The clearance between the piston and the bore is given by Eq. (6).

$$r_d = \frac{D_{bore} - D_{piston}}{2} \tag{6}$$

and the contact area between the piston and the cylinder-block bore is set forth in Eq. (7).

$$A_c = \pi D_{piston} l \tag{7}$$

The contact area between the shoes and the swash plate is established in Eq. (8).

$$A_s = \pi (r_{so} - r_{si})^2 \tag{8}$$

The viscous drag force F is opposite to the direction of motion of the piston. Depending on the angular position of the pistons, this force either increases or decreases the hold-down force on the shoes. Also, the viscous drag force is inversely proportional to the cosine of the stroke angle. With the definitions conveyed in Eqs.(6), (7) and (8) the viscous drag force F and the slipper friction force F_{sf} may be respectively represented as

$$F = \frac{A_c \mu \omega r \tan(\alpha)}{r_d \cos(\alpha)} \tag{9}$$

$$F_{sf} = A_s \omega \mu_s \tag{10}$$

The forces on the piston-shoe assembly in each coordinate direction are as follows:

x-direction:

$$Fr_{sp} = \frac{\left[-(M + M_o) r \tan(\alpha)\, \omega^2 \sin(\theta) + A_s \omega \mu_s \sin(\theta_n) + A_p p_n \cos(\beta) - \frac{A_c \mu \omega r \tan(\alpha) \cos(\beta)}{r_d \cos(\alpha)}\right]}{\cos(\alpha)} \tag{11}$$

y-direction:

$$0 = (M + M_o) r \omega^2 \cos(\theta_n) - Fr_{yp} + A_p p_n \sin(\beta) \cos(\theta_n) + \frac{A_c \mu \omega r \tan(\alpha) \sin(\beta) \sin(\theta_n)}{r_d \cos(\alpha)} + \frac{A_s \omega \mu_s \cos(\theta_n)}{\cos(\alpha)} \tag{12}$$

z-direction:

$$0 = (M + M_o) r \omega^2 \sin(\theta_n) - Fr_{sp} \sin(\alpha) + A_p p_n \sin(\beta) \sin(\theta_n) - Fr_{zp} + \frac{A_c \mu \omega r \tan(\alpha) \sin(\beta) \cos(\theta_n)}{r_d \cos(\alpha)} + \frac{A_s \omega \mu_s \sin(\theta_n)}{\cos(\alpha)} \tag{13}$$

After rearranging the moment balances, Eqs. (4) and (5), by substituting Eqs. (2), (3), (11), (12), and (13), there emerges Eqs. (14) and (15). Equations (14) and (15) provide engineers with the location of valve plate reaction points in the z and y directions. If the geometry of a pump does not satisfy the criterion that the valve-plate reaction point is outside of the envelope of the given design, the

cylinder barrel will not be stable and there will be a tipping moment present. This means that under certain conditions, such as high pressure or high speed, the cylinder barrel will be pushed away from the valve plate. This will result in loss of high pressure fluid and reduced performance of hydraulic machinery.

$$F_v Z_{re} = \sum_{n=1}^{N} [(M + M_o) r\,\omega^2 \sin(\theta_n) + (M + M_o) r \tan^2(\alpha) \omega^2 \sin(\theta_n) - A_p p_n \cos(\beta) \tan\alpha + F \tan(\alpha) \cos(\beta) + A_p p_n \sin(\beta) \sin(\theta_n) + F \sin(\beta) \cos(\theta_n) + F_{sf} \sin(\theta_n)](l_n - l_s) - \sum_{n=1}^{N} p_n r A_b \cos\beta \sin(\theta_n) \quad (14)$$

$$F_v Y_{re} = \sum_{n=1}^{N} [(M + M_o) r\omega^2 \cos(\theta_n) + A_p p_n \sin(\beta) \cos(\theta_n) + F \sin(\beta) \sin(\theta_n) + F_{sf} \cos(\theta_n)]\,(l_s - l_n) + \sum_{n=1}^{N} p_n r A_b \cos(\beta) \cos(\theta_n) \quad (15)$$

To implement Eqs. (14) and (15) , certain simplifications can be made by using the symmetry of the conical barrels. In particular,

$$\sum_{n=1}^{N} \sin(\theta_n) = \sum_{n=1}^{N} \cos(\theta_n) = \sum_{n=1}^{N} \sin(\theta_n) \cos(\theta_n) = 0 \quad (16)$$

$$\sum_{n=1}^{N} \sin^2(\theta_n) = \sum_{n=1}^{N} \cos^2(\theta_n) = \frac{N}{2} \quad (17)$$

Equations (14) and (15) can be simplified using the identities given by Eqs. (16) and (17), with the outcomes:

$$Z_{re} = \{\frac{N}{2}((M + M_o)r^2\omega^2 \tan(\alpha)(1 + \tan^2(\alpha)) + \frac{N}{2}A_p p_n \cos(\beta)\tan(\alpha)l_s - F\tan(\alpha)\cos(\beta)l_s + \frac{N}{2}(p_n r \sin(\theta_n)(A_p \sin(\beta)\tan(\alpha) - A_p \cos(\beta)\tan^2(\alpha) - A_b \cos(\beta)) - \frac{N}{2}(F_{sf} r \tan(\alpha) l_s)\} / F_v \quad (18)$$

$$Y_{re} = \{\frac{N}{2}(F\, r \sin(\beta)\tan(\alpha)) + \frac{N}{2}p_n r A_b \cos(\beta)\cos(\theta)\}/F_v \quad (19)$$

Next, Eq. (20) is generated to determine the amount of spring force necessary. This is particularly important during low pressure and high speed conditions. Since there will not be a piston force available to hold down the barrel, the spring will need to provide enough force to prevent the barrel from tipping.

$$F_s > \{[F\, r \sin(\beta)\tan(\alpha)]^2 + [N(M + M_o)r^2\omega^2 \tan(\alpha)(1 + \tan^2(\alpha)) + F_{sf} r \tan(\alpha) + F\tan(\alpha)\cos(\beta)r]^2\}^{0.5} / 2R \quad (20)$$

When the equations (18), (19) and (20) are compared to their counterparts in the literature [61], significant differences are observed. The mass of the oil, the friction between the piston and the bores and the friction between the swash plate and shoes were not taken into account in the past. This leads to an inaccurate calculation of the valve plate reaction locations and the spring force necessary to prevent the barrel from tipping during normal operation. Also, the necessary spring force to prevent the barrel from tipping is underestimated.

To assess the errors related to the omission of key phenomena in prior analyses, the more inclusive equations derived here were numerically evaluated as were the corresponding equations from the prior analyses. The input values for these

evaluations were taken from geometric and operational information for a commercially available 72400 pump by Eaton. A listing of all of the physical quantities used as input to the relevant equations for the two models being compared is presented in Table 11. The equations in question are (18)-(20) for the new model and those of [61] for the prior model.

Table 11: Geometric dimensional and operational data used to validate the calculations.

Speed	ω	4000 rpm
Pressure	p_n	5000 psi
Piston + Shoe Mass	M	0.88 lb
Mass of the oil	M	2.7 lb
Swash plate angle	α	17 degrees
Piston pitch radius	r	1.24 in
Number of pistons	n	9
Barrel outer diameter	R	2.45 in
Piston diameter	D_{piston}	0.75 in
Barrel bore diameter	D_{bore}	0.75 in
Cant angle	β	0 degrees

When the results of Eq. (18), (19), and (20) were compared to the results that would be generated by using the equations from the literature [61], the following were the findings.

The method of determining the location of the valve-plate reaction point in the literature is incorrect. The inclusion of the missing terms, as in Eqs. (18) and (19), leads to a difference of 7% in the location results. This means that the equations in the literature incorrectly underestimates the distance between the center point and the point of reaction. A consequence of this underestimation is that, for a given pump, the maximum pressure at which the pump can be run would be predicted to be lower than the actual by this same percentage. Another result of the aforementioned error is that the failure mode would be the tipping of the

barrel due to the valve-plate reaction point would be outside of the specified geometry.

The second issue that was corrected was the necessary spring force to prevent the barrel from tipping. A spring force value of approximately 30% higher was calculated with the updated equations compared to that from the incomplete equations. The under prediction of the spring force from the conventional theory would have significant effects on the overall performance of the pump. To quantify this assertion, the literature-based calculation of the necessary spring force would mean that the maximum speed at which the pump can run would be reduced by 30%. At speeds higher than that corresponding to the literature-based spring force would result in tipping of the barrel which, in turn, would cause a hydraulic-short circuit. Under that condition, the high pressure fluid would be returned to the low-pressure side without any control. In some cases, this short circuit event can cause structural damage to the pump housing due to elevated pressures.

Another negative effect of the improperly calculated spring force is the reduction in the horsepower of the pump. If that spring force were to be believed, the end user would have 30% less horsepower available in their machines. This degradation in performance would also increase the end user costs due to reduced productivity.

CHAPTER 7: GLOBAL CONCLUDING REMARKS

This thesis encompasses a synergistic interaction between physical modeling, numerical simulation, laboratory experimentation, and mathematical analysis. The physical processes underlying all aspects of the work relate to a wide range of fluid mechanic phenomena. One focal point of the thesis is the quantification of perforated plates as a means of flow control. The quantification encompassed a wide range of geometric and operational parameters. The geometric parameters included plate porosity, deployment pattern of the perforations, the thickness of the participating perforated plates, the angle of attack of the oncoming flow, and the cross-sectional dimensions of the host duct. These exhaustive parametric studies were performed by means of numerical simulation.

To ensure the validity of the results of the numerical simulations, a purposeful experimental investigation was undertaken. A special wind tunnel was designed and fabricated to facilitate the experimentation. Pressure measurements both upstream and downstream of the installed perforated plate were used to compare with the numerical predictions for cases congruent between the simulations and the experimentation. The agreement between the results from the two sources was approximately 2%, thereby validating the simulation model and its execution. Once validated, the simulation model was extended to all of the parametric variations that were called out in the penultimate paragraph.

Among the numerical results, the quantity of direct relevance to applications is the relationship between the pressure drop due to all aspects of the presence of the plate and a quantity that describes the nature of the flow. In particular, all possible flow regimes were investigated, including friction-dominated laminar flow, laminar flow with friction and inertial losses, intermittent laminar and turbulent flow, and fully turbulent flow with inertial effects.

A novel method of assessing turbulence levels was formulated by use of a metric which is the ratio of the apparent turbulent viscosity to the molecular viscosity. This metric sharply delineated zones of low, intermediate, and high turbulence.

The pressure drop that occurs in perforated-plate homogenizers was precisely correlated by means of an equation which has roots in the fluid mechanics of porous media. The most widely accepted means of relating porous medium pressure drop and fluid flow is the Forchheimer model. That model has the same form as Eq. (2) of Chapter 4 which was used here for bringing together the perforated-plate pressure drop and a flow parameter. It was found, as detailed in Chapter 4, that Eq. (2) which mimics the Forchheimer equation brings together data extending from Reynolds numbers of 0.001 to 28500. This range significantly exceeds the ranges for which the Forchheimer model has been used in the past. Clearly, this Reynolds number range encompasses all possible flow regimes.

On the other hand, there is a copious literature relating to the Forchheimer model, dealing with its applicability and limitations. One of the widely accepted limitations is that it is restricted to friction-dominated laminar flows and to laminar flows in which inertial effects give rise to non-linearities [68]. This notion flies in the face of what has been found here. It is expected that the broader applicability of the Forchheimer model that has been demonstrated here will significantly alter the physical interpretation and its range of applicability.

A broader utility of the Forchheimer-related results is their possible impact on commercial software packages. In that regard, guidance may be taken from the numerical treatment of porous media. Major software packages avoid a direct assault to determine porous-media pressure drop. Instead, the software makes use of an equation comparable to Eq. (2). By the same token, a similar strategy can be performed for perforated plates whereby Eq. (2) can be utilized to determine pressure drop while avoiding a direct numerical assault.

During the course of the research, an apparent paradox was encountered which challenges superficial intuitive expectations. It was found that in certain circumstances, the perforated-plate pressure drop varied inversely with the thickness of the plate; the thinner the plate, the higher the pressure drop. A full blown diagnostic investigation was performed to unravel the paradox. A careful investigation of the pattern of fluid flow in an aperture disclosed that the absence of reattachment of a recirculation zone within the aperture proper was the factor that gave rise to the higher pressure drop for the thinner plate.

The issue of possible use of an array of perforated plates was also considered. In that regard, the critical information is the distance downstream of a perforated plate at which the plate-induced disturbances die away. For an oncoming flow having a zero angle of attack, the downstream distance for complete decay was on the order of five aperture diameters. In contrast, for non-zero angles of attack, the disturbances due to the presence of the plate persisted to lengths on the order of meters. On the other hand, the most major disturbance due to the plate's presence is a large eddy attached to the rear face of the plate. The downstream closure of that eddy occurred at distances ranging from 0.3 to 0.5m, depending on the duct height. The recirculation zone played the role of a blockage.

An important outcome of the perforated-plate studies was the qualitative identification of the most important of the several parameters which govern the fluid flow. To add rigor and quantification to the rank-ordering of the parametric importance, a Taguchi-based analysis was performed and the results compared to those obtained from qualitative assessment. The rank ordering from the two sources was shown to be in general agreement.

A final demonstration of the overbearing significance of careful fluid mechanic modeling was provided by the analysis set forth in Chapter 6. That chapter was focused on an assumption-free model of fluid flow and concomitant structural interactions in a liquid prime mover. The previously accepted performance in terms of produced flow rate and imparted pressure rise was flawed due to the

absence of accounting for fluid-structural interactions (FSI). The proper accounting of FSI is a relatively recent development, and its application here demonstrates the deficiencies of older forms of analysis. The outcome of the present analysis is a closed-form solution in algebraic form. Numerical involvement is only necessary to evaluate the algebraic quantities.

Bibliography

[1] I. E. Idelchik, Handbook of Hydraulic Resistance, National Technical Information Service, 1966.

[2] G. Gan, S. B. Riffat, Pressure loss characteristics of orifice and perforated plates, Experimental Thermal and Fluid Science 14 (1997) 160-165.

[3] S. Yavuzkurt, G. L. Catchen, Dependence of pressure losses on angle of attack for flow through perforated plates, ASME Fluids Engineering Division 259 (2003) 435-440.

[4] K. D. Broach, M. E. Conner, J. L. Norrell, C. E. Lunde, Perforated plate pressure losses with improved inlet and outlet flow hole features, Proceedings of ASME FEDSM'03 (2003) 767-772.

[5] E. M. Laws, A. Chesnoy, The design and development of flow conditioning devices, Devices for Flow Measurement and Control ASME 159 (1993) 11-17.

[6] E. M. Laws, A. K. Ouazzane, A further investigation into flow conditioner design yielding compact installations for orifice plate flow metering, Flow Measurement and Instrumentation 6 (3) (1995) 187-199.

[7] E. P. Spearman, J. A. Sattary, M. J. Reader-Harris, Comparison of velocity and turbulence profiles downstream of perforated plate flow conditioners, Flow Measurement and Instrumentation 7 (3/4) (1996) 181-199.

[8] A. Erdal, A numerical investigation of different parameters that affect the performance of a flow conditioner, Flow Measurement and Instrumentation 8 (2) (1997) 93-102.

[9] Th. Schluter, W. Merzkirch, PIV measurements of the time averaged flow velocity downstream of flow conditioners in a pipeline, Flow Measurement and Instrumentation 7 (3/4) (1996) 173-179.

[10] W. Xiong, K. Kalkuhler, W. Merzkirch, Velocity and turbulence measurements downstream of flow conditioners, Flow Measurement and Instrumentation 14 (2003) 249-260.

[11] W. Yaici, M. Ghorab, E. Entchev, 3D CFD analysis of the effect of inlet air flow maldistribution on the fluid flow and heat transfer performances of plate-fin-and-tube laminar heat exchangers, International Journal of Heat and Mass Transfer 74 (2014) 490-500

[12] K. Gerova, S. Velikov, K.P. Garry, The effects of porosity and inclination on the pressure drop across porous screens and honeycombs used for heat exchanger simulations in wind tunnel studies, SAE International Journal of Passenger Cars – Mechanical Systems 6 (2) (2013) 483-494.

[13] M.R. Kaern, T. Tiedemann, Compensation of airflow maldistribution in fin-and tube evaporators, in: International Refrigeration and Air Conditioning Conference, Purdue, USA, (2012).

[14] J. Hoffmann-Vocke, J. Neale, M. Walmsley, The effect of inlet conditions on the air side hydraulic resistance and flow maldistribution in industrial air heaters, International Journal of Heat Fluid Flow 32 (2011) 834–845.

[15] M.A. Habib, R. Ben-Mansour, S.A.M. Said, M.S. Al-Qahtani, J.J. Al-Bagawi, K.M. Al-Mansour, Evaluation of flow maldistribution in air-cooled heat exchangers, Computational Fluids 38 (2009) 677–690.

[16] J. Wen, Y. Li, A. Zhou, Z. Zhang, An experimental and numerical investigation of flow patterns in the entrance of plate fin heat exchanger, International Journal of Heat and Mass Transfer 49 (2006) 1667-1678.

[17] J. Wen, Y. Li, Study of flow distribution and its improvement on the header if plate-fin heat exchanger, Cryogenics 44 (2004) 823-831.

[18] A.J. Jiao, Y.Z. Li, C.Z. Chen, R. Zhang, Experimental investigation on fluid flow maldistributions in plate-fin heat exchanger, Heat Transfer Engineering 24 (4) (2003) 25-31.

[19] S. Lalot, P. Florent, S.K. Lang, A.E. Berglles, Flow maldistributions in heat exchangers, Applied Thermal Engineering 19 (1999) 847-863.

[20] A.C. Mueller, J.P. Chiou, Review of various types of flow maldistributions in heat exchangers, Heat Transfer Engineering 9 (2) 1988, 36-50.

[21] B. Sahin, Pressure losses in an isolated perforated plate and jets emerging from the perforated plate, International Journal of Mechanical Sciences 31 No. 1 (1989) 51-61.

[22] B. Sahin, A. J. Ward-Smith, Flow control by perforated plates using a blanking technique in wide-angle diffusers employed in practical electrostatic precipitator systems, Journal of Wind Engineering and Industrial Aerodynamics 37 (1991) 269-284.

[23] B. Sahin, A. J. Ward-Smith, D. Lane, The pressure drop and flow characteristics of wide-angle screened diffusers of large area ratio, Journal of Wind Engineering and Industrial Aerodynamics 58 (1995) 33-50.

[24] S. R. Kosmos, G. L Riskowski, L.L Christianson, Force and static pressure resulting from airflow through screens, Transactions of ASABE 36 (5) (1993) 1467-1472.

[25] A. F. Miguel, N. J. Van De Braak, G. P. A. Bot, Analysis of the airflow characteristics of greenhouse screening materials, Journal of Agricultural Engineering Research, 67 (1997) 105-112.

[26] A. F. Miguel, Airflow through porous screens: from theory to practical considerations, Energy and Buildings 28 (1998) 63-69.

[27] M. Teitel, A. Shklyar, Pressure drop across insect-proof screens, Transactions of the ASABE 41 (6) (1998) 1829-1834.

[28] T. Bartzanas, T. Boulard, C. Kittas, Numerical simulation of the airflow and temperature distribution in a tunnel greenhouse equipped with insect-proof screen in the openings, Computers and Electronics in Agriculture 34 (2002) 207-221.

[29] A. Shyklyar, A. Arbel, Numerical simulations of turbulent flow through screen mesh, Proceedings of International Symposium on Greensys (2007) 995-1002.

[30] J. Groth, A. V. Johansson, Turbulence reduction by screens, Journal of Fluid Mechanics 197 (1988) 139-155.

[31] S. J. G. Pardue, S. S. Munukutla, Experimental studies on turbulence behind screens and perforated plates, AIAA Aerospace Sciences Meeting and Exhibit, 30th, Reno, NV, Jan. 6-9, (1992) 9.

[32] N. Mazellier, L. Danaila, B. Renou, Multi-scale turbulence injector: a new tool to generate intense homogenous and isotropic turbulence for premixed combustion, Journal of Turbulence, 11 (2010) E-print ArXiV:1004.0074v1.

[33] R. D. Mehta, Turbulent boundary layer perturbed by a screen, AIAA Journal 23 (9) (1985) 1335-1342.

[34] E. M. Sparrow, J. C. K. Tong, J. P. Abraham, Fluid Flow in a System with Separate Laminar and Turbulent Zones, Numerical Heat Transfer 53 (4) (2008) 341-353.

[35] S. J. Kline, and F. A. McClintock, Describing Uncertainties in Single-Sample Experiments, Mechanical Engineering (1953) p. 3.

[36] N. Celik, I. Kurtbas, N. Yumusak, H. Eren, Statistical Regression and Artificial Neural Network Analyses of Impinging Jet Experiments, Heat and Mass Transfer 45 (2009) 599-611.

[37] S. Yavuzkurt, G. L. Catchen, Dependence of pressure losses on angle of attack for flow through perforated plates, ASME Fluids Engineering Division 259 (2003) 435-440.

[38] M. Teitel, D. Dvorkin, Y. Haim, J. Tanny, I. Seginer, Comparison of measured and simulated flow through screens: Effects of screen inclination and porosity, Biosystems Engineering 104 (2009) 404-416.

[39] A. B. K. Putra, S. W. Ahn, H. K. Kang, A numerical study on heat transfer and friction in rectangular channel with inclined perforated baffles, The Canadian Journal of Chemical Engineering 87 (3) (2009) 415-421.

[40] B. Y. Guo, Q, F. Hou, A. B. Yu, L. F. Li, J. Guo, Numerical modeling of the gas flow through perforated plates, Chemical Engineering Research and Design 91 (2013) 403-408.

[41] E. Brundrett, Prediction of pressure drop for incompressible flow through screens, Journal of Fluids Engineering 115 (2003) 239-242.

[42] K. Gerova, S. Velikov, K. P. Garry, The effects of porosity and inclination on the pressure drop across porous screens and honeycombs used for heat exchanger simulations in wind tunnel studies, SAE International Journal of Passenger Cars – Mechanical Systems 6 (2) (2013) 483-494.

[43] J. Xiong, A. Johnson, F. Liu, D. Papamoschou, Body force model for the aerodynamics of inclined perforated surfaces, American Institute of Aeronautics and Astronautics Journal 50 (11) (2012) 2525-2535.

[44] T. Lee, Aerodynamic characteristics of airfoil with perforated gurney-type flaps, Journal of Aircraft 46 (2) (2009) 542-548.

[45] C. J. Florendo, T. R. Yechout, S. Siegel, R. M. Cummings, Experimental evaluation of a high fineness ratio body with drag brakes, 44th AIAA Aerospace Sciences Meeting and Exhibit 2006-666 (2006) 1-11.

[46] D. I. Greenwell, R. V. Barrett, Inclined screens for control of ship air wakes, 3rd AIAA Flow Control Conference 2006-3502 (2006) 1-12.

[47] J. Groth, A. V. Johansson, Turbulence reduction by screens, Journal of Fluid Mechanics 197 (1988) 139-155.

[48] F. R. Menter, Two-equation eddy-viscosity turbulence models for engineering applications, AIAA Journal 32 (8) (1994) 1598-1605.

[49] J. L. Rosa, A. Robin, M. B. Silva, C. A. Baldan, M. P. Peres, Electrodeposition of copper on titanium wires: Taguchi experimental design approach, Journal of Materials Processing Technology 209 (2009) 1181-1188.

[50] R. S. Rao, C. K. Ganesh, R. P. Shetty, P. J. Hobbs, The Taguchi methodology as a statistical tool for biotechnological applications: A critical appraisal, Biotechnology Journal 3 (4) (2008) 510–523.

[51] R. S. Rao, R.S. Prakasham, K. K. Prasad, S. Rajesham, P.N. Sarma, L. V. Rao, Xylitol production by Candida sp.: parameter optimization using Taguchi approach, Process Biochemistry 39 (8) (2004) 951–956.

[52] P. H. Selden, Sales Process Engineering: A Personal Workshop, Milwaukee, Wisconsin, ASQ Quality Press (1997) 237.

[53] I. N. Vuchkov, L. N Boyadjieva, Quality Improvement with Design of Experiments: A Response Surface Approach, Kluwer Academic Publishers, Dordrecht (2001).

[54] P. J. Ross, Taguchi Techniques for Quality Engineering, second edition, McGraw Hill Co. New York (1996).

[55] M.S. Chua, M. Rahman, Y.S. Wong, H.T. Loh, Determination of optimal cutting conditions using design of experiments and optimization techniques, Int. J. Mach. Tools Manuf. 33 (2) (1993) 297–305.

[56] S.H. Lee, S.H. Lee, Optimization of cutting parameters for burr minimization in face-milling operations, Int. J. Prod. Res. 41 (3) (2003) 497–511.
[57] M.S. Phadke, Quality Engineering Using Robust Design, Prectice-Hall, Englewood Cliffs, New Jersey, USA (1989).

[58] R. K. Roy, Design of Experiments Using the Taguchi Approach: 16 Steps to Product and Process Improvement, John Wiley & Sons, New York (2001).

[59] J. Ivantysyn, M. Ivantysynova, Hydrostatic pumps and motors, Tech Books International (2003).

[60] G. Jacazio and F. Vatta, The ASME/ASCE Bioengineering, Fluids Engineering and Applied Mechanics Conference (1981) 22-24.

[61] N. Manring, 2000, Tipping the cylinder block of an axial piston swash-plate type hydrostatic machine," Journal of Dynamic Systems, Measurement, and Control, 122 (2000) 216-221.

[62] D. McCandlish, R. Dorey, Steady-state losses in hydrostatic pumps and motors, 6th International Fluid Power Symposium, St. John's Colleges, Cambridge, England (1981).

[63] A. Pourmovahed, Uncertainty in the efficiencies of a hydrostatic pump/motor, Proceedings of the Winter Annual Meeting of the American Society of Mechanical Engineers, Anaheim, CA (1992).

[64] A. Yamaguchi, Formation of a fluid film between a valve plate and a cylinder block of piston pumps and motors (1st Report, a vale plate with hydrodynamic pads), JSME 29 (251) (1986) 1494-1498.

[65] A. Yamaguchi, Formation of a fluid film between a valve plate and a cylinder block of piston pumps and motors (1st Report, a vale plate with hydrostatic pads), JSME 30 (259) (1987) 87-92.

[66] M.K. Bahr Khalil, J. Svoboda, and R.B. Bhat, Modeling of Swash Plate Axial Piston Pumps with Conical Cylinder Blocks, Journal of Mechanical Design ASME, (2003).

[67] Z. Shi, G. Parker, J. Granstrom, Kinematic analysis of a swash-plate controlled variable displacement axial-piston pump with a conical barrel assembly," Journal of Dynamic Systems, Measurement, and Control, 132 (2010) 011002-1-011002-8.

[68] H. Huang, J. Ayoub, Applicability of the Forchheimer Equation for Non-Darcy Flow in Porous Media, Society of Petroleum Engineers 13 (2008) 112-122.